

University of Naples Federico II

Department of Structures for Engineering and Architecture

Ph.D. program in Structural, Geotechnical engineering and Seismic Risk



Ph.D. Dissertation • XXXIV Cycle



Base isolation systems for seismic protection of rocking art objects: modelling and design

Davide Pellecchia

Advisor:

Prof. eng. Luciano Rosati

Co-advisor:

Dr. eng. Nicolò Vaiana

Ph.D. Coordinator:

Prof. eng. Iunio Iervolino



Davide Pellecchia · davide.pellecchia@unina.it
*Base isolation systems for seismic protection of rocking art objects:
modelling and design*
Copyright © 2022, March

Se vogliamo che tutto rimanga come è, bisogna che tutto cambi.

— Giuseppe Tomasi di Lampedusa, *Il Gattopardo*

I'll see you on the dark side of the moon.

— Roger Waters

ACKNOWLEDGEMENTS

The dissertation acknowledgements section is available only in the printed version.

DECLARATION

Davide Pellecchia hereby declares that this dissertation submitted to obtain the academic degree of Philosophiæ Doctor (Ph.D.) in Ph.D. program in Structural, Geotechnical engineering and Seismic Risk is his own unaided work, that he has not used other than the sources indicated, and that all direct and indirect sources are acknowledged as references.

Parts of this dissertation have been published in international journals and conference proceedings.

Naples, 2022, March

CONTENTS

1	INTRODUCTION	1
2	MATHEMATICAL MODELLING OF ROCKING RIGID BODIES	7
2.1	Literature overview	7
2.1.1	Rocking rigid body	7
2.1.2	Base-isolated rocking rigid body	11
2.2	Modelling of rocking rigid body	18
2.2.1	Kinematics	19
2.2.2	Full-Contact	20
2.2.3	Sliding	21
2.2.4	Rocking	22
2.2.5	Slide-Rocking	23
2.2.6	Collisions	25
2.3	Modelling of base-isolated rocking rigid body	26
2.3.1	Kinematics	26
2.3.2	Full-Contact	28
2.3.3	Rocking	29
2.3.4	Collisions	30
3	SEISMIC PROTECTION TECHNIQUES	33
3.1	Restraint mechanisms and mounts	33
3.1.1	Stops and Clips	34
3.1.2	Contour mounts	35
3.1.3	Internal mounts	35
3.2	Seismic Isolation Bearings	36
3.2.1	Elastomeric Bearings	37
3.3	Wire Rope Isolators	39
3.3.1	Experimental set-up	42
3.3.2	Analysis of results	45
3.3.3	Influence of displacement magnitude	46
3.3.4	Influence of vertical preload	48
3.3.5	Influence of frequency	49
3.3.6	Influence of wire rope diameter	51
4	MATHEMATICAL MODELLING OF SEISMIC ISOLATORS	55
4.1	The class of Bouc-Wen differential models	56
4.1.1	Modelling of symmetric hysteresis loops	57
4.1.2	Modelling of asymmetric hysteresis loops	60
4.1.3	Modelling of pinched hysteresis loops	63
4.1.4	Modelling of degrading hysteresis loops	67
4.2	Proposed class of uniaxial phenomenological models	70
4.2.1	Assumptions of the class of hysteretic models	71
4.2.2	General expressions of the four curves	72

4.2.3	Bilinear model formulation	74
4.2.4	Algebraic model formulation	75
4.3	The energy-based design process	77
4.3.1	Evaluation of the energy dissipated per cycle	77
4.3.2	Evaluation of the bilinear model parameters	79
4.3.3	Evaluation of the algebraic model parameters	80
5	COMPUTATIONAL ANALYSIS	83
5.1	Overturning spectra generated by impulsive excitation	83
5.1.1	Elastomeric isolators	84
5.1.2	Wire Rope Isolators	87
5.2	Application of sculptures subjected to seismic excitation	88
5.2.1	Application of a Caryatid from the Erechtheion	89
5.2.2	Application of the six of Michelangelo's sculptures	91
5.2.3	Application of the Emperor Caracalla's bust	95
6	CONCLUSIONS AND PERSPECTIVES	103
	BIBLIOGRAPHY	107

LIST OF FIGURES

Figure 1.1	Collapse of sculptures located in the Spanish Fortress of L'Aquila [92].	2
Figure 1.2	Earthquake damages in Kos Island, 2017.	3
Figure 1.3	Several collections of the Zagreb Archaeological Museum were severely damaged during the earthquake in 2020.	4
Figure 2.1	Geometrical properties of the rocking rigid body.	19
Figure 2.2	Instances of the motion that can occur: (a) Full-Contact; (b) Sliding; (c) Rocking; (d) Slide-Rocking.	19
Figure 2.3	Forces acting during the Sliding phase.	21
Figure 2.4	Forces and moments acting during the Rocking phase.	22
Figure 2.5	Forces and moments acting during the Slide-Rocking phase.	23
Figure 2.6	Geometrical properties of the seismically base-isolated rigid body.	27
Figure 2.7	Instances of the motion that can occur: (a) Full-Contact; (b) Rocking.	27
Figure 2.8	Forces and moments acting during the Full-Contact phase.	28
Figure 2.9	Forces and moments acting during the Rocking phase.	29
Figure 3.1	Physical restrains: stop and clips [103].	35
Figure 3.2	Sculpture anchored by clips [103].	36
Figure 3.3	Contour mounts [103].	37
Figure 3.4	A cast bronze sculpture protected by the internal mount [103].	38
Figure 3.5	Typical hysteretic loops displayed by the main categories of elastomeric bearings for seismic isolation applications: (a) Lead Rubber Bearings; (b) High Damping Rubber Bearings.	39
Figure 3.6	Marble anti-seismic basement. BI= marble lower block, S= marble spheres, DO= Horizontal displacement limitation and recentering device, BS= marble upper block, DV=vertical isolation device inserted in the BS upper block [22].	41
Figure 3.7	(a) Helical WRIS, (b) wire rope cross-section.	41
Figure 3.8	Geometrical characteristics and load direction (a) WRI lateral view, (b) WRI cross-section.	42

Figure 3.9	Laboratory of the Department of Structures for Engineering and Architecture of the University of Naples Federico II. (a) Servohydraulic testing machine and the tested devices, (b) The grip between a tested WRI and the machine.	43
Figure 3.10	The influence of displacement magnitude against the four control parameters.	47
Figure 3.11	Influence of displacement magnitude - hysteresis loops.	48
Figure 3.12	Influence of pre-axial load magnitude on the dynamic behaviour of the PWHS16040 device.	49
Figure 3.13	PWHS1604 hysteresis loops: influence of vertical preload. (a) displacement magnitude equal to 10 mm; (b) displacement magnitude equal to 30 mm.	50
Figure 3.14	Influence of frequency input on the dynamic behaviour of the PWHS16040 device.	51
Figure 3.15	PWHS16040 hysteresis loops: influence of frequency. (a) displacement magnitude equal to 10 mm; (b) displacement magnitude equal to 30 mm.	52
Figure 3.16	PWHS16040 and PWHS16040s hysteresis loops: influence of wire diameter. (a) displacement magnitude equal to 10 mm; (b) displacement magnitude equal to 30 mm.	52
Figure 4.1	The symmetric hysteresis loop of a bearing - H. A. Hadad et al. [55].	57
Figure 4.2	Sensitivity analysis of the Bouc-Wen model with respect to the material parameters.	59
Figure 4.3	The asymmetric hysteresis behaviour of a wire rope isolator along their axial direction - G. F. Demetriades et al. [34].	60
Figure 4.4	Values of the Ψ function in the model by Sireteanu et al.	62
Figure 4.5	Sensitivity analysis of the Bouc-Wen model with respect to the material parameters.	63
Figure 4.6	The hysteresis behaviour of a concrete column section - R. Park et al. [93].	64
Figure 4.7	Sensitivity analysis of the Bouc-Wen model with respect to the material parameters.	66
Figure 4.8	The hysteresis behaviour of a unreinforced masonry panels - D. Liberatore et al. [74].	67
Figure 4.9	Sensitivity analysis of the Bouc-Wen model with respect to the material parameters.	69
Figure 4.10	Hysteresis loop bounded by two straight parallel lines (a) or curves (b).	70

Figure 4.11	Evaluation of the history variable x_j^+ (x_j^-) for a generic loading (unloading) case.	73
Figure 4.12	The full area (a), the area below the top (b) and the bottom (c) curve of the algebraic hysteretic model.	78
Figure 5.1	Overturning spectra for rigid bodies: without base isolation (a), isolated by the LRB (b), HDRB ₁ (c), HDRB ₂ (d) isolation systems defined in Table 5.3 and subjected to the full sine cycle. Dark blue colour = safe area; red colour = overturning area; further colours indicate rocking area; 45 degree parallel lines hatch pattern indicates collapse area for elastomeric bearing.	86
Figure 5.2	The overturning spectra for rigid bodies isolated by four WRIs loaded in (a) Shear and (b) Roll directions and subjected to the full sine cycle. Dark blue colour = safe area; red colour = overturning area; further colours indicate rocking area; 45 degree parallel lines hatch pattern indicates collapse area for WRIs.	88
Figure 5.3	The Caryatid from the Erechtheion.	89
Figure 5.4	The East-West component of the Düzce earthquake acceleration recorded on the 12 th of November 1999 (a); Non-isolated Caryatid's rocking response (b).	90
Figure 5.5	Response spectra obtained from the Düzce earthquake acceleration.	91
Figure 5.6	The rocking (a) and horizontal displacement (b) responses of the seismically base-isolated Caryatid.	91
Figure 5.7	Rocking response of the Michelangelo's sculptures located in the <i>Galleria dei Prigioni</i> at the Accademia Gallery of Florence subjected to the horizontal ground acceleration recorded during the Northridge earthquake (1994).	94
Figure 5.8	Rocking response of the <i>San Matteo</i> statue located in the <i>Galleria dei Prigioni</i> at the Accademia Gallery of Florence subjected to the: (a) Northridge, (b) Loma Prieta, (c) San Salvador, (d) Friuli, (e) Emilia, and (f) Central Italy seismic excitations.	95
Figure 5.9	Full-Contact spectra referring to the seismically base-isolated rigid body with four LRBs whose admissible displacement, viscous damping factor and initial-to-post yield stiffness ratio are listed in Table 5.7	96

Figure 5.10	The displacement time histories of the seismically base-isolated rigid body with the LRBs isolation system, whose properties are listed in Table 5.7 , subjected to the: (a) Northridge, (b) Loma Prieta, (c) San Salvador, (d) Friuli, (e) Emilia, and (f) Central Italy seismic excitations.	97
Figure 5.11	Emperor Caracalla's bust of the Farnese collection (Naples, Italy).	98
Figure 5.12	Numerical results of non-isolated Emperor Caracalla's bust by using the horizontal and vertical components of the Irpinia earthquake (Italy).	100
Figure 5.13	The rocking (a) and horizontal displacement (b) responses of the seismically base-isolated Emperor Caracalla's bust endowed with WRIs loaded in the in Shear direction.	100
Figure 5.14	The rocking (a) and horizontal displacement (b) responses of the seismically base-isolated Emperor Caracalla's bust by WRIs loaded in the Roll direction.	101
Figure 5.15	The horizontal displacements responses of the seismically base-isolated Emperor Caracalla's bust by WRIs loaded in the Shear (a) and Roll (b) directions.	102

LIST OF TABLES

Table 3.1	Geometrical characteristics of tested WRIs, see Figure 3.8 for reference.	42
Table 3.2	Dynamic tests in Tension-Compression direction.	44
Table 3.3	Values of the four control parameters to vary the displacement magnitude.	53
Table 3.4	Values of the four control parameters by varying the vertical preload.	54
Table 3.5	Values of the four control parameters by varying the input frequency.	54
Table 4.1	Sign combinations of the Ψ function in the model by Sireteanu et al.	62
Table 5.1	Properties of the rigid body used for generating the overturning spectra.	83
Table 5.2	Properties of the elastomeric isolators.	84

Table 5.3	The algebraic model parameters obtained by the energy-based design procedure.	85
Table 5.4	Identified model parameters relevant to the experimental hysteresis loops of WRI PWHS16040 tested in Shear and Roll directions.	87
Table 5.5	LRBs' properties and the model constitutive parameters of the model	92
Table 5.6	The geometrical properties (see Figure 2.6) of the equivalent blocks of the six of Michelangelo's sculptures located in the <i>Galleria dei Prigioni</i> at the Accademia Gallery of Florence [16].	93
Table 5.7	The properties considered to evaluate the algebraic model parameters for the isolation of the Michelangelo's sculptures with the LRBs.	94
Table 5.8	The algebraic model parameters obtained from the LRBs' properties listed in Table 5.7 by means of the energy-based design procedure.	96
Table 5.9	The properties considered to evaluate the algebraic model parameters for the isolation of the Michelangelo's sculptures with the HDRBs.	97
Table 5.10	The algebraic model parameters obtained from the HDRBs' properties listed in Table 5.9 by means of the energy-based design procedure.	98
Table 5.11	REXEL outputs.	99

1

INTRODUCTION

Countries in Southern Europe, such as Italy, Greece, and Turkey have probably the most significant number of cultural heritage sites worldwide. Unfortunately, such countries are also known for their intensive seismic activity. According to Parisi and Augenti [92], the frequency of natural disasters and the magnitude of earthquakes increased from 1975 to 2005. Consequently, in recent years, damages caused by earthquakes have been estimated by a total of 3.14 trillion USD.

Earthquake losses have shed light on the vulnerability of existing structures and infrastructures, above all those belonging to cultural heritage constructions. However, when a building shakes due to an earthquake, all elements, including the building contents, will be subjected to the earthquake's inertia forces. This means that the earthquake threatens not only the cultural heritage construction but also its contents. By this last term we mean all non-structural elements, such as machinery, storage units, display furniture and, in the case of museum buildings, collections and artworks. Usually, similarly to most non-structural elements, museum contents are not designed to resist earthquakes accelerations.

Commonly, conservators in charge of protecting collections focus their attention on other important issues, such as fires, flooding due to rain, thefts, vandalism, etc. As a consequence, they are not prepared to prevent or mitigate the damage caused by earthquakes. Moreover, several museum artefacts are freestanding, that is they have little or no restraint, such as sculptures, statues, amphorae, etc. Accordingly, these objects are the most vulnerable ones to seismic excitations since, due to rocking and sliding, they can overturn or fall from the support. As a matter of fact even art objects anchored to larger masses such as pedestals could be severely damaged during an earthquake if their stability is not guaranteed.

Generally, museum buildings belonging to the cultural heritage are rather stiff masonry structures. Although these buildings are able to resist the effects of expected earthquakes, they are not necessarily adequate to host freestanding art objects. As a result, this could be the leading cause of collapse and damage to museum artefacts. Indeed, typical monumental buildings can filter the base seismic motion modifying its frequency and magnitude. The accelerations on the upper floors can be two to four times higher than the ones on the ground floor, as shown by Baggio *et al.* [12]. Consequently, a simple change



Figure 1.1: Collapse of sculptures located in the Spanish Fortress of L'Aquila [92].

of the art object's place, e.g. from the ground floor to the second one, will also require a preliminary study on the feasibility of relocation. In the worst case, it will be necessary to implement a seismic damage mitigation technique, as in the example of the two Riace's Bronzes [22, 98].

Hence, art objects contained in museums are at significant risk of earthquakes, and their collapse and damage are potentially associated with significant human and economic losses. This is especially the case when the collection's value is greater than that of the museum building itself.

The earthquakes of L'Aquila (2009) and Emilia Romagna (2012) caused enormous damage the cultural heritage, as shown in [Figure 1.1](#).

Significant damages due to earthquakes were also experienced from the cultural heritage in Greece; for instance, the Athens earthquake in 1999 is probably the worst natural disaster of modern Greek history, creating economic losses of 3 billion USD [125].

The Kos earthquake in July 2017 caused widespread damage to several archaeological sites and monuments, including the medieval Nerantzia Castle, sections of the ancient agora, and the recently refurbished Archaeological Museum. Notably, of the 43 ancient sculptures on display, five fell from their pedestals, suffering severe damages (see [Figure 1.2](#)).



(a) Kos Archeological site, ref: [Archaeology News Network](#).



(b) Kos Archeological Museum, ref: [Greece-is](#).

Figure 1.2: Earthquake damages in Kos Island, 2017.

To highlight the topic's actuality, [Figure 1.3](#) shows some damages suffered by the Archaeological Museum in Zagreb due to the recent earthquake (occurred on the 22nd of March 2020).

The use of mitigation techniques towards seismic excitation regarding the safety of museum art objects is still scarce. In fact, the larger majority of seismic protection attention is currently given to the monumental buildings rather than to collections, even though some interest and awareness about protection of art objects is beginning to spread by means of workshops and conferences [80].

The first publication on the protection of museum objects from earthquake damage is that associated with a 1987 visit to the Getty Museum by Mihran Agbabian, professor of civil engineering at the University of Southern California.

The research team coordinated by prof. Agbabian proposed to classify art objects and their supports according to their shape and seismic behaviour [1, 2].

Augusti *et al.* [7] suggested a few rules for the safeguard of art objects, such as allowing the sliding motion between the object and its support



Figure 1.3: Several collections of the Zagreb Archaeological Museum were severely damaged during the earthquake in 2020.

in order to reduce the inertial forces, lowering the object's centre of mass to increase its stability, and providing the object with a base isolation system.

Jerry Podany was probably the first cultural heritage conservator to worry about the seismic events and to work on mitigation measures for artefacts. His books and papers from workshops and symposiums represent an essential prerequisite to this study [101–103].

The study of the dynamic response of rigid bodies simply supported on horizontal planes has effectively made possible to address the protection of museum art objects. The first research to establish and solve the equations of motion of a rocking rigid body is due to Housner [60]. His study was applied to understand the rocking behaviour of tall, slender structures, such as water tanks, subjected to horizontal ground motion. Housner discovered that there is a scale effect that makes this kind of structure more stable against overturning than might have been expected.

Housner theory has also been recently applied to freestanding objects in multi-story buildings such as hospital equipment and computer servers [39, 99], as well as, even more notably, to art objects in museums.

Several further analyses have been carried out in the past decades on the rocking response of rigid bodies [6, 63, 126, 148–150]. Although this is a well-known topic in the scientific literature, there have been many recent and significant developments, such as the derivation of closed-form solutions [72], the investigation on the role of the friction coefficient [49, 50, 52], the influence of heavy masses on the rocking behaviour [51], the assessment of the existing protocols for shake table

testing of freestanding objects [31, 32], and the study of the seismic response of storage racks.

From the experimental point of view, recent researches aim at determining the friction coefficients between the rigid body and the base [89] as well as the minimum horizontal acceleration needed to activate rocking [17].

From the mathematical point of view, one can obtain a general estimation of an object's response to an earthquake-induced motion on the basis of Housner theory. The rocking response of freestanding art objects in a museum provides an essential guide to the design of damage mitigation measures, such as restraints and supports, known as mounts, since it allows one to classify the objects in generalised stability categories. The restraints and mounts have not only the function to securely hold an object in an unnatural pose, imposed for the sake of aesthetics or access, but also to prevent damage during an earthquake.

In this dissertation, the performance of the base isolation for the protection of freestanding rigid bodies is studied in depth. Particular emphasis is dedicated to protecting art objects, notably statues, that need many stringent requirements for their safeguard. The dissertation examines the rocking behaviour when the base isolation is supported on the main types of elastomeric isolators, i.e. the Lead Rubber Bearings and High Damping Rubber Bearings, and special device named Wire Rope Isolators. The hysteretic response of the isolation system is modelled by means of an accurate uniaxial phenomenological model belonging to a class formulated by Vaiana *et al.* [133], thus greatly improving the dynamic response accuracy of this highly nonlinear coupled system. The parameters of the proposed hysteretic model have a mechanical meaning that is clearer than those characterising the differential model used in some papers [82, 108, 138, 140]. In addition, we propose a new design process using an energy-based approach regarding the above-mentioned hysteretic model. Notably, we exploit the hysteretic model's algebraic nature to derive a formula that computes the energy dissipated per cycle by a closed-form expression. This can be particularly useful from a technical point of view. The design procedure consists of evaluating the small number of model's parameters by a constrained optimisation problem, equating the energies dissipated by a linear viscous system and the isolator. In this way, the model parameters have been established on the basis of specific and clear criteria, in contrast to the majority of alternative hysteretic models, mostly the Bouc-Wen one, in which they are directly provided without justifying their values and the procedure used to obtain them.

The dissertation is organised as follows

IN THE SECOND CHAPTER, mathematical models generally used to describe rocking rigid bodies' behaviour, with and without base isolation are described.

IN THE THIRD CHAPTER, classical and modern seismic protection techniques of unanchored museum contents are examined.

IN THE FOURTH CHAPTER, the most common hysteretic model, i.e. the Bouc-Wen one, and its most significant variants are discussed. In addition, the proposed hysteretic model and the energy-based design process are described.

IN THE FIFTH CHAPTER, the results of some numerical analyses performed on seismically isolated rigid bodies are displayed and discussed.

IN THE SIXTH CHAPTER, conclusions and some perspectives of the research are drawn.

2

MATHEMATICAL MODELLING OF ROCKING RIGID BODIES

In this Chapter, the mathematical models generally used to describe rocking rigid bodies' behaviour, with and without base isolation are presented. In addition, an extensive literature overview is reported herein for the reader's convenience and to shed light on the key aspects of the rocking mechanism.

2.1 LITERATURE OVERVIEW

2.1.1 Rocking rigid body

The study of the dynamic response of unanchored symmetric rigid bodies on horizontal planes was initially addressed by Housner (1963) [60]. His study was applied to understand the rocking behaviour of tall, slender structures, such as water tanks, subjected to horizontal ground motion. Housner was the first to establish the differential equation of motion of a thin rigid body simply supported on a rigid base by applying the Newton's second law of angular motion. In that study, the rigid body can only rock around one of the two bottom corners and subjected to two types of excitation, namely a rectangular and a half-sine pulse. He also provided closed-form solutions of the differential equation of motion for slender rigid bodies and small rotations. In particular, Housner concluded that there is a scale effect that explains the reason why the larger of two similar bodies are more stable than the smaller ones.

Aslam *et al.* (1978) [6] carried out experimental tests and numerical analyses in which the rigid body was subjected to earthquake motion as well as to single pulse excitations. They concluded that the rocking problem is highly nonlinear and very sensitive to small changes, i.e. the rocking behaviour is very dependent on the boundary condition.

Yim *et al.* (1980) [148] studied the rocking response of rigid bodies subjected to earthquakes by means of a probabilistic approach. In particular, they numerically evaluated the rocking response by using artificially generated ground motions and also produced fragility curves.

Ishiyama (1982) [63] defined six types of motion, namely rest, slide, rotation, slide rotation, translation jump, and rotation jump. Overturning criteria were studied by considering frequency sweep tests with

a variable amplitude as input. Ishiyama concluded that overturning criteria strictly depend on the peak ground velocity.

The first one to consider the interaction between the freestanding rigid body with an elastic soil was Psycharis and Jennings (1983) [104].

Spanos and Koh (1984) [123] studied a rigid rectangular body on a Winkler's foundation under non-stationary motion, and they developed analytical methods able to determine the fundamental modes of the system.

The first one to introduce the concept of the Poincaré section in this field of research was Hogan (1989) [58]. He intensively studied the mathematical structure of the problem, examining the stability as well as the evolution of motion in presence of different boundary conditions.

Shenton and Jones (1991) [115, 116] demonstrated that the stability of a freestanding rigid body depends not only on base acceleration, aspect ratio, weight, and the distribution of the body's mass but also on the properties of the contact surfaces, i.e. on the coefficient of friction. The importance of friction was also explained by Sinopoli (1997) [118]. In addition, Shenton (1996) [114] derived criteria governing the initiation of the slide, rock, and slide-rock motions.

The study of the rocking behaviour of a freestanding rigid body under trigonometric pulses and near field ground motions was investigated in depth by Makris and Roussos (2000) [83]. They discovered that, as a matter of fact, a rigid body under sine-pulse can overturn during its free-vibration regime and not at the instant in which the pulse finishes, as assumed by Housner. Moreover, they found that smaller masses are more sensitive to the peak ground acceleration while larger blocks are prone to overturn because of the peak ground velocity.

Zhang and Makris (2001) [149] established that a rigid body under cycloidal pulse can overturn by exhibiting either one or more collisions or without any collision. The former was called the first mode, whereas the latter the second mode. From the Overturning Acceleration Spectra, the authors deduced that the smaller is the frequency of the pulse to the rigid body's natural rocking frequency ratio, the bigger is the probability of the block to overturn by means of the first mode. On the contrary, a rigid body will overturn by way of the second mode. They concluded that the shape of this region strictly depends on the coefficient of restitution of the collisions and that the nonlinear nature of the problem complicates the development of a practical methodology to establish if a rigid body subjected to an earthquake survives or not.

An in-depth study of the rocking response of rectangular rigid bodies under horizontal and vertical base acceleration was done by Taniguchi (2002) [126]. He considered four types of motion, namely rest, sliding, rocking, and slide-rocking, defining, for each type of motion, the initial and final conditions. In conclusion, Taniguchi realised that the vertical

component of the ground motion adds irregularities to the response and consequently it cannot be neglected.

Peña *et al.* (2007) [100] have carried out a total of 275 experimental tests on a shaking table in order to study the rocking response of four granite stones with different geometrical properties under free vibrations as well as harmonic and random motion. The main aim of their study was to compare the experimental results with two types of analyses, namely the method of complex coupled rocking rotations, and the discrete element method. Both models are extremely sensitive to the variation of the boundary conditions, mostly for the angle that measures the slenderness of the body, usually denoted as α . In fact, a small variation of this parameter produces huge differences in the responses. After a calibration of the experimental data with the theoretical parameters, the two kind of results agreed with each other.

An extensive numerical investigation was done by Purvance *et al.* (2008) [105]. They analysed 34 symmetrical and 24 asymmetrical blocks subjected to 1440 excitations. The overturning fragility curves were compared with experimental tests using blocks having different aspect ratios and characterised by both simple and complex basal contact conditions. The results have shown that blocks with a complex basal contact condition are more fragile than the blocks with a simple basal contact. However, the nondestructive tests showed that blocks with complex basal overturn as well as the more slender blocks with simple contact conditions.

Konstantinidis and Makris (2010) [71] thoroughly investigated the rocking behaviour of full-scale and quarter-scale freestanding laboratory equipment, subjected to trigonometric pulses and near field earthquakes, by means of an experimental campaign. The principal response observed was sliding with an order of magnitude slide displacement equal to 60-70 cm.

DeJong (2012) [33] confirmed a key aspect: the rocking response of rigid bodies subjected to earthquake acceleration is a time-dependent problem. Consequently, elastic analyses with response spectrum would not be helpful. Moreover, his work showed that the impulses can have an amplifying or minimising effect, depending on the amplitude, the spacing, and the duration of the impulses. In particular, in the case of multiple impulses, the effect of amplifying can be relevant.

Dimitrakopoulos and DeJong (2012) [41] derived, by means of an original procedure, a closed-form solution able to define the overturning areas for a slender rocking rigid body in which the equations of motion have been linearized.

The problem of sizing the width of tall freestanding columns having a given height and prone to rock due to earthquakes was investigated by Makris and Vassiliou (2013) [84]. The authors derived the overturning spectra for different pulses able to reproduce the effects

of near-field earthquakes. In addition, by deriving an analytical expression, they have evaluated a minimum design slenderness for a freestanding column having a given size to resist a pulse motion with known acceleration amplitude and duration.

Voyagaki *et al.* (2013) [142] exploited an analytical approach to study the rocking problem of a slender rectangular block subjected to idealised ground acceleration pulses defined by a generalised function. To linearise the problem, the authors considered small rotations as well as no sliding phase. Such a linearised response was analytically compared to the fully nonlinear one. It was shown that the linearized equations of motion predict a more unstable response than their nonlinear counterparts.

Monaco *et al.* (2014) [89] worked on determining the coefficients of friction via experimental tests. The experimental campaign was carried out on prismatic blocks with different dimensions and materials, and utilising a unidirectional shaking table and different supporting surfaces in order to establish the influence of different coefficients of friction. In particular, the experimental campaign was developed in order to reproduce the same conditions of freestanding art objects in museums. The results of the experimental campaign have shown that the rocking motion is the only kind of motion that can occur with increasing frequency when the coefficient of friction assumes high values in regards to the slender rigid block.

Kounadis (2015) [72] derived a closed-form solution for a slender rigid body able to rock and slide. He concluded that the sliding motion is beneficial for the stability of the rigid body subjected to pulses acting in a long period. On the contrary, pulses with small values of the period, tend to destabilise the rigid body.

The stability characterisation of a rigid body under a family of multi-lobe pulse ground motions was thoroughly discussed by Dimitrakopoulos and Fung (2016) [42]. They proposed both exact and approximate solutions for the determination of the collision's times. From the analyses conducted, they revealed that, in most cases, overturn after one or more collisions is attained when the pulse expired.

Gesualdo *et al.* (2016) [49] compared the experimental results in [89] with some numerical analyses. The numerical results when the rigid body undergoes both rest and sliding motion were in agreement with the experimental ones.

Wittich *et al.* (2016) [147] studied the dynamic response of 24 marble statues located in Florence, Italy, in which mass distribution and geometry were obtained by using advanced imaging and processing tools. They considered two geometric data acquisition methods, namely (1) light detection and ranging (LiDAR) and (2) the structure from motion (SfM) methods. Although both methods are useful to support the geometric characterisation, the structure from motion method is a simpler

alternative to the other one. The differences were in the order of 40% for the evaluation of the aspect ratio as well as of the radial distance of the centre of mass. On the other hand, differences greater than 100% may arise for the mass moment of inertia. The analyses have shown variations up to the 50% in terms of the maximum rotational response.

Gesualdo *et al.* (2018) [50] examined the real situation of marble statues freestanding on a flat pedestal subjected to harmonic excitation. In particular, they considered two bodies having different aspect ratios. One was placed on a flat pedestal while the second one was freestanding on a moving base. The former was only able to slide due to its geometry, while the latter could only rock due to the high friction coefficient with the base. In particular, it was showed that the presence of a pedestal modelled as a rigid surface could avoid overturning of a slender rigid body especially in the case of increasing slenderness and increasing mass of the rigid body.

Ther and Kollár (2018) [127] proposed a new design approach able to predict the safety of a rigid body able to rock. In particular, this approach was based on the new Overturning Acceleration Spectra characterised by the replacement impulse duration. In this way, it was possible to verify whether a body is safe from overturning provided that the replacement impulse duration for a specific site is known.

In conclusion, rocking behaviour of rigid bodies is a well-known topic in the scientific literature. However, there have been many recent and significant developments, such as the study of the seismic response of storage racks (Malhotra (2009) [85]), and the assessment of the existing protocols for shake table testing of freestanding objects (D'Angela *et al.* (2021) [32]). From an experimental point of view, recent researches aim at determining the minimum horizontal acceleration required to activate rocking (Berto *et al.* (2021) [17]).

2.1.2 Base-isolated rocking rigid body

The minimisation of the seismic risk of art objects by base isolation was studied by Vestroni and Di Cinto (2000) [140]. In this respect, high damping laminated rubber bearings were used as isolation devices. The responses of the isolation system were studied in the frequencies and time domains, using recorded accelerograms as input. Aim of the work was the design of the isolation system. The study by Vestroni and Di Cinto was conducted in a parametric way, by varying the numbers of isolators and shear module of the rubber. The response of the isolation system was modelled considering both a linearized system through an equivalent viscous damping and the authors' hysteretic model. In particular, in order to determine the dynamical properties of the isolation system, a linear equivalent force-displacement relationship was used for each isolation device with a stiffness equal to the secant stiffness

at 100% of strain, and viscous damping calibrated in order to equate the dissipated energy on one cycle, with a strain magnitude at 100%, and a frequency equal to the fundamental frequency of the system. The response of the isolated system, modelled as a simple harmonic oscillators characterised by a hysteretic behaviour, was studied. Regarding the nonlinear model for the force-displacement relationship of the isolators, the calibration of the hysteretic parameters was done by way of the experimental force-displacement laws of the rubber bearings. A comparison in terms of shear strain results between the linear and non-linear systems has also been shown. The authors concluded that the differences between the nonlinear analysis results and the linear one depended on the shape of the accelerogram. Moreover, Vestroni and Di Cinto realised that the maximum displacement is acceptable for the limits of the isolators, and stresses acting on the statue are practically negligible.

Caliò and Marletta (2003) [20] studied the vibration passive control of art objects, modelled as rigid bodies freestanding on an isolated-base connected with a visco-elastic device, and subjected to a base acceleration. By using an energy approach, the authors provided a condition able to understand if the rigid body can re-uplift after a collision. They studied the response of the system under pulse excitations, evaluating for both undamped and damped systems the maximum acceleration value that activate the rocking phase. In addition, the authors provided the minimum value of pulse able to causes overturn of a not isolated rigid body with zero polar inertia. Regarding the isolated system, such value was evaluated numerically. The analyses showed that the difference between the minimum pulse start the rocking phase and the pulse causing the overturn, decreases with an increasing period of the isolated system. On the contrary, the minimum pulse that starts the rocking phase increases with increasing the non-isolated system's period. Finally, the response of the base-isolated rigid body under seismic excitations was computed. The results have shown that the unsafe area on the behaviour map of the isolated system is less than the unsafe area of the same not isolated system. Only the isolated system with a very high aspect ratio are able to overturn. Caliò and Marletta (2004) [21], focused their attention on some typical examples of Greek vessel and stone statues representing human figures.

Roussis *et al.* (2008) [109] investigated the dynamic response of a seismically isolated slender statue subjected to a horizontal acceleration. The statue was modelled as a rigid body just able to rock. Both the sliding phase and the vertical component of base acceleration were not considered. The authors concluded by saying that the behaviour of the isolated system strictly depends on the collisions that can change the degrees of freedom of the system as well as modify the kinetic energy.

The influence of the seismic isolation on non-symmetric art objects modelled as rigid bodies was studied by Contento and Di Egidio (2009) [29]. Seismic isolation was modelled as a visco-elastic system. The authors conducted extensive analyses aiming to highlight the performance of the isolation system by varying the eccentricity of the centre of mass and the slenderness of the rigid body. A closed-form solution was obtained for an approximated damped system subjected to a pulse excitation. On the other hand, numerical integration was used when a seismic excitation was used as input. The results have shown a worse performance of the system when the slenderness and the eccentricity of the centre of mass of the body increase.

Di Egidio and Contento (2009) [36] extended their previous study [29] in order to consider the sliding phase and focusing on rigid bodies representing art objects. The frictional forces were expressed by the Coulomb model. The behaviour of the system was studied under the action of two kinds of forces, namely the pulse and the seismic excitation. Finally, they considered two kinds of collapse mechanisms, that is to say, overturning of the rigid body and falling of the body from the isolated base. The analyses were focused on the effect of the coefficient of friction and the eccentricity of the centre of mass. The results have shown that the behaviour of the system is characterised by full-contact and rocking motions when the coefficient of friction is greater than a limit value that depends on the slenderness of the body. Moreover, to establish the benefits of the isolation system, a comparison between the results obtained from both isolated and not isolated rigid body was done. Such comparison showed that the base isolation can be beneficial for art objects.

Vassiliou and Makris (2012) [138] studied the stability of rigid rectangular blocks on an isolated base supported on visco-elastic systems and sliding bearings with both single and double curvature. The authors did not consider sliding motion. First of all, the authors computed six overturning spectra divided into two groups, depending on the slenderness value of the rigid body. For each group, three systems were considered, namely a non-isolated rigid body, a rigid body with a visco-elastic isolation system characterised by a seismic isolation period to a pulse period ratio equal to 2, and a rigid body with a visco-elastic isolation system characterised by a seismic isolation period to a pulse period ratio equal to 3. The viscous damping ratio of the visco-elastic system was assumed equal to 5%, and the mass of the isolated-base was considered equal to 99 times the mass of the body. Finally, the authors considered that all systems were subjected to a symmetric Ricker wavelet excitation. Overturning spectra showed that the base isolation increases the static value of the base acceleration able to start the rocking phase of the non-isolated rigid body. The authors pointed out that this aspect is fundamental for the safeguard of art objects in

which any kind of damage due to impact should be avoided. The same analyses were done considering an antisymmetric Ricker wavelet excitation and the results were compared to the previous ones. From this comparison, the authors declared that the base isolation is beneficial for the small-size rigid bodies; on the contrary, it could be harmful to the large-size rigid bodies. Vassiliou and Makris also studied the influence of the rigid body mass on the base isolation mass ratio. The results of these analyses have shown that for small-size rigid bodies, the rigid body mass to the base isolation mass ratio has no influence on the rocking response. Regarding the single concave sliding bearings, the authors have modelled such isolation system by a bilinear hysteretic model. Overturning spectra of such system were computed and then compared with the overturning spectra of the rigid body with a visco-elastic isolation system. The authors concluded that the response between the two isolation systems was very similar. On the other hand, the double concave sliding bearings were modelled by a trilinear hysteretic model. The computed results with such isolation systems were compared to the results obtained when the isolation system consists of a single concave sliding bearing. Such a comparison led the authors to conclude that the minimum rocking acceleration for the above two-mentioned systems was identical. Finally, the authors have carried out some analyses in order to understand the effect of the isolation system on ancient classical columns. They concluded that the isolation system is beneficial in terms of stability only if the freestanding rigid body has a small size. Consequently, the isolation system impairs the beneficial property according to which stability increases when increasing the size of the rigid body and decreasing the pulse's period.

Berto, Favaretto, and Saetta (2013) [15] investigated the possibility to apply the double concave sliding bearings for the protection of art objects. Thanks to the support of a company leader in the production of anti-seismic devices the authors performed a redesign phase, since they realised that a simple rescaling of the isolation techniques utilized from civil structures to art objects is inappropriate. Then, an experimental campaign was carried out with the goal to characterise the prototypes and to investigate their interaction with four concrete blocks able to simulate the behaviour of the Michelangelo's marble sculptures exhibited in the Galleria dell'Accademia. Finally, some numerical simulations were carried out and, after a calibration phase, the comparison between numerical and experimental results have shown a good agreement in terms of the global response. The authors concluded that from the experimental and numerical results, the isolation system is efficient in terms of limiting transferred inertial force. The influence of the base isolation on the rocking response of the rigid bodies was not investigated.

Ceravolo *et al.* (2016) [24] investigated the semi-active on-off control strategy for the protection of monolithic art objects. To understand the benefits of the semi-active to passive control strategy, the authors evaluated the overturning spectra. The numerical experiments were done by taking into account bodies with different size and slenderness subjected to one-sine pulse. The paper showed that a semi-active control strategy sensibly reduces the overturning area associated with the first mode, that is to say overturn with one or more collisions.

A study on the use of the base isolation for the protection of rigid bodies placed on a multi-floor frame subjected to seismic excitation was carried out by Contento and Di Egidio (2014) [30]. Goal of this work was to understand if base isolation could be beneficial or not for the protection of a rigid body. The authors considered a non-symmetric rigid body able to slide and rock, whereas the frame was considered to work in the elastic regime. In particular, the authors examined the role of the friction coefficient, of the eccentricity of the centre of mass of the rigid body, the role of the period of the base isolation system, of the response on the floor where the object is placed, and finally, the efficiency of the base isolation. The authors concluded that the base isolation for a rigid body placed on a multi-floor frame may not be advantageous in comparison to the same body placed on a fixed base.

A freestanding symmetric seismically base-isolated rigid body able to slide and rock and subjected to a horizontal ground excitation was studied by Roussis and Odysseos (2014) [107]. The isolation system was modelled as a linear visco-elastic system. The nonlinear response of the isolated and non-isolated rigid body under earthquake motion was compared. The authors concluded that base isolation increases the safe area in which the rigid body does not rock. In addition, the failure of the falling rigid body on the pedestal is associated with a larger value of the ground acceleration when the rigid body is isolated.

The dynamic response of a seismically isolated rigid body subjected to a pulse excitation was studied by Roussis and Odysseos (2017) [108]. The authors assumed that the friction coefficient was enough high to prevent sliding. Two isolation systems were considered, namely the linear visco-elastic and the bilinear hysteretic model. The latter was used to reproduce the hysteretic behaviour of a friction pendulum system. They conducted extensive numerical applications in which simple pulses and earthquake excitations of various magnitude and frequency content were used as input. Overturning spectra for both isolated and non-isolated systems were obtained by considering various geometric characteristics in order to understand the advantage of the isolated system with respect to the rocking initiation. They concluded that the isolation system increases the minimum rocking acceleration, an advantage that increases with increasing of the isolation period. This aspect is true regardless of the size of the body and of the pulse

period. However, the use of isolation is better for a body having a small size, for both short and long excitation periods. On the contrary, the isolation system would not be beneficial, for excitation periods greater than one second, for what concerns the stability of the rigid body.

A freestanding ancient classical column on a seismically isolated rigid base was studied numerically by Kavvadias *et al.* (2017) [66]. Friction pendulum sliding bearings were considered as an isolation system. In particular, the authors considered both double and triple friction pendulum bearings. The rocking behaviour of the column, as well as the behaviour of the friction pendulum, were simulated by using the finite element method. The authors investigated the influence of the friction pendulum radius when the column is subjected to earthquake excitation. The results have shown that the triple friction pendulum reduces the acceleration amplitudes of the earthquake excitations characterised by high-frequency content. Moreover, the triple friction pendulum shows better performance than the double friction pendulum when the column is subjected to excitation having a longer main period. However, using both devices, the column will never overturn.

An investigation on the use of active control devices for the protection of art objects was done by Venanzi *et al.* (2018) [139]. The authors provided the suitable equations of the system able to slide and rock but unable to slide-rock simultaneously. Active control was simulated as an actuator connected to the base of the art object and placed in parallel with a spring-dashpot system simulating a passive control system. Numerical analyses were carried out with the aim to show the performance of the active control with respect to the passive control. The results have shown that passive control reduces slide displacements much more than the active one, and it ensures excellent performance from the point of view of rocking response. The authors concluded by saying that passive control could not be efficient when the art object is subjected to intensive earthquakes, whereas active control will be still efficient.

Di Egidio *et al.* (2018) [38] proposed two active control methods able to protect a wide class of rigid bodies. The first method was based on the well-known Linear Quadratic Regulator approach, whereas the second was based on the pole placement method. The former depends only on the state variables of the system, whereas the latter depends also on the external excitation. The optimal control force is obtained for both methods by adopting a linearised system, i.e., a system characterised by a slender rigid body in which the angles of rotation are very small. Both methods are suitable for a wide large class of rigid bodies since they exhibit a very low sensitivity to the variation of the geometrical characteristics of the system. The authors computed the overturning spectra when the rigid body is subjected to a pulse excitation in order to evaluate the effectiveness of the methods. The

overturning spectra have shown that the active control method reduces the overturning area of the block regardless of its slenderness. The authors affirmed that the pole placement method works better than the Linear Quadratic Regulator control method. Moreover, the authors have done several numerical tests using earthquake ground motion as input with the aim to evaluate the performances of the two methods both from the point of view of overturning protection and reducing of rocking angle. The results have shown that the controlled systems are able to avoid overturning of the body. In particular, also in this case, the pole placement method works better than the Linear Quadratic Regulator control method.

Simoneschi *et al.* (2018) [117] focused on the study of the pole placement method to control the rocking motion of rigid blocks.

Kavvadias *et al.* (2019) [67] carried out some seismic fragility analyses of a freestanding marble statue modelled as a rigid body able only to rock. The authors assumed that the statue was placed on the second floor of a two-story reinforced concrete frame building. Moreover, the authors considered two cases of base isolation, both having friction pendulum sliding bearings as isolation devices. In the first case, the building was considered isolated, in the second case, the statue was considered isolated. From the results, the authors have concluded that the base isolation of the statue is more efficient than the base isolation of the building, from what concerns the peak floor acceleration to the peak ground acceleration ratio. The rocking response was also reduced when the base isolation was installed under the statue, rather than under the building.

Thiers-Moggia and Málaga-Chuquitaype (2019) [128] proposed to add supplemental rotation inertia as a seismic control device, in order to reduce the effects of earthquakes on a rigid body able to rock. In particular, this mechanical device was the inerter in which the generated strength is proportional to the relative acceleration between its terminals. The authors developed the equations able to take into account the interaction between the rocking response of the rigid body and the response of the device. The effects of the inerter on the overturning behaviour of rocking bodies subjected to trigonometric pulse excitations were studied by computing the overturning spectra. The authors concluded that the presence of the inerter reduces the areas of overturning and translates them to the lower frequency region. However, the effect of the inerter system on the overturning response is less significant for smaller objects.

The prevention from the overturning response of a rigid body by means of a mass-damper dynamic absorber was investigated by Di Egidio *et al.* (2019) [35]. The mass-damper was modelled as a pendulum hinged at the top of the body. The authors derived the equations of rocking motion as well as the collision conditions. Numerical analyses

were carried out with the aim to understand the performances of the mass-damper on the rocking response of the rigid body subjected to one-sine pulse excitation. Overturning spectra were computed by considering three different values of the pendulum damper's mass. The results have shown that for both values of the pendulum damper's mass, the overturning area is reduced. Moreover, the area related to the first mode, i.e. the overturning area in which the rigid body overturns by exhibiting one or more collisions, will be reduced by increasing the mass of the pendulum damper. Other spectra were computed varying the length of the pendulum damper and it was shown that the behaviour of the system improves when increasing the length of the pendulum damper. However, after a limit value of this quantity, the performances no longer modify. The authors also performed some experimental tests that validated the analytical model as well as the effectiveness of the pendulum mass damper.

Makris and Aghagholizadeh (2019) [82] studied the rocking response of freestanding columns equipped with vertical energy dissipation devices able to dissipate energy by means of hysteretic or viscous (linear or nonlinear) phenomena. The study was focused on a bridge pier. The authors used the constitutive model proposed by Constantinou *et al.* (1998) [28] to simulate energy dissipation by viscous phenomena. On the other hand, to reproduce a hysteretic phenomenon, they used the Bouc-Wen model (Bouc (1971) [19]; Wen (1976) [145]). From the rocking response diagram, the authors concluded that as the size of the column increases, the freestanding column becomes remarkably stable. The benefits of the hysteretic supplemental damping in suppressing the rocking response of the column strictly depends on the kinematic characteristics of the ground motion. In addition, the difference between the damped and undamped response was marginal and, in most cases, the damped response was lower than the undamped one.

Di Egidio *et al.* (2020) [37] focused on the study of the linear quadratic regulator control method for the protection of rigid blocks from overturning.

2.2 MODELLING OF ROCKING RIGID BODY

The rocking rigid body is presented in this Section, outlining its geometrical properties, kinematics, the equations of motion, and the formulation of collisions.

The system here studied is composed by a rigid body simply supported on non-deformable plane. The following assumptions are made: the rigid body is symmetric with respect to the vertical axis and has uniform density; accordingly, the centre of mass is on the vertical axis

of symmetry. Furthermore, as usual in the specialised literature, a 2D model is assumed.

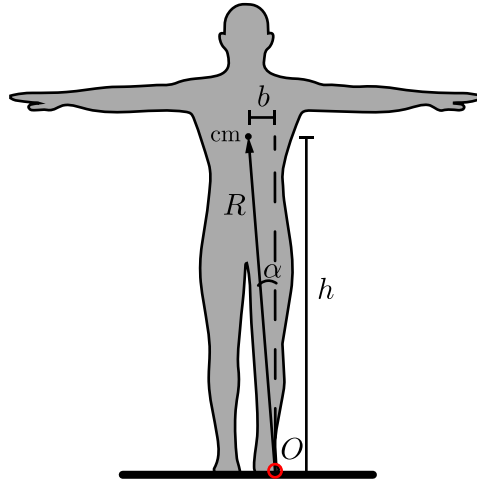


Figure 2.1: Geometrical properties of the rocking rigid body.

In Figure 2.1, the fundamental properties of the body are shown. The horizontal and vertical distances between the centre of mass and one of the two centres of rotation, are denoted as b and h , respectively. Accordingly, the radial distance between the centre of rotation and the centre of mass, is equal to $R = \sqrt{b^2 + h^2}$. The slenderness of the body is measured by the angle $\alpha = \tan^{-1}(b/h)$ that represents the tilt of the radial distance R relative to the vertical. Denoting as m and J_{cm} the mass and the polar inertia about centre of mass of the rigid body, respectively, the polar inertia about rotation axis through one of the two centres of rotation can be computed, applying the *Parallel-Axis Theorem*, as $J_O = J_{\text{cm}} + m R^2$.

2.2.1 Kinematics

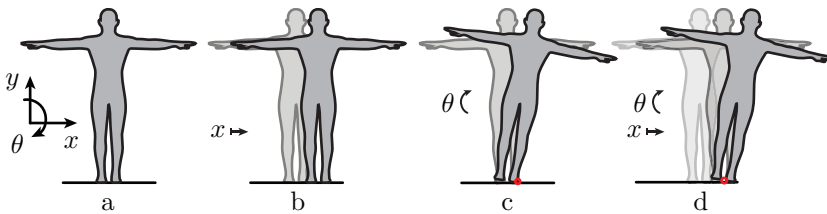


Figure 2.2: Instances of the motion that can occur: (a) Full-Contact; (b) Sliding; (c) Rocking; (d) Slide-Rocking.

We assume that the rigid body can slide over the ground and can rock around one of the two bottom corners. Consequently, the overall degrees of freedom that describe the possible kinematic configurations of the rigid body are two: one relative to the sliding motion, and the other corresponding to the rocking motion. However, these degrees of freedom can be activated both or just one, depending on the behaviour of the rigid body.

Hence, as shown in [Figure 2.2](#), there are overall four phases that the rigid body can undergo: Full-Contact motion (see [Figure 2.2a](#)) where the body does not move; Sliding motion (see [Figure 2.2b](#)) where the body slides on the surface; Rocking motion (see [Figure 2.2c](#)) where the body rocks around one of the two bottom corners; Slide-Rocking motion (see [Figure 2.2d](#)) that represents a combination of the sliding and rocking motions.

In [Figure 2.2](#), the Lagrangian parameters used to describe the above-mentioned phases are also shown. However, the dependence of these Lagrangian parameters on time is omitted for writing convenience. The Lagrangian parameter x describes the horizontal displacement between the body and the ground, see [Figure 2.2b](#), whereas the angle θ , to measure the tilting of the rigid body, see [Figure 2.2c](#). To describe the first and the second derivatives of such Lagrangian parameters respect to the time, that is to say the velocity and acceleration respectively, the Newton's notation is used:

$$\frac{dx(t)}{dt} = \dot{x}, \quad \frac{d\theta(t)}{dt} = \dot{\theta} \quad \text{and} \quad \frac{d^2x(t)}{dt^2} = \ddot{x}, \quad \frac{d^2\theta(t)}{dt^2} = \ddot{\theta}$$

The horizontal and vertical components of the base acceleration acting at the ground are denoted as \ddot{x}_g and \ddot{y}_g , respectively.

The equations of motion are different for each phase that the rigid body can undergo. In the next subsections, we will describe the equations of motion as well as the starting and ending conditions for each phase. To derive the equations of motion, a coordinate system xy is defined, in order to establish the positive directions of displacements, velocities, and accelerations, both linear and angular. The positive direction of x due east and that of y is upward; finally, we assume that clockwise rotations around the reference frame's origin turn have a positive magnitude.

2.2.2 Full-Contact

A Full-Contact phase occurs when no one starting conditions of the other phases occur and when the following initial conditions are null

$$\dot{x}_0 = 0, \quad \theta_0 = 0, \quad \text{and} \quad \dot{\theta}_0 = 0 \tag{2.1}$$

Accordingly, the rigid body does not move in the Full-Contact phase until one of the starting conditions of the other phases occurs or when one of the initial conditions (2.1) is not null.

2.2.3 Sliding

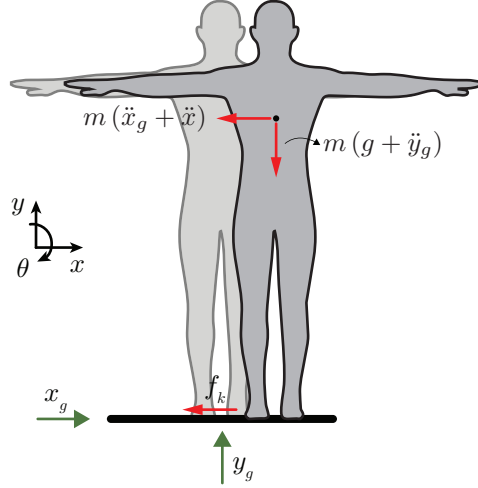


Figure 2.3: Forces acting during the Sliding phase.

In the Sliding phase, the rigid body has one degree of freedom described by the Lagrangian parameter x . The Sliding phase occurs when both initial conditions in terms of angular displacement and velocity are null ($\theta_0 = 0$ and $\dot{\theta}_0 = 0$) as well as when one of the following conditions is satisfied

$$|\ddot{x}_g| \geq \mu_k (g + \ddot{y}_g) \quad (2.2)a$$

$$x_0 \neq 0 \quad \text{and/or} \quad \dot{x}_0 \neq 0 \quad (2.2)b$$

where μ_k is the coefficient of kinetic friction and g is the gravity acceleration. The Equation (2.2)a describes the condition that the inertial force due to the horizontal component of the base acceleration is greater than the frictional force.

The equation of motion that describes the Sliding phase can be obtained by applying Newton's second law to linear motion and balancing all forces acting on the body in the horizontal direction, see Figure 2.3

$$m(\ddot{x}_g + \ddot{x}) + f_k = 0 \quad (2.3)$$

where f_k is the kinetic friction force parallel to the surface and directed so as to contrast the sliding. Such force can be evaluated applying the Coulomb friction law

$$f_k = \mu_k \operatorname{sgn}(\dot{x}) F_N \quad (2.4)$$

in which $\operatorname{sgn}(\dot{x})$ is the signum function of the sliding velocity and F_N is the normal force that in this phase is given by

$$F_N = m (g + \ddot{y}_g)$$

The Sliding phases will end when the sliding velocity approaches zero, i.e. $|\dot{x}| \rightarrow 0$.

2.2.4 Rocking

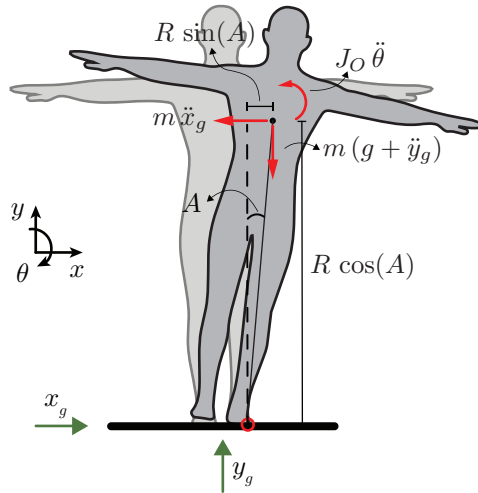


Figure 2.4: Forces and moments acting during the Rocking phase.

The Lagrangian parameter θ is the only degree of freedom activated when the Rocking phase occurs. Since the rigid body is symmetric, the radial distance R as well as the polar inertia J_O are the same for both centres of rotation. Moreover, the change of the sign in θ - when the body switches the centre of rotation - can be taken into account through the signum function $\operatorname{sgn}(\bullet)$. Accordingly, the starting conditions as well as the equation of motion can be written in the same way when the rigid body rocks either around the left or around the right corner.

The Rocking phase can arise when the initial condition in terms of sliding velocity is null ($\dot{x}_0 = 0$) and when one of the following starting conditions is satisfied

$$|\ddot{x}_g| \geq \frac{b}{h} (g + \ddot{y}_g) \tag{2.5a}$$

$$\theta_0 \neq 0 \quad \text{and/or} \quad \dot{\theta}_0 \neq 0 \tag{2.5b}$$

The Equation (2.5)a describes the condition that the overturning moment due to the horizontal acceleration \ddot{x}_g is greater than the resisting moment due to the inertial forces regarding the vertical acceleration \ddot{y}_g and the gravity acceleration g .

The equation of motion that describes the Rocking phase can be obtained by applying Newton’s second law to circular motion and balancing all moments acting on the body, see Figure 2.4

$$J_O \ddot{\theta} + m \ddot{x}_g R \cos(A) + m (g + \ddot{y}_g) R \sin(A) = 0 \tag{2.6}$$

where $A = \text{sgn}(\theta) \alpha - \theta$.

We assume the Rocking phase ends when the angular velocity vanishes after a collision, i.e. $|\dot{\theta}| \rightarrow 0$.

2.2.5 Slide-Rocking

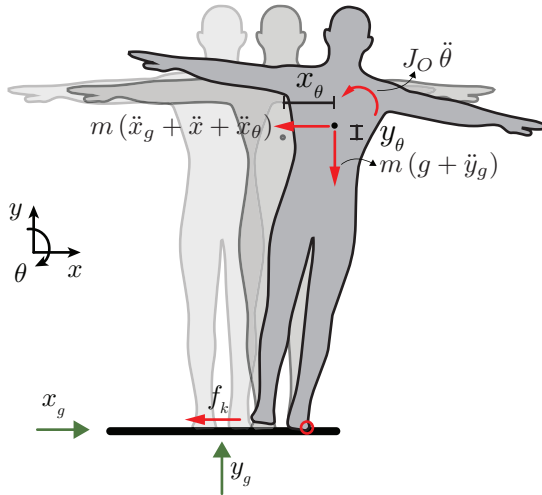


Figure 2.5: Forces and moments acting during the Slide-Rocking phase.

In the Slide-Rocking phase, both degrees of freedom x and θ are activated. The starting conditions depend on from which phase the Slide-Rocking phase arises. From the Full-Contact phase, the Slide-

Rocking phase can take place when the starting conditions of Sliding (2.2) and Rocking (2.5) are simultaneously satisfied, i.e.

$$|\ddot{x}_g| \geq \mu_k (g + \ddot{y}_g) \quad \text{and} \quad |\ddot{x}_g| \geq \frac{b}{h} (g + \ddot{y}_g) \quad (2.7)\text{a}$$

or

$$(x_0 \neq 0 \quad \text{and/or} \quad \dot{x}_0 \neq 0) \quad \text{and} \quad (\theta_0 \neq 0 \quad \text{and/or} \quad \dot{\theta}_0 \neq 0) \quad (2.7)\text{b}$$

The Slide-Rocking phase will start from the Sliding phase if the overturning moment due to the inertial forces regarding the horizontal acceleration \ddot{x}_g and the sliding acceleration \ddot{x} is greater than the resisting moment due to the inertial forces regarding the vertical acceleration \ddot{y}_g and the gravity acceleration g

$$|\ddot{x}_g + \ddot{x}| \geq \frac{b}{h} (g + \ddot{y}_g)$$

On the other hand, the Slide-Rocking phase can arise from Rocking phase if the inertial forces are greater than the frictional forces

$$|\ddot{x}_g + \ddot{x}_\theta| \geq \mu_k (g + \ddot{y}_g + \ddot{y}_\theta)$$

where the accelerations \ddot{x}_θ and \ddot{y}_θ are the second derivative with respect to the time of the horizontal and vertical displacement, respectively, of the centre of mass relative to the ground, see [Figure 2.5](#).

There are two equations of motion that describe the Slide-Rocking phase. These equations can be obtained by applying Newton's second law to both linear and angular motion and balancing all horizontal forces and moments acting on the body, see [Figure 2.5](#)

$$\begin{aligned} m(\ddot{x}_g + \ddot{x} + \ddot{x}_\theta) + f_k &= 0 \\ J_O \ddot{\theta} + m(\ddot{x}_g + \ddot{x}) R \cos(A) + m(g + \ddot{y}_g) R \sin(A) &= 0 \end{aligned} \quad (2.8)$$

where the frictional force f_k can be obtained by using the [Equation \(2.4\)](#). However, the normal force F_N in this phase is computed as follows

$$F_N = m(g + \ddot{y}_g + \ddot{y}_\theta) \quad (2.9)$$

Hence, the [Equation \(2.8\)](#) can be rewritten as

$$m(\ddot{x}_g + \ddot{x} + \ddot{x}_\theta) + \mu_k \operatorname{sgn}(\dot{x}) m(g + \ddot{y}_g + \ddot{y}_\theta) = 0 \quad (2.10)\text{a}$$

$$J_O \ddot{\theta} + m(\ddot{x}_g + \ddot{x}) R \cos(A) + m(g + \ddot{y}_g) R \sin(A) = 0 \quad (2.10)\text{b}$$

The following displacements, strictly related to θ , can be computed as

$$x_\theta = \text{sgn}(\theta) R \sin(\alpha) - R \sin(A) \quad (2.11)a$$

$$y_\theta = R \cos(A) - R \sin(\alpha) \quad (2.11)b$$

Consequently, the first and second derivatives with respect to the time are

$$\dot{x}_\theta = R \cos(A) \dot{\theta} \quad (2.12)a$$

$$\dot{y}_\theta = R \sin(A) \dot{\theta} \quad (2.12)b$$

and

$$\ddot{x}_\theta = R \cos(A) \ddot{\theta} + R \sin(A) \dot{\theta}^2 \quad (2.13)a$$

$$\ddot{y}_\theta = R \sin(A) \ddot{\theta} - R \cos(A) \dot{\theta}^2 \quad (2.13)b$$

The Slide-Rocking phase will end if the ending conditions of the Sliding and Rocking phase are simultaneously satisfied.

2.2.6 Collisions

When the angular displacement θ approaches zero, the rigid body will collide with the non-deformable plane changing the centre of rotation from a corner to the other. Consequently, the rigid body will collide on the ground, changing the dynamic of the motion. Indeed, the kinetic energy of the body after the collision will be less than the kinetic energy before the collision. Hence, the evaluation of the initial condition immediately after the collision is very important for the purpose of the study of a rigid block's behaviour.

The collision condition will be made on the basis of some hypotheses. First of all, we assume that the collision has no effect on the sliding motion. The same hypothesis was assumed by Taniguchi 2002 [126]. Additionally, we assume that after the collision, the body can only be re-uplifted by changing the centre of rotation, i.e. the body does not bounce during the collision. This assumption is motivated by the fact that after each collision a slender body is prone to behave following this assumption [20].

To compare the motion before and after the collision, the law of conservation of angular momentum is used. In fact, although the kinetic energy decreases, the angular momentum remains unchanged. The subscript $(\bullet)_i$ will denote the pre-collision quantities, whereas the subscript $(\bullet)_f$ will identify the post-collision quantities. When the rigid

body rocks around the bottom right corner, the conservation of angular momentum of the bottom left corner gives

$$J_O \dot{\theta}_i - 2 m b R \sin(\alpha) \dot{\theta}_i = J_O \dot{\theta}_f$$

Hence, the post-collision to pre-collision angular velocity ratio is given by

$$e_\theta = \frac{\dot{\theta}_f}{\dot{\theta}_i} = 1 - \frac{2 m b R \sin(\alpha)}{J_O}$$

where the scalar parameter e_θ is called *coefficient of restitution*.

For a rectangular block, $J_O = \frac{4}{3} m R^2$, consequently the above equation can be written as

$$e_\theta = 1 - \frac{3}{2} \sin^2(\alpha)$$

2.3 MODEL EXTENSION TO ROCKING RIGID BODIES SUPPORTED ON BASE ISOLATION

In this Section, the base-isolated rocking rigid body is described, illustrating its kinematics, the equations of motion, and the collisions problem.

Other than the hypothesis of the symmetric rigid body described in the previous Section, we assume that Sliding motion is prevented [43, 75, 99] either assuming that the kinetic friction between the rigid body and the base isolation is sufficiently high or supposing that there are some clip constraints able to prevent the relative horizontal displacement between the rigid body and the base isolation.

The geometrical properties of the rocking rigid body have already been described in the previous Section. The model herein presented is also composed of the base isolation with mass m_b that is connected to the non-deformable plane by means of seismic isolators, see Figure 2.6. Moreover, we assume that the isolators' vertical stiffness was considered far greater than the horizontal one. Consequently, rotation and curvilinear translation of the base are neglected.

2.3.1 Kinematics

Based on the previous assumptions, the system has two degrees of freedom: one relative to the rocking motion of the rigid body, and the other corresponds to the relative translation motion of the base isolation. Nevertheless, depending on the behaviour of the system, the

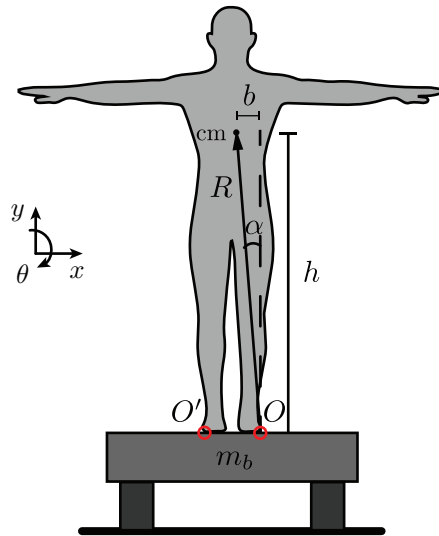


Figure 2.6: Geometrical properties of the seismically base-isolated rigid body.

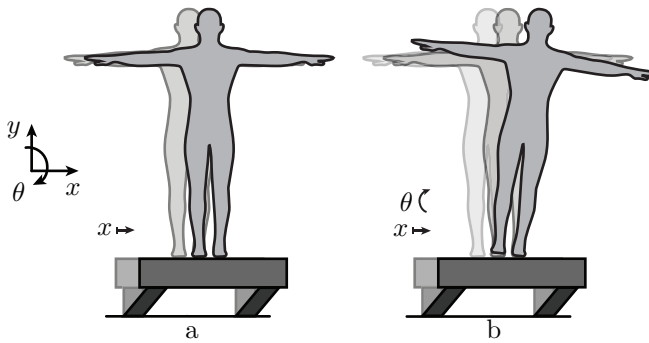


Figure 2.7: Instances of the motion that can occur: (a) Full-Contact; (b) Rocking.

two degrees of freedom are not both activated. Notably, there are two phases of motion: (a) Full-Contact in which the rigid body is in contact with the base isolation, see Figure 2.7a; (b) Rocking in which the rigid body rocks around one of the two centres of rotation while the base isolation moves horizontally as shown in Figure 2.7b.

The Lagrangian parameters that describe the two above-mentioned kinds of motions are the relative displacement between the base isolation and the ground $x(t)$, and tilting of the rigid body $\theta(t)$. According to the Newton's notation, their first and second derivatives with respect to the time are denoted as $\dot{x}(t)$, $\dot{\theta}(t)$ and $\ddot{x}(t)$, $\ddot{\theta}(t)$, respectively.

Horizontal and vertical components of the base acceleration acting on the fixed support are denoted as $\ddot{x}_g(t)$ and $\ddot{y}_g(t)$, respectively. Unless otherwise specified, the dependence on time will be omitted hereafter.

An xy coordinate system has been defined to establish the positive directions of displacements, velocities, and accelerations (see Fig. 2.6). The positive direction of x -axis due right and that of y -axis is upward; finally, we assume that clockwise rotations around the reference frame's origin turn have a positive magnitude.

The equations of motion change according to the kind of motion that the base-isolated rocking rigid body undergoes. Consequently, in the next Subsections, we outline the starting condition as well as the equations of motion for each phase.

2.3.2 Full-Contact

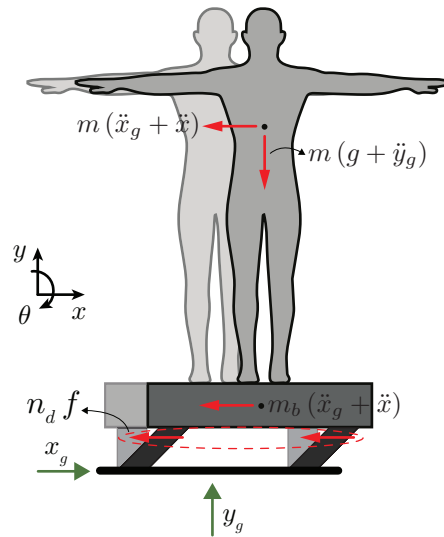


Figure 2.8: Forces and moments acting during the Full-Contact phase.

In the Full-Contact phase, the rigid body has one degree of freedom described by the Lagrangian parameter x . This phase occurs when both initial conditions in terms of angular displacement and velocity are null ($\theta_0 = 0$ and $\dot{\theta}_0 = 0$), and when the starting condition of the Rocking phase is unsatisfied. The latter will be detailed in the next Subsection.

The equation of motion that describes the Full-Contact phase can be obtained by applying Newton's second law of linear motion and balancing all forces acting on the body in the horizontal direction (see Fig. 2.8)

$$(m + m_b) (\ddot{x}_g + \ddot{x}) + n_d f = 0, \quad (2.14)$$

where n_d denotes the number of isolators and f represents the isolator restoring force.

The Full-Contact phase stops when the Rocking phase starts.

2.3.3 Rocking

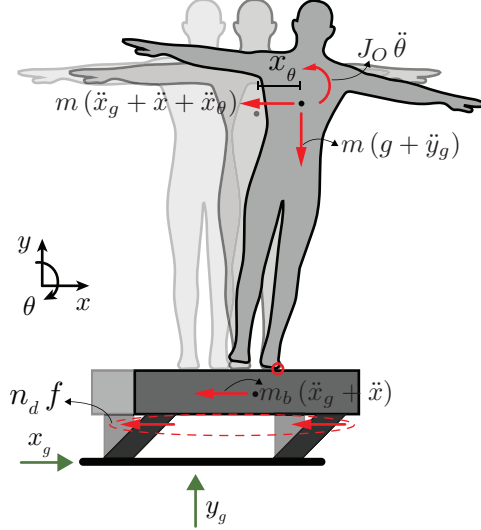


Figure 2.9: Forces and moments acting during the Rocking phase.

Both Lagrangian parameters, namely x and θ , are activated in the Rocking phase. Since the rigid body is symmetric, it is possible to take into account the change of the sign in θ , that is when the body changes the centre of rotation, by means of the signum function $\text{sgn}(\bullet)$. Accordingly, the starting condition as well as the equations of motion are valid when rigid body rocks either around the left or around the right corner.

The Rocking phase can start when the overturning moment due to the inertial forces is greater than the resisting moment due to the gravity acceleration g , namely $|\ddot{x}_g + \ddot{x}| \geq (g + \ddot{y}_g) b/h$, or for $\theta_0 \neq 0$ and/or $\dot{\theta}_0 \neq 0$.

The equations of motion can be obtained by applying Newton's second law of both linear and angular motion and balancing all horizontal forces and moments acting on the body (see Figure 2.9)

$$m(\ddot{x}_g + \ddot{x} + \ddot{x}_\theta) + m_b(\ddot{x}_g + \ddot{x}) + n_d f = 0, \quad (2.15)a$$

$$J_O \ddot{\theta} + m(\ddot{x}_g + \ddot{y}_g + \ddot{x}) R \cos(\text{sgn}(\theta) \alpha - \theta) = -m g R \sin(\text{sgn}(\theta) \alpha - \theta), \quad (2.15)b$$

where \ddot{x}_θ is the second derivative with respect to the time of the horizontal displacement x_θ of the centre of mass of the rigid body with respect to the base isolation, see Equation (2.11)a and Equation (2.13)a.

The rocking phase ends when the angular velocity vanishes after a collision, i.e. $|\dot{\theta}| \rightarrow 0$.

2.3.4 Collisions

When the angular displacement θ approaches zero, the rigid body collides with the base isolation, with a sudden change in its motion. For inelastic collisions, the kinetic energy of the system and the body velocity decrease.

Being the statue a slender body, we assume that after the collision, the body can only re-uplift by changing the centre of rotation, i.e. there is no bouncing of the body on the corner in contact [20].

To obtain the initial condition immediately after the collision, the law of conservation of linear [angular] momentum is used. In fact, although the kinetic energy decreases, the linear [angular] momentum remains unchanged. The subscript $(\bullet)_i$ will denote the pre-collision quantities, whereas the subscript $(\bullet)_f$ will identify the post-collision quantities.

Conservation of angular momentum on bottom corner O' gives

$$\begin{aligned} J_O \dot{\theta}_i - 2 m b R \sin(\alpha) \dot{\theta}_i + m R \cos(\alpha) \dot{x}_i = \\ J_O \dot{\theta}_f + m R \cos(\alpha) \dot{x}_f, \end{aligned} \quad (2.16)$$

and the conservation of linear momentum of the entire system along the horizontal direction gives:

$$(m + m_b) \dot{x}_i + m \dot{x}_{\theta_i} = (m + m_b) \dot{x}_f + m \dot{x}_{\theta_f}. \quad (2.17)$$

Replacing Equation (2.12)a in the Equation (2.17), we obtain

$$(m + m_b) \dot{u}_i + m R \cos(\alpha) \dot{\theta}_i = (m + m_b) \dot{u}_f + m R \cos(\alpha) \dot{\theta}_f. \quad (2.18)$$

In conclusion, the angular and linear velocities after the collision can be obtained by solving Equation (2.16) and Equation (2.18) for the variables $\dot{\theta}_f$ and \dot{x}_f . Accordingly

$$\dot{\theta}_f = \left(1 + \frac{2 b^2 m}{h^2 m \tilde{m} - J_O} \right) \dot{\theta}_i, \quad (2.19)$$

and

$$\dot{x}_f = \dot{x}_i - \frac{2 b^2 h m \tilde{m}}{h^2 m \tilde{m} - J_O} \dot{\theta}_i, \quad (2.20)$$

where $\tilde{m} = m/(m + m_b)$.

Provided that the Rocking phase ceases after a collision, Equation (2.19) and Equation (2.20) are written in the following way

$$\dot{\theta}_f = 0, \quad (2.21)\text{a}$$

$$\dot{x}_f = \dot{x}_i + \tilde{m} R \cos(\alpha) \dot{\theta}_i, \quad (2.21)\text{b}$$

in which the Equation (2.21)b trivially follows from the Equation (2.18) with $\dot{\theta}_f = 0$.

3

SEISMIC PROTECTION TECHNIQUES FOR FREESTANDING ART OBJECTS

This Chapter aims to illustrate classical and modern seismic protection techniques of unanchored museum contents such as statues, amphorae, busts, etc. This topic has received significant interest over the last decade, given that the majority of contents contained in museums are still now not equipped to resist oscillations induced by earthquakes. Although such protection techniques are similar to the ones used to protect laboratory/hospital equipment and electrical transformers, they need to be customised for each artefact to properly account for the museum aesthetic demand.

3.1 RESTRAINT MECHANISMS AND MOUNTS

Assuming that rigid body's kinematics can generally describe the response of the building content, three basic response modes are experienced during an earthquake: moving with the support plane (known as full-contact), sliding and rocking. Obviously, a combination of these responses may also occur.

A large number of art objects belonging to collections can be considered as rigid bodies due to their limited height and deformability. The rocking response should be considered a failure mode because of the possible damages that collisions can cause to the art objects with the support. In addition, the rocking response can attain the limit state of overturning, what can lead to the collapse of the museum content. The sliding motion can also provide damage due to collisions with close objects, even if it is far easier to mitigate than rocking.

Since the building's response can often be controlled only to a limited extent, the best way to mitigate the seismic damage of the collection is to reduce the ground and building oscillations by means of strengthening, supporting, restraining or isolating the collection object. The response limitation of a freestanding object to earthquake motion is a well-known topic in protecting hospital equipment, electrical transformers, commercial store displays, etc.

Similar techniques in protecting museum artefacts by restraints and mounts are utilised. However, each artefact presents unique characteristics so that each technique must be customised to meet the aesthetic demands of exhibition environments.

Restraint mechanisms avoid sliding, rocking, and overturning of the freestanding museum object. However, in this way, the earthquake forces will be directly transferred to the object, and this could cause damage, depending on its degree of fragility. In some cases, if the object is too fragile, allowing it to slide without rocking or overturning, or introducing some form of base isolation, may be the preferred approach [95, 96]. Sliding is achieved by lowering the coefficient of friction between the object and the support plane.

Restraining an object may also involve its connection to a larger and/or heavier mass so that the object assembly will have a more stable geometry and a favourably low centre of mass. An example is a large pedestal or a platform able to increase the footprint of a sculpture and hence increase the aspect ratio and lower the centre of mass of a small object. However, the vertical dynamic forces' magnitude will increase with the increasing object mass until it exceeds the compressive strength of the material or the object's structural integrity. Certainly, the restraint mechanisms need to be sufficiently strong to resist the dynamic forces of the earthquake event. In addition, they should be easily reversible whenever possible. In this Section, we summarise some of the seismic mounts already described in Podany [103]. Consequently, the reader is asked to refer to the above-mentioned papers for a more comprehensive description and further details.

3.1.1 Stops and Clips

Stop restraints represent an easier way to avoid sliding of a small object having stable geometry, i.e. not prone to rocking and overturning. There must be at least three/four stop restraints with a sufficient height to restrict any tilt of the object as shown in [Figure 3.1a](#) in which a vase restrained by three acrylic tabs is depicted. The use of acrylic may not be the best choice due to the stress concentration in the corner. Consequently, during earthquake motion, the restraints could become loose, leaving the object unrestrained. For this reason, metal stop clips, padded at the object interface, would be preferable (see [Figure 3.1b](#)).

Clips are tabs in which the shape is adapted to some part of the object to anchor, e.g. the foot rim of a vase or a statue support base, in order to restrain lateral and vertical movements. Placement, as well as the size and surface area of the clips, need to be designed to distribute the potential stresses to withstand the force imposed by the object during the dynamic motion of the earthquake. In fact, failure of the object at the points where clips are located is the most significant potential

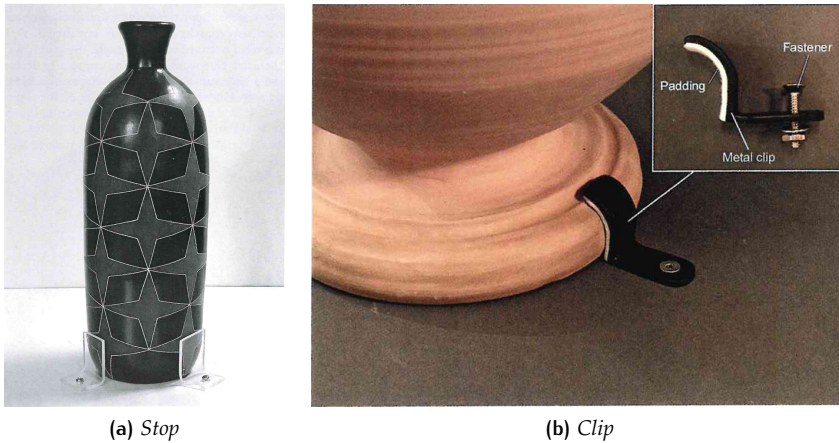


Figure 3.1: Physical restraints: stop and clips [103].

damage. Medium-to large-scale sculpture can also be anchored using clips if the material's strength at the points where clips are located is esteemed to be sufficient, see e.g. Figure 3.2.

3.1.2 Contour mounts

Contour mounts would be preferable when the stresses concentrated in the clips are too high due to the limited geometry. A contour mount is generally vertical, shaped to match the object's profile and has a padded surface to prevent abrasion. The line's path should avoid sharp edges that could break during movements, and it should be in contact with an area of the object that is sufficiently strong. The mount's height should equal the centre of mass' height or a suitable point where the object can anchor with sufficient stability (see Figure 3.3a). Clearly, the line needs to be sufficiently stiff to avoid any plastic deformation during the dynamic load. Two horizontal segments shaped to the circumference of the objects, named arms, can be used to limit the rotational movement around the vertical axis (see Figure 3.3b).

3.1.3 Internal mounts

Mounts are designed to constrain the earthquake movement from the interior when the objects are hollow and there is sufficient space. Figure 3.4 shows a complex stainless steel internal mount to support the cast bronze sculpture, distributing the gravity loads by the surfaces of the shoulders and, at the same time, constraining the sculpture's movement in all directions.

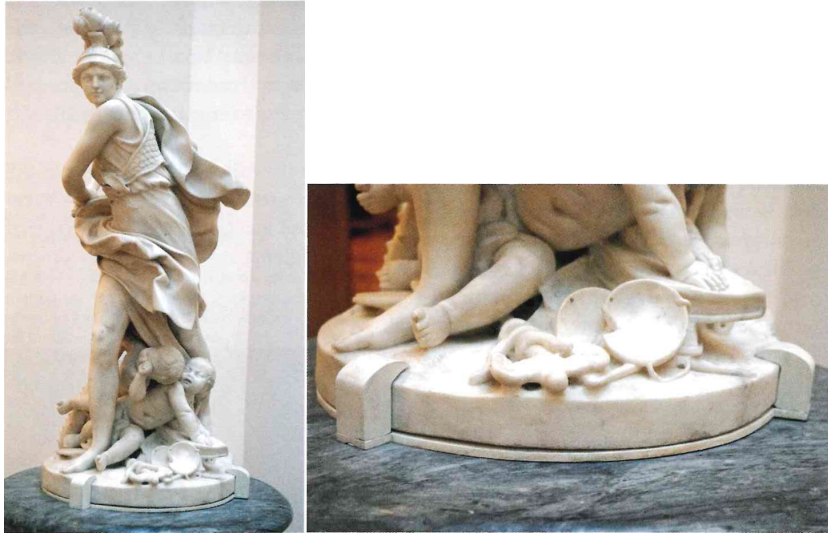


Figure 3.2: Sculpture anchored by clips [103].

3.2 SEISMIC ISOLATION BEARINGS

The use of restraint mechanisms and mounts seen so far can avoid sliding, rocking motion or a combination of both. However, in the majority of cases, this technique can not wholly eliminate the movements in all directions. A mount able to prevent movements in all directions would be so large and intrusive that it would compromise the aesthetic demand. In addition, the price to pay for the use of restraint mechanisms and mounts is that earthquake forces from the ground would be directly transferred to the object through the museum building structure. Hence, the art object needs to be sufficiently strong to resist seismic excitations. The base isolation technique can overcome this limit, protecting unstable or fragile art objects from earthquakes in all directions.

Base isolation is widely used in seismic engineering to protect civil structures and infrastructures from earthquakes. It limits the seismic energy transmitted to the building by eliminating the rigid connection between the ground and the building. Notably, some devices (named isolators) characterised by a reduced stiffness are added. In this way, the fundamental period of the isolated building will shift so as to unmatch the estimated dominant frequency content of the ground motion. The use of base isolation in museums in protecting freestanding art objects is currently unsatisfactory due to their costs and a lack of familiarity with the concept of isolation for small masses. However, the complete reversibility of base isolation and its lower dependence on



Figure 3.3: Contour mounts [103].

direct intervention on the object is of particular importance in the light of modern preservation ethics and guidelines.

3.2.1 Elastomeric Bearings

Elastomeric isolators are one of the most popular types of isolation devices used for seismic protection. They have a circular or square cross section and are made of alternating layers of rubber and thin steel plates that are bonded together by a specific manufacturing process. The reinforcing elements prevent the lateral expansion of the elastomer due to the axial compressive load, whereas the elastomer material provides energy dissipation and flexibility.

The main categories of elastomeric bearings for seismic isolation applications are the Low Damping Rubber Bearings, High Damping Rubber Bearings, and Lead Rubber Bearings [76, 78, 79, 90]. The formers are typically used in coupling with other kinds of isolators (e.g. flat sliders, steel yielding devices, and viscous dampers), due to their limited damping capacity. Consequently, in this Section we analyse the differences only between High Damping Rubber Bearings and Lead Rubber Bearings, with a particular emphasis on the force-transverse displacement (f - x) relationship.



Figure 3.4: A cast bronze sculpture protected by the internal mount [103].

3.2.1.1 Lead Rubber Bearings

The Lead Rubber Bearings (LRBs) are generally characterised by one lead cylinder inserted in a vertical hole into the rubber bearings. The lead cylinder increases the horizontal stiffness in order to limit the horizontal displacements produced by the non-seismic horizontal loads, as well as the energy dissipation capacity. Therefore, the initial tangent stiffness of these devices is approximately 10 times the post-elastic tangent stiffness, and the equivalent viscous damping factor can reach a value up to $\zeta = 15 \div 35\%$ [90]. Several dynamic tests conducted on these kinds of devices show that at strains approaching 200% there is no stiffening behaviour, so that the force-displacement hysteretic loop is bounded between two parallel straight lines [130], see Figure 3.5a.

3.2.1.2 High Damping Rubber Bearings

The High Damping Rubber Bearings (HDRBs) allow one to reach an equivalent viscous damping factor of $\zeta = 10 \div 20\%$ at a shear strain of $\gamma = 100\%$. The shape of the HDRB's force-displacement relationship depends on the value of the applied shear strain. Notably, the shear modulus at low levels of shear strain ($\gamma < 10\%$) can be 5 times greater than the one at shear strain levels of $\gamma \approx 100 \div 150\%$ [27]. For relatively small values of shear strain, namely $\gamma \leq 100 \div 150\%$, the hysteretic loop is bounded between two parallel straight lines. As the shear strain increases ($\gamma > 100 \div 150\%$), a stiffening behaviour is shown [48] and

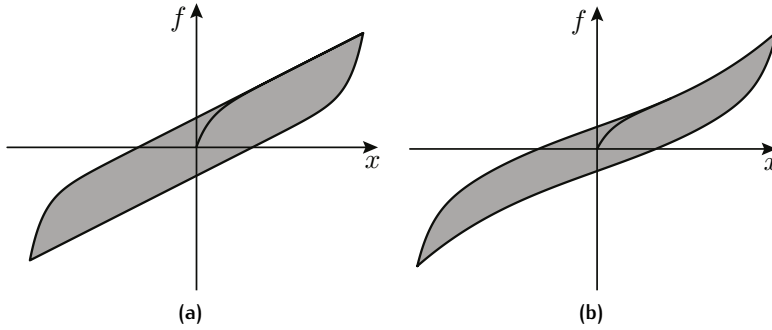


Figure 3.5: Typical hysteretic loops displayed by the main categories of elastomeric bearings for seismic isolation applications: (a) Lead Rubber Bearings; (b) High Damping Rubber Bearings.

consequently, the HDBR's hysteretic loop is bounded between two parallel curves, see [Figure 3.5b](#).

3.3 WIRE ROPE ISOLATORS

Wire Rope Isolators (WRIs) are metal devices that exploit their geometrical and mechanical characteristics in controlling both vibration and shock to isolate sensitive equipment in the areas of aerospace and mechanical engineering [129] as well as for the seismic protection of equipment in buildings [34]. Indeed, reducing the inertia forces applied on lightweight structures by introducing flexible elements, such as elastomeric bearings, could lead to achievement of incompatible displacements with their size. WRIs having different shapes, such as helical, circular, or arch, can absorb a lot of energy input by their damping characteristics that depend, for instance, on the size, number of strands, and wire rope's diameter allowing relatively small displacements. In addition, the WRIs' behaviour also depends on the directions in which they are loaded, namely Shear, Roll, and Tension-Compression.

Base isolation with WRIs has been investigated by Alessandri et al. [3, 4] in protecting high voltage ceramic circuit breakers towards seismic events, demonstrating their effectiveness. A shaking table experimental investigation on a scaled structure seismically isolated by both friction pendulum isolators and WRIs has been studied by Spizzuoco et al. [124]. The authors have shown that WRIs can be helpful to complete recentering of base-isolated structures as well as for limiting displacements.

Experimental frequency responses curves have been employed to study the dynamic behaviour in Tension-Compression direction of a

mass isolated by means of a WRI by Barbieri et al. [14]. Vaiana et al. [136] have carried out several experimental tests, both static and dynamic, on four different WRIs along Shear and Roll directions by using sinusoidal displacements as input having different magnitudes as well as frequencies and under different values of vertical preload. The dynamic performance of WRIs under Tension-Compression direction by using experimental frequency responses curves of both isolated and non-isolated structures has also been investigated by Salvatore et al. [110]. Notably, the isolated (non-isolated) system is experimentally and numerically investigated. In the former case, the system is represented by two symmetric cantilever steel beams with a tip mass and coupled (uncoupled) by a WRI. In the latter, a two-degree-of-freedom system has been considered to model the isolated (non-isolated) structure. The comparisons between experimental frequency responses curves of the isolated and non-isolated structures have shown a severe reduction of transmissibility coefficient in a wide frequency range. In addition, the numerical response of the tested WRI has been modelled by a new phenomenological model of differential nature.

They have also been used to protect the two Riace's bronzes [98], since this isolation system would be particularly suitable when a rocking effect prolongs the fundamental period of the rigid body [3]. Notably, the Archeological Museum of Reggio Calabria has replaced the elastomeric isolators originally installed to protect the two Riace bronzes, known as "Bronze A the young" and "Bronze B the old", with a complex anti-seismic marble basement [22]. The need to replace the base isolation system is due to moving the two statues from the ground floor to the museum's first floor because of the floor amplification of the earthquake accelerations. The new anti-seismic basement is made of marble from Carrara, composed of four spheres also made by marble and WRIs, for horizontal displacement limitation. A vertical isolation system in the upper block of the basement is added since the system does not provide any isolation along the vertical direction, which is typical of most sliding-type designs, see Figure 3.6.

In this Section, a new experimental campaign focused on the dynamic behaviour of four different WRIs loaded along the Tension-Compression direction is proposed. Notably, the experimental campaign is exploited to study the influence of the displacement magnitude and frequency as well as the vertical preload and the wire rope's diameter on the dynamic behaviour of WRIs in both small and large displacements fields. Indeed, the first motivation of such an experimental campaign is that the experimental studies described in [14, 110] are focused on investigating displacement frequency in the field of small displacements. These experimental activities have been carried out in the laboratory of the Department of Structures for Engineering

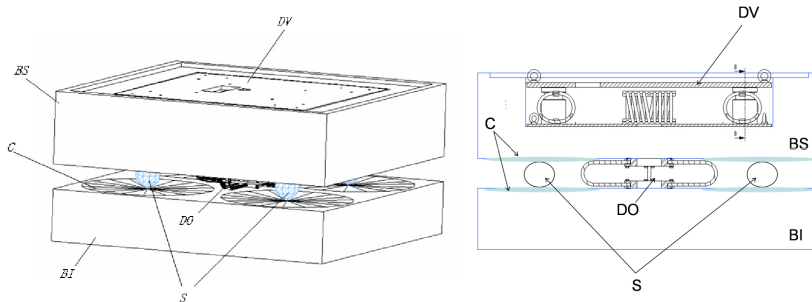


Figure 3.6: Marble anti-seismic basement. BI= marble lower block, S= marble spheres, DO= Horizontal displacement limitation and recentering device, BS= marble upper block, DV=vertical isolation device inserted in the BS upper block [22].

and Architecture of the University of Naples Federico II (Italy) with the collaboration of Prof. G. Serino and Eng. M. Spizzuoco as well as supported by the inter-university consortium ReLUIS.

The tested WRIs are characterised by a wire rope with a helix shape bounded into two aluminium alloy bars, see [Figure 3.7a](#). The wire rope's cross-section is represented by seven strands, six of which are wound around a strand that is the inner core. Each strand has twenty-five wires, except the inner core which is composed of forty-nine wires, see [Figure 3.7b](#). All seven wires are made of stainless steel type 316. The sliding friction is developed between strands and wires, providing good damping properties to the WRI, which will attenuate shocks and absorb vibrations.



Figure 3.7: (a) Helical WRIS, (b) wire rope cross-section.

The experimental campaign is carried out on four different typologies of WRIs, manufactured by Powerflex S.r.l. (Limatola, Italy). Such devices are characterised by different geometrical characteristics listed

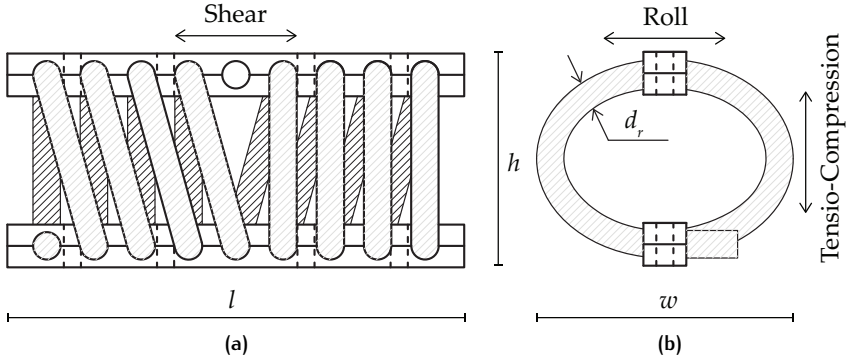


Figure 3.8: Geometrical characteristics and load direction (a) WRI lateral view, (b) WRI cross-section.

in Table 3.1, i.e. the width w , the height h , and the wire rope diameter d_r , whereas the length l is the same, see Figure 3.8.

In the following Subsections, the experimental set-up, and dynamic tests are described.

3.3.1 Experimental set-up

In this experimental campaign, only WRIs' dynamic responses in the Tension-Compression direction is achieved (see Figure 3.8) since those in the two principal horizontal directions, i.e. Roll and Shear directions, have already been investigated by Vaiana *et al.* [136]. These dynamic tests are performed employing the servohydraulic testing machine 810 Material Test System (MTS) model 318.50 (see Figure 3.9a). The load cell for force measurement and control is mounted in the crosshead. Instead, the hydraulic actuator is integrally mounted in the base plate and can reach a maximum force capacity of 500 kN. In addition, the hydraulic actuator includes a displacement transducer for displacement control and measurement. Consequently, both force and displacement

Table 3.1: Geometrical characteristics of tested WRIs, see Figure 3.8 for reference.

WRI	l [mm]	w [mm]	h [mm]	d_r [mm]
PWHS16010	267	100	110	16
PWHS16040	267	125	150	16
PWHS16040s	267	125	150	19
PWHS16060	267	145	185	16

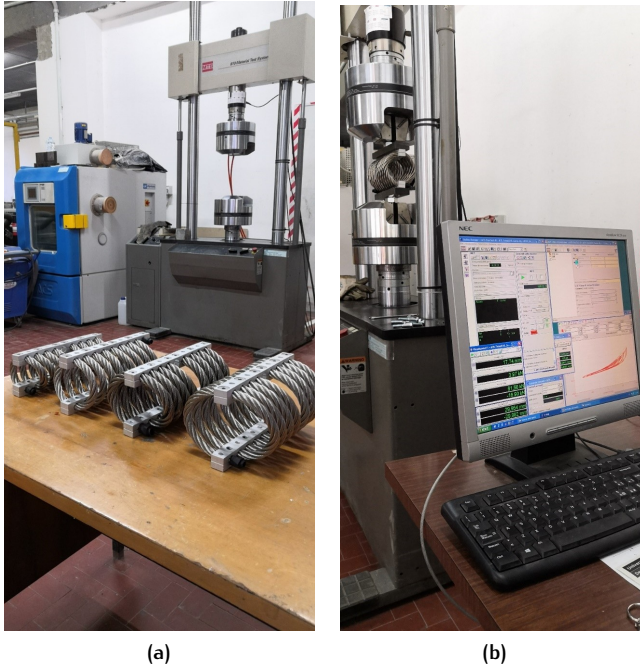


Figure 3.9: Laboratory of the Department of Structures for Engineering and Architecture of the University of Naples Federico II. (a) Servohydraulic testing machine and the tested devices, (b) The grip between a tested WRI and the machine.

controlled procedures are allowed. The grip between the testing machine and WRIs is ensured by two steel bars fixed to each device's upper and lower aluminium alloy bar, see [Figure 3.9b](#).

A total of seventy-one tests in Tension-Compression direction are carried out on the selected devices. Ten cycles of fully-reversed sinusoidal displacement having different magnitudes A_d and frequencies f_r are imposed as input for each test. In addition, different values of the vertical pre-load P_N are considered. Notably, the testing protocol consisted of applying three displacements ranges, that is, small, relatively large, and large. Both maximum displacement and vertical pre-load values reached during the tests are chosen to avoid devices damages. The frequency influence is studied on the PWHS16040 device by varying it from 0.15 to 1.00 Hz, whereas in all other devices, the frequency was 0.10 Hz. In [Table 3.2](#), a more comprehensive description of dynamic tests carried out is listed.

Table 3.2: Dynamic tests in Tension-Compression direction.

WRI	No. of tests	$\pm A_d$ [mm]	f_r [Hz]	P_N [kN]
PWHS16010	6	2.50, 5.00, 7.50, 10.0, 12.5, 15.0	0.10	0.00
	6	2.50, 5.00, 7.50, 10.0, 12.5, 15.0	0.10	2.00
	6	5.00, 10.0, 15.0, 20.0, 25.0, 30.0	0.10	0.00
	6	5.00, 10.0, 15.0, 20.0, 25.0, 30.0	0.10	1.20
	6	5.00, 10.0, 15.0, 20.0, 25.0, 30.0	0.10	2.00
	6	5.00, 10.0, 15.0, 20.0, 25.0, 30.0	0.10	3.00
PWHS16040	3	5.00	0.25, 0.50, 1.00	0.00
	2	10.0	0.25, 0.50	0.00
	2	30.0	0.15, 0.20	0.00
	2	30.0	0.15, 0.20	0.00
PWHS16040s	6	5.00, 10.0, 15.0, 20.0, 25.0, 30.0	0.10	0.00
	6	5.00, 10.0, 15.0, 20.0, 25.0, 30.0	0.10	2.00
PWHS16060	8	5.00, 10.0, 15.0, 20.0, 25.0, 30.0, 35.0, 40.0	0.10	0.00
	8	5.00, 10.0, 15.0, 20.0, 25.0, 30.0, 35.0, 40.0	0.10	2.00

3.3.2 Analysis of results

In this Subsection, the results of the dynamic experimental campaign are presented and discussed. The experimental campaign deals with studying the influence of the displacement magnitude A_d , the vertical pre-load P_N , the frequency f_r , and the wire rope diameter d_r , on dynamic behaviour of WRIs tested in the Tension-Compression direction.

For each of the seventy-one tests, ten force-displacement ($f - x$) hysteresis loops are obtained. The hysteretic behaviour of devices exhibited asymmetry when they are subjected to the Tension-Compression direction. From a mathematical point of view, an asymmetric loop is not described by odd functions with respect to the origin of the reference frame like the symmetric loop. From a mechanical point of view, this is due to the different secant stiffnesses in Tension and Compression. If one of the above-mentioned parameters is modified, WRIs' hysteresis loops will change accordingly. Hence, the four control parameters used to study the dynamic behaviour of tested WRIs in Tension-Compression direction are the following average values: (1) the energy dissipated E_d , (2) the equivalent viscous damping factor ν_e , and (3) the secant stiffness of the peak-to-peak values in the hysteresis loop k_s . These average values are computed on six of ten experimental hysteresis loops because the first three loops are removed due to device settling, while the last loop was not wholly closed.

Two values of the effective secant stiffness are computed due to the asymmetry of the experimental hysteresis loop

$$k_s^+ = \frac{\max(f)}{\max(x)} = \frac{f_{\max}}{x_{\max}}, \quad \text{and} \quad k_s^- = \frac{\min(f)}{\min(x)} = \frac{f_{\min}}{x_{\min}} \quad (3.1)$$

i.e. the two secant stiffnesses of the peak-to-peak values in the first (state of Tension) and third (state of Compression) quadrant, respectively, of the force-displacement plane.

The equivalent viscous damping factor ν_e is generally computed by equating the energy dissipated in one cycle of the existing system and an equivalent viscous system [25], i.e.

$$\nu_e = \frac{1}{4\pi} \frac{E_d}{E_{ev}} \quad (3.2)$$

where

$$E_{ev} = \frac{1}{2} k_s \Delta x^2 \quad (3.3)$$

is the potential elastic energy. However, if the experimental hysteresis loop is not symmetric, Equation (3.3) needs to be changed accordingly. In fact, the secant stiffness in the state of Tension is different from

the Compression one, as explained before. In addition, there is no reason to pick up the maximum relative displacement rather than the minimum one [56]. Consequently, Kumar *et al.* [73] proposed a new approach able to provide a reasonable estimation of the equivalent viscous damping factor when the hysteresis loop is asymmetric. In particular, they modified the term $4 E_{ev}$ in Equation (3.2) in order to take into account the different values of secant stiffnesses in the states of Tension e Compression, yield

$$v_e = \frac{1}{\pi} \frac{E_d}{E_{ev}^I + E_{ev}^{II} + E_{ev}^{III}} \quad (3.4)$$

where the energies E_{ev}^I , E_{ev}^{II} , and E_{ev}^{III} are evaluated in the following way

$$E_{ev}^I = \frac{1}{2} k_s^+ x_{\max}^2, \quad E_{ev}^{II} = f_{\min} x_{\max}, \quad E_{ev}^{III} = \frac{1}{2} k_s^- x_{\min}^2 \quad (3.5)$$

The energy dissipated for each hysteresis loop $E_{d,j}$ with $j = 1, \dots, 6$, is evaluated by the formula (23) in [86], i.e.

$$E_{d,j} = \frac{1}{2} \sum_{i=1}^n \mathbf{r}_i \cdot \mathbf{r}_{i+1}^\perp \quad (3.6)$$

where n is the number of samples that defines the j -th experimental hysteresis loop, \mathbf{r}_i and \mathbf{r}_{i+1} are vectors that identified the i -th and $(i+1)$ -st loop's sample compared to the origin of a Cartesian reference frame. The superscript \perp establishes a rotation of $\pi/2$ of the vector \mathbf{r}_{i+1} in an anti-clockwise or clockwise direction, depending on how the boundary of each loop is parametrised.

3.3.3 Influence of displacement magnitude

Figure 3.10 depicts the relationships of the four control parameters, namely the average energy dissipated, the average equivalent viscous damping factor, and the average secants stiffnesses in the state of Tension and Compression vs the displacement magnitude. Values of the four control parameters obtained from displacement inputs having frequencies equal to 0.1 Hz and without the vertical preload are listed in Table 3.3. From Figure 3.10a and Figure 3.10b, the excellent damping properties of the tested devices are shown. Due to the sliding friction of the stranded cable developed during the deformation of the helix wire rope, a significant proportion of the average energy stored is dissipated with the increase of the displacement magnitude (see Figure 3.10a). The tested WRIs show high values of the equivalent viscous damping factor starting from the range of small displacement. In fact, the biggest

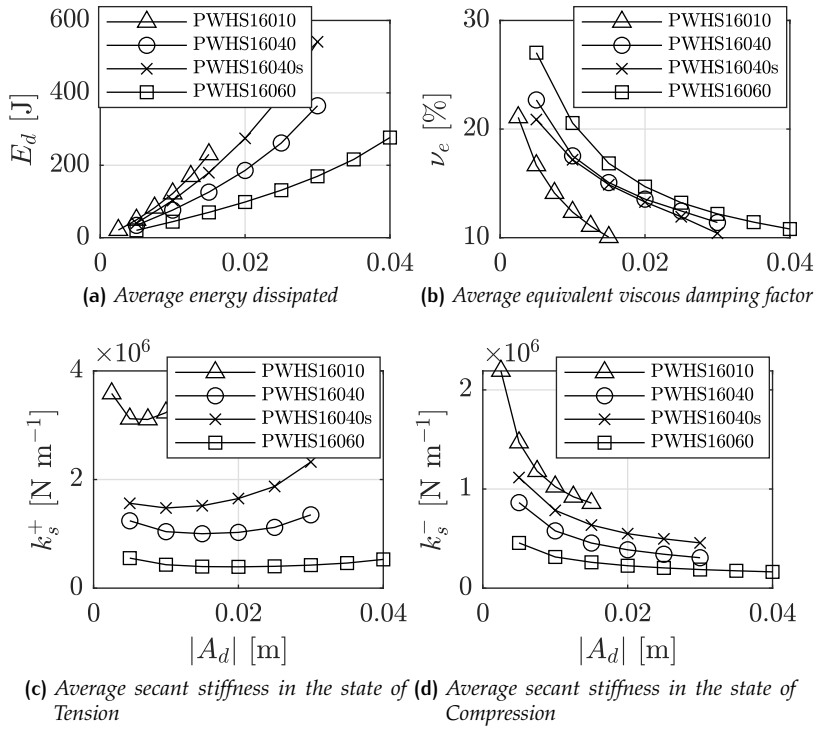


Figure 3.10: The influence of displacement magnitude against the four control parameters.

device, i.e. the PWHS16060, reaches an equivalent viscous damping factor between 25 and 30% in the same range. The equivalent viscous damping factor decreases with increasing displacement magnitude reaching a value of close to 10%, as shown in [Figure 3.10b](#).

As the displacement magnitude increases, stiffening and softening behaviour are displayed in the state of Tension e Compression, respectively (see [Figure 3.10c](#) and [Figure 3.10d](#)). Notably, [Figure 3.10c](#) depicts that the average stiffness in the state of Tension changes its trend showing a convex shape. Consequently, it starts with a high value in the range of small displacements, the it decreases in the relatively large one and finally it increases in the large displacements field. On the contrary, the average secant stiffness in the state of Compression decreases when the displacement magnitude rises, as shown in [Figure 3.10d](#).

Hysteresis loops of each device obtained for four different displacement magnitudes are shown in [Figure 3.11](#). The high asymmetry of tested devices' behaviour is clear, and it varies with changing of the displacement range. Notably, in the field of small displacements, softening in Compression and a moderately hardening behaviour in Tension

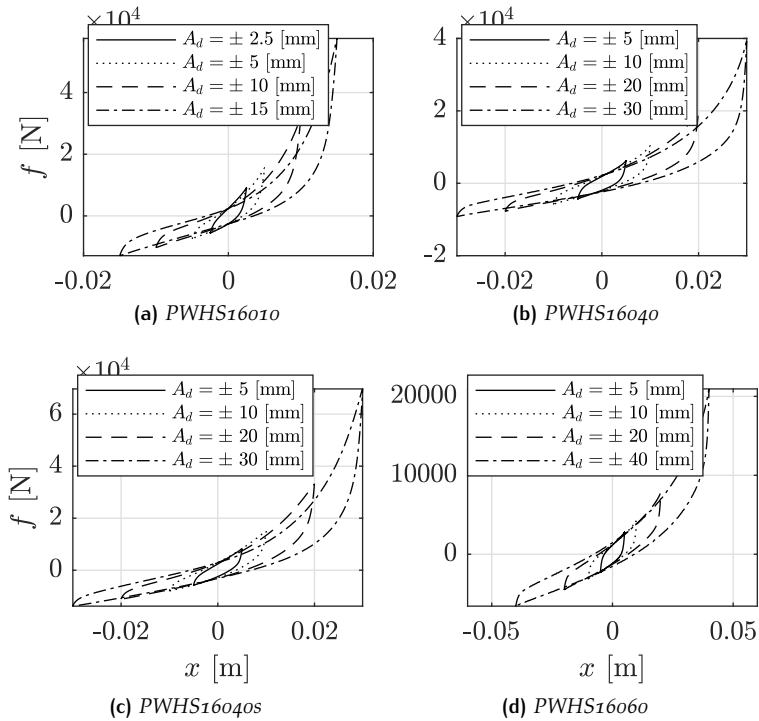


Figure 3.11: Influence of displacement magnitude - hysteresis loops.

are shown, whereas at large displacements, experimental loops show a pronounced hardening behaviour in the state of Tension.

3.3.4 Influence of vertical preload

The vertical preload effect on the dynamic behaviour of PWHS16040 device is shown in Figure 3.12. The four control parameters are obtained from dynamic tests with displacement inputs having frequencies equal to 0.1 Hz and magnitude varying from 5 to 30 mm. From Figure 3.12a and Figure 3.12b, one can observe that the vertical preloads effect does not significantly change the energy dissipated and the equivalent viscous damping factor than those without the preload. However, a slight increase (decrease) is shown in the energy dissipated (equivalent viscous damping factor) at large displacements.

The most interesting result is in the variation of the two secant stiffnesses shown in Fig. Figure 3.12c and Figure 3.12d. The average secant stiffnesses in the state of Tension and Compression at small displacements decrease with the increase of the vertical preload. On the other hand, only the average secant stiffness in the state of Tension increases

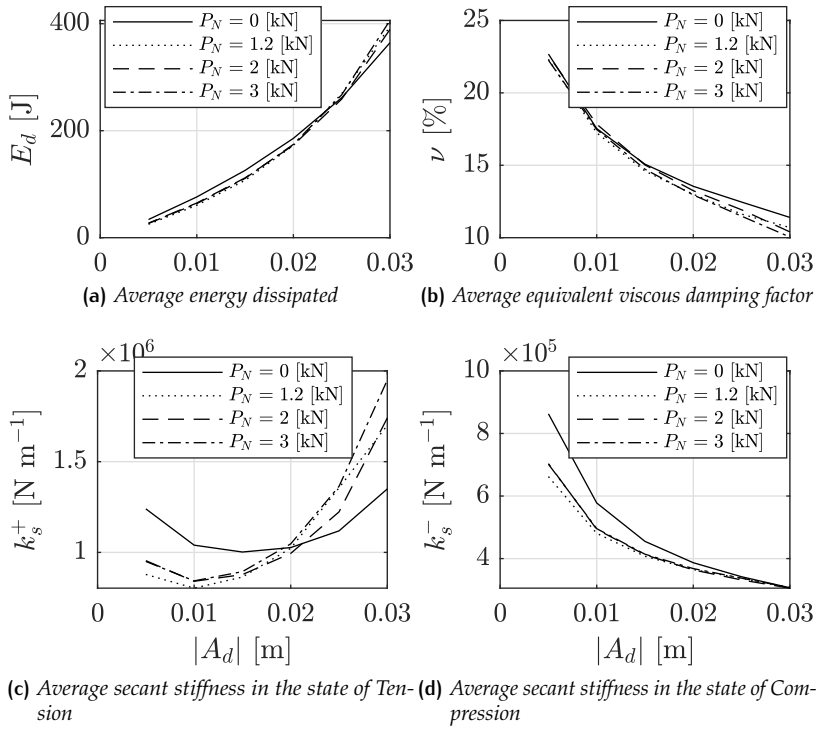


Figure 3.12: Influence of pre-axial load magnitude on the dynamic behaviour of the PWHS16040 device.

at large displacements while the one in the state of Compression does not change.

Figure 3.13 depicts the PWHS16040 device's two hysteresis loops obtained by applying sinusoidal displacements having a magnitude equal to 10 mm (Figure 3.13a) and 30 mm (Figure 3.13b). The hysteresis loop exhibits a clockwise rotation in the range of small displacements when a vertical preload is applied without changing its area (see Figure 3.13a). On the other hand, in the range of large displacements (Figure 3.13b), with increasing of the vertical preload, stiffening behaviour in the state of Tension is displayed, while the secant stiffness variation in the state of Compression is negligible.

For readers reference, the PWHS16040 device's values of the four control parameters show in Figure 3.13 are listed in Table 3.4.

3.3.5 Influence of frequency

In Figure 3.14, the PWHS16040 device's four control parameters versus displacement frequencies is depicted. These tests regard sinusoidal

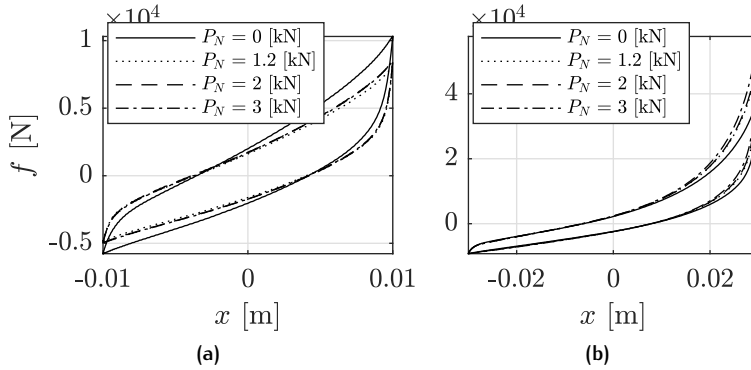


Figure 3.13: PWS1604 hysteresis loops: influence of vertical preload. (a) displacement magnitude equal to 10 mm; (b) displacement magnitude equal to 30 mm.

displacements having different magnitude's values and without the effect of the vertical preload.

In the small displacements range, that is when the displacement magnitude in absolute value varies between 5 and 10 mm, WRIs show an independent rate behaviour. Notably, in this range the variation of the average energy dissipated, average viscous damping factor, and average secant stiffness in the state of Tension are negligible (see from [Figure 3.14a](#) to [Figure 3.14c](#)). In comparison, the variation of the average secant stiffness in the state of Compression is small (see [Figure 3.14d](#)). However, the PWS16040 device shows a rate dependent behaviour at large displacements since an increase in the input frequency determines a decrease in the average equivalent viscous damping factor. Simultaneously, average energy dissipated and the average secant stiffness in the state of Tension increase. On the other hand, the average secant stiffness in the state of Compression remains negligible with increasing of input frequency.

It must be pointed out that, assuming the frequency of the applied sinusoidal displacement, as control parameter for different amplitudes of the hysteresis cycle, presents some limitations since the displacement rate along the cycle depends on the amplitude. Comparisons between cyclic ramps and homeomorphisms applied to the ramp histories would have been more appropriate, as shown in [5].

[Figure 3.15](#) shows PWS16040 device's hysteresis loops obtained in ranges of small and large displacements, see [Figure 3.15a](#) and [Figure 3.15b](#), respectively. By increasing the input frequency, a pronounced hardening behaviour in the state of Tension in large displacements range is shown (see [Figure 3.15b](#)). In contrast, the frequency effect on the tested WRI is much less at small displacements ([Figure 3.15a](#)).

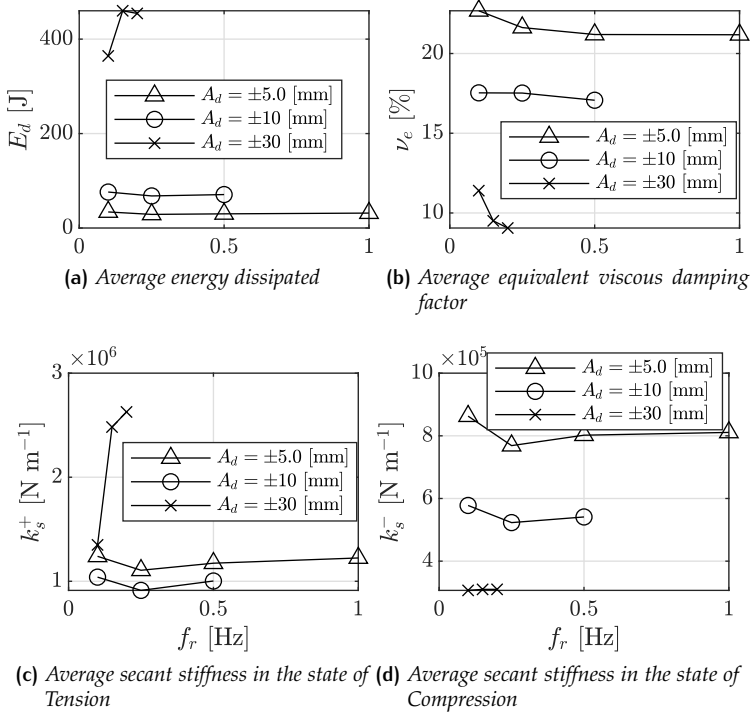


Figure 3.14: Influence of frequency input on the dynamic behaviour of the PWHS16040 device.

In Table 3.5, the four control parameters variations by varying the input frequency are listed.

3.3.6 Influence of wire rope diameter

To study the influence of the helix cable diameter on the dynamic behaviour of the tested device, a special WRI named PWHS16040s is manufactured by Powerflex S.r.l. Geometrical characteristics of this device are the same as the PWHS16040, but its wire rope has a bigger diameter of 19 mm.

The four control parameters variations of PWHS16040 and PWHS16040s devices by varying the displacement magnitude are shown in Figure 3.10 and listed in Table 3.3. In terms of energy dissipated, the PWHS01640s provides more dissipation than the PWHS16040 one, mainly in large displacements range, see Figure 3.10a. However, Figure 3.10b shows that PWHS01640s and PWHS16040 devices' equivalent viscous damping factors are very close to each other. The use of a

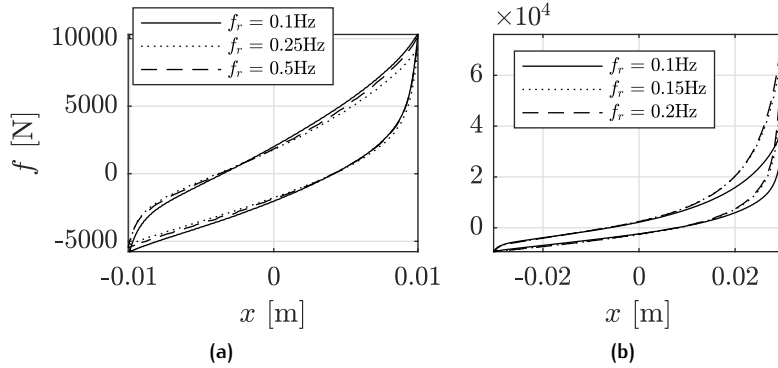


Figure 3.15: PWS16040 hysteresis loops: influence of frequency. (a) displacement magnitude equal to 10 mm; (b) displacement magnitude equal to 30 mm.

WRI with a bigger wire rope diameter provides a stiffer behaviour (see [Figure 3.10c](#) to [Figure 3.10d](#)).

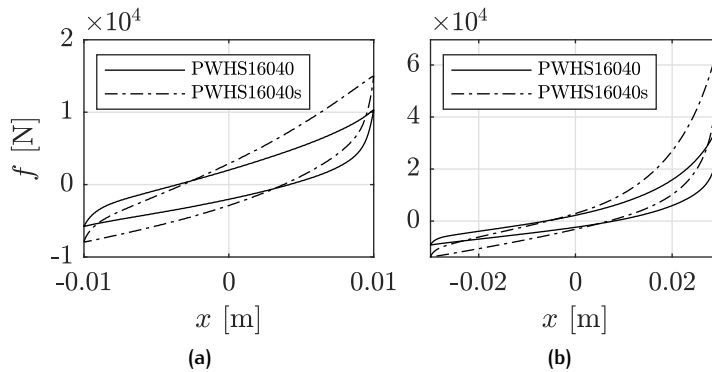


Figure 3.16: PWS16040 and PWS16040s hysteresis loops: influence of wire diameter. (a) displacement magnitude equal to 10 mm; (b) displacement magnitude equal to 30 mm.

[Figure 3.16](#) depicts a comparison between PWS16040 and PWS16040s devices' hysteresis loops by applying sinusoidal displacements having a frequency equal to 0.1 Hz as well as a magnitude equal to 10 mm ([Figure 3.16a](#)) and 30 mm ([Figure 3.16b](#)). One can observe that using a bigger wire rope diameter provides a clockwise rotation of hysteresis loops in both displacements ranges. Notably, a stronger (slight) hardening behaviour in the state of Tension (Compression) is reached in the large displacements range.

Table 3.3: Values of the four control parameters to vary the displacement magnitude.

WRI	$ A_d $ [mm]	E_d [J]	ν_e [%]	k_s^+ [N m ⁻¹]	k_s^- [N m ⁻¹]
PWHS16010	2.50	20.99	0.21	3 585 123.75	2 191 470.63
	5.00	49.16	0.17	3 119 743.41	1 469 256.41
	7.50	82.65	0.14	3 106 036.44	1 180 324.04
	10.00	121.93	0.12	3 232 201.89	1 023 735.77
	12.50	169.94	0.11	3 508 399.43	921 542.40
	15.00	230.12	0.10	3 927 754.13	858 068.72
PWHS16040	5.00	34.00	0.23	1 239 833.07	862 817.39
	10.00	76.17	0.18	1 039 863.34	577 751.89
	15.00	125.77	0.15	1 002 063.50	454 971.34
	20.00	185.69	0.14	1 026 558.77	386 783.21
	25.00	261.52	0.12	1 118 603.30	341 938.16
	30.00	364.39	0.11	1 349 757.42	306 696.66
PWHS16040s	5.00	40.05	0.21	1 562 512.45	1 116 002.93
	10.00	102.66	0.17	1 476 127.11	784 690.12
	15.00	179.37	0.15	1 516 863.12	636 422.67
	20.00	274.30	0.13	1 649 963.54	549 682.27
	25.00	392.14	0.12	1 872 386.91	497 321.13
	30.00	540.99	0.10	2 323 543.62	456 398.68
PWHS16060	5.00	20.29	0.27	552 790.57	456 122.39
	10.00	44.20	0.21	431 444.16	314 430.14
	15.00	69.88	0.17	396 795.24	260 682.53
	20.00	98.51	0.15	392 316.32	226 005.83
	25.00	131.09	0.13	401 782.82	204 175.00
	30.00	169.56	0.12	423 994.22	187 658.19
	35.00	216.21	0.11	461 753.37	175 001.52
	40.00	276.58	0.11	529 453.11	164 190.40

Table 3.4: Values of the four control parameters by varying the vertical preload.

P_N [kN]	$ A_d $ [mm]	E_d [J]	ν_e [%]	k_s^+ [N m ⁻¹]	k_s^- [N m ⁻¹]
0.00	5.00	25.02	0.22	878 458.80	662 183.15
	10.0	60.57	0.17	803 034.94	480 625.14
	15.0	107.23	0.15	864 219.38	407 361.23
	20.0	172.41	0.13	1 022 774.83	364 902.84
	25.0	269.20	0.12	1 355 712.32	336 789.36
	30.0	394.49	0.11	1 700 831.74	306 114.64
2.00	5.0	27.14	0.23	954 460.56	703 519.08
	10.0	64.80	0.18	840 853.36	493 520.20
	15.0	111.86	0.15	877 688.71	412 189.37
	20.0	173.01	0.13	994 516.88	363 799.73
	25.0	258.96	0.12	1 223 163.55	331 753.31
	30.0	389.19	0.10	1 740 710.29	305 507.54
3.00	5.0	26.65	0.22	950 129.21	701 728.60
	10.0	63.73	0.17	843 190.25	495 738.51
	15.0	110.88	0.15	894 082.83	413 929.99
	20.0	174.41	0.13	1 046 871.92	367 988.08
	25.0	267.05	0.11	1 363 805.01	337 428.69
	30.0	406.07	0.10	1 949 439.62	307 438.71

Table 3.5: Values of the four control parameters by varying the input frequency.

$ A_d $ [mm]	f_r [Hz]	E_d [J]	ν_e [%]	k_s^+ [N m ⁻¹]	k_s^- [N m ⁻¹]
5.00	5.00	34.00	0.23	1 239 833.07	862 817.39
	10.00	28.83	0.22	1 105 776.33	768 727.03
	15.00	30.00	0.21	1 173 739.18	802 021.09
	20.00	31.59	0.21	1 224 042.42	810 869.43
10.00	5.00	67.93	0.18	912 482.22	522 995.96
	10.00	70.83	0.17	1 002 573.43	541 049.84
30.00	5.00	460.01	0.10	2 482 322.51	309 912.89
	10.00	454.40	0.09	2 627 236.24	310 046.85

4

MATHEMATICAL MODELLING FOR SIMULATING MECHANICAL HYSTERESIS PHENOMENA

Hysteresis is a complex phenomenon that can be experienced in many fields of science and technology; undoubtedly it represents the predominant typology of nonlinear constitutive behaviour. The importance of properly reproducing hysteretic responses in engineering has been highlighted by several contributions available in the literature. The main research field include civil applications, magnetism and mechanics [141]. Beyond basic applications such as the modelling of seismic devices, dampers and concrete, hysteresis plays a significant role also for the analysis of more complex mechanical systems including applications concerning framed and shell structures, structural identification and random vibrations [8, 145].

The output of hysteresis systems and materials typically depends on present and past histories of the input variable and can exhibit different peculiar features: in particular, when the first time derivative of the input variable does not influence the output, this hysteresis phenomenon is denominated *rate-independent*.

The development of mathematical models able to describe such nonlinear phenomena is very complicated. In particular, in the last few years many researchers have proposed different models whose common objective was not to explain the physical origin of the hysteresis but to try to reproduce the overall experimental behaviour [87]. These models are called *phenomenological* models.

It is possible to classify the phenomenological models according to the nature of the equation to solve for the evaluation of the output variable, namely the generalised force or the generalised displacement. In particular one has:

- algebraic models, such as the ones developed by Ramberg and Osgood [106], Menegotto and Pinto [88], and Vaiana et al. [134, 135];
- transcendental models, as the ones introduced by Kikuchi and Aiken [68], and Vaiana et al. [133];

- differential models, such as those formulated by Bouc [18, 19], Özdemiş [151], and Wen [145, 146];
- damage-based models, as the one proposed by Valoroso and Fedele [137].

Among existing models, the differential ones are currently the most used models to reproduce the behaviour of mechanical systems and materials. These models are typically based on the Duhem hysteresis operator [45] whose formulation is defined by a Cauchy problem of the form:

$$\begin{cases} \dot{z}(t) = g_1(x, z) \dot{x}(t)^+ + g_2(x, z) \dot{x}(t)^-, \\ z(0) = z_0, \end{cases}$$

in which $z(t)$ and $x(t)$ denote the hysteretic functions and the generalised displacement, respectively, and the superimposed dot denotes the derivative with respect to time t ; g_1 and g_2 are continuous functions whereas $\dot{x}(t)^+ = \max(0, \dot{x}(t))$ and $\dot{x}(t)^- = \min(0, \dot{x}(t))$; finally z_0 represents the value of the function $z(t)$ at the time $t = 0$. All models based on Duhem's class are characterised by a peculiar property: the output value can be evaluated if the current values of the input and output variables (x, z) as well as the sign of the first derivative with respect to time of the input variable ($\text{sgn}(\dot{x})$) are known [40]. Examples of differential models based on Duhem hysteresis operator are the ones proposed by Jiles-Atherton [65], Coleman-Hodgdon [57], Bouc-Wen [19, 145, 146], and Özdemiş [151].

4.1 THE CLASS OF BOUC-WEN DIFFERENTIAL MODELS

This Section aims to illustrate the evolution of the Bouc-Wen model in the area of mechanics. In particular such an evolution is described with reference to the modelling of symmetric and asymmetric hysteresis loops, hysteresis loops with pinching and hysteresis loops with strength and/or stiffness degradation typically displayed by *rate-independent* mechanical systems and materials. The influence of the input parameters on the dimension and/or shape of the hysteresis loops is shown and discussed for each hysteretic model.

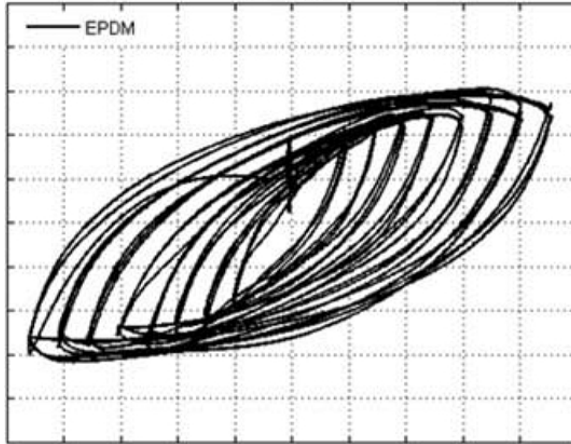


Figure 4.1: The symmetric hysteresis loop of a bearing - H. A. Hadad et al. [55].

4.1.1 Modelling of symmetric hysteresis loops

From a mathematical point of view, symmetric hysteresis loops are characterised by odd functions with respect to the origin of the reference frame, i.e. hysteretic functions z fulfilling the condition

$$z(x) = -z(-x).$$

Among several mechanical systems and materials that exhibit a nonlinear behaviour characterised by symmetric hysteresis loops, we recall, as an example, the typical cross section of steel and concrete filled steel elements, metal devices, such as wire rope isolators deforming along their transverse directions [136], seismic protection devices, such as isolators [54, 77, 79, 131, 134] and dampers [91]. In Figure 4.1 an example of symmetric hysteresis loop obtained in experimental tests is shown.

The restoring force of the above described mechanical systems and materials is typically computed as follows:

$$f(x) = f_e(x) + f_h(x),$$

where $f_e(x)$ is the elastic component whereas $f_h(x)$ is the hysteretic one. In turn the restoring force can be described in the following way:

$$f(x) = \chi k x + (1 - \chi) k z,$$

in which χ is ratio between the post-yield and pre-yield stiffness whereas k is defined as the stiffness at yield, i.e. the ratio between the yield force and the generalised yield displacement.

4.1.1.1 Bouc model and its modified versions

The full class of Bouc models is described by the following general nonlinear first-order ordinary differential equation:

$$\dot{z} = B \dot{x} \quad (4.1)$$

in which \dot{z} denotes the time derivative of the hysteretic variable, required to evaluate the rate-independent hysteretic component $f_h(x) = (1 - \chi)kz(x)$, whereas \dot{x} is the generalised velocity. The hysteretic function z basically depends on the system behaviour, material properties and response amplitude.

The nonlinear function B has been assumed of different form over the years [18, 19]:

$$\text{Bouc model 1 (1967):} \quad B = A - z\beta \operatorname{sgn}(\dot{x}), \quad (4.2)$$

$$\text{Bouc model 2 (1967):} \quad B = A - |z| \left(\gamma + \beta \operatorname{sgn}(\dot{x}z) \right), \quad (4.3)$$

$$\text{Wen model (1976):} \quad B = A - |z^n| \left(\gamma + \beta \operatorname{sgn}(\dot{x}z) \right) \quad (4.4)$$

where A , n , and γ are material parameters that tune the size and/or the shape of the hysteresis loops.

Equation (4.2), that defines the original Bouc model, is characterised by two model parameters, namely A and β . Subsequently, Bouc has modified such an equation by adding a new parameter, that is γ , as shown in Equation (4.3). Finally, Wen has extended the class of the Bouc differential models by adding the parameter n in order to smooth the hysteretic curve predicted by the original Bouc model. Note that equation $f(x) = \chi kx + (1 - \chi)kz$, and Equation (4.4) define the so called Bouc-Wen model.

The smooth nature of the Bouc model modified by Wen makes it particularly convenient for addressing several engineering problems especially when several dynamic analyses are required. This includes the case of flutter analysis [23] and random vibration analysis of structures.

The Bouc-Wen model is capable of reproducing several behaviours depending on the parameters A , β , γ , and n , whose influence on the hysteretic variable z is illustrated in Section 4.1.1.2.

4.1.1.2 Sensitivity analysis

A parameter sensitivity analysis was carried out to evaluate the effect of each parameter on the hysteretic variable $z(x)$ obtained by adopting Equation (4.1) and Equation (4.4).

The relationship between the hysteretic variable z and the generalised displacement x , is shown in Figure 4.2 for different combination of the

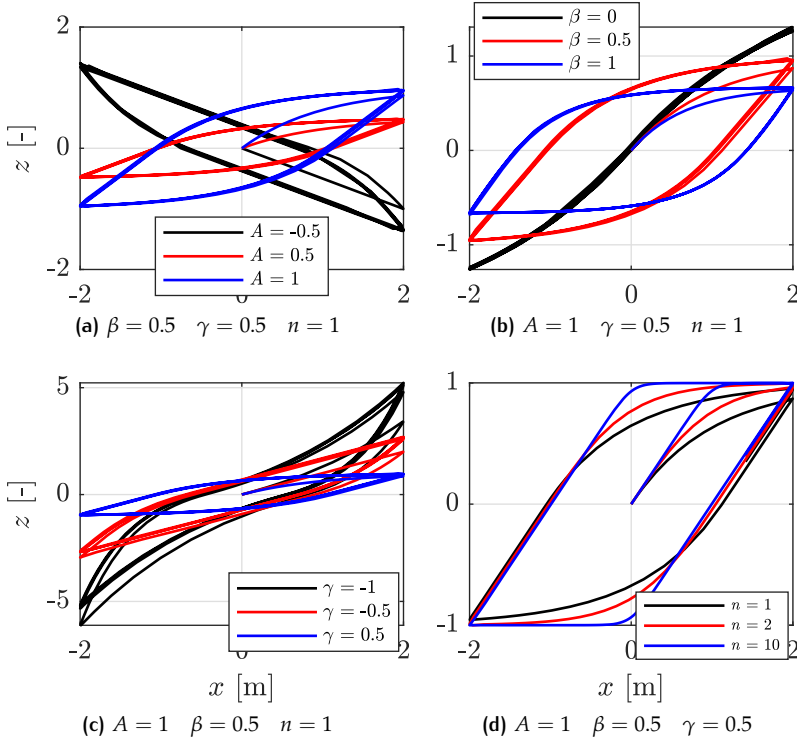


Figure 4.2: Sensitivity analysis of the Bouc-Wen model with respect to the material parameters.

constitutive parameters. All hysteretic loops are obtained by applying a generalised displacement described by the following sine wave:

$$x(t) = 2 \sin(t) \quad (4.5)$$

and integrating the differential Equation (4.1) by MATLAB[®] using the solver ode45.

The Figure 4.2a shows that the tangent stiffness at the origin of the hysteresis loop increases when the parameter A is increased and its sign is the same as that of A ; for negative values of parameter A , the tangent stiffness at the origin becomes negative.

The Figure 4.2b shows that the hysteretic energy dissipation increases as β increases. In particular, an elastic nonlinear constitutive law can be obtained by setting $\beta = 0$.

The Figure 4.2c shows that the hysteresis loop is bounded between two parallel straight lines and it rotates clockwise when the parameter γ is increased. On the other hand, by decreasing the value of γ , the hysteresis loop is bounded by two parallel curves such that, for

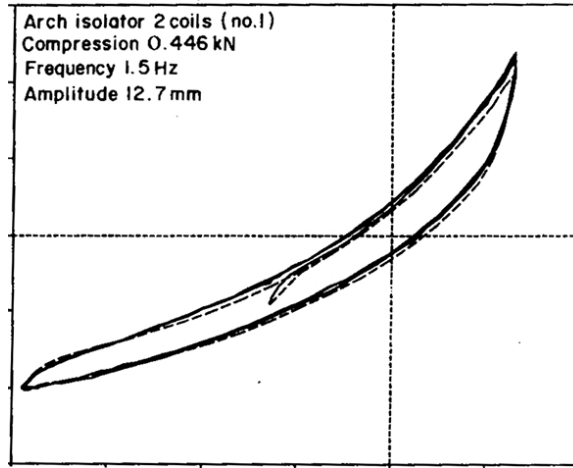


Figure 4.3: The asymmetric hysteresis behaviour of a wire rope isolator along their axial direction - G. F. Demetriades et al. [34].

high values of the displacement x , the hysteresis loop exhibits a work hardening behaviour.

Finally, the Figure 4.2d shows that the hysteresis loop gets smoother with decreasing n so that such a parameter can be related to the smoothness of the hysteresis loop. In the limit case $n \rightarrow \infty$, the constitutive law becomes elastic-perfectly plastic.

4.1.2 Modelling of asymmetric hysteresis loops

There exist several mechanical systems and materials displaying a non-linear response characterised by asymmetric hysteresis loops; typical examples are some materials, such as metals [44], polymers [59] and shape memory alloys [53], as well as some devices, such as wire rope isolators deforming along their axial direction [34]. Asymmetric hysteresis loops obtained in experimental tests and retrieved from the literature are shown in Figure 4.3.

4.1.2.1 Asymmetric Bouc-Wen models

The differential models described in Section 4.1.1 are not able to reproduce rate-independent asymmetric hysteresis phenomena. Hence, to simulate the typical asymmetric hysteresis loops, some researchers [119, 122, 144] have proposed the following generalised expression for the function:

$$B = A - |z^n| \Psi, \quad (4.6)$$

where Ψ assumes different forms according to the specific improved model that is adopted. In particular, one has:

$$\text{Wang and Wen (1998): } \Psi = \begin{cases} \gamma + \beta \operatorname{sgn}(\dot{x} z) \\ + \phi \operatorname{sgn}(\dot{x} + \dot{z}) \end{cases} \quad (4.7)$$

$$\text{Song and Der Kiureghian (2006): } \Psi = \begin{cases} \beta_1 \operatorname{sgn}(\dot{x} z) + \beta_2 \operatorname{sgn}(x \dot{x}) \\ + \beta_3 \operatorname{sgn}(x z) + \beta_4 \operatorname{sgn}(\dot{x}) \\ + \beta_5 \operatorname{sgn}(z) + \beta_6 \operatorname{sgn}(x) \end{cases} \quad (4.8)$$

$$\text{Sireteanu et al. (2012): } \Psi = \begin{cases} \beta_1 \operatorname{sgn}(\dot{x} z) + \beta_2 \operatorname{sgn}(x \dot{x}) \\ - \beta_2 \operatorname{sgn}(x z) + \beta_4 \operatorname{sgn}(\dot{x}) \\ + \beta_5 \operatorname{sgn}(z) \end{cases} \quad (4.9)$$

where β_1, \dots, β_6 and ϕ are material parameters.

Equation (4.7), introduced by Wang and Wen, includes an additional parameter ϕ that takes into account the asymmetric behaviour; being independent from the sign of the generalised displacement x , Equation (4.7) cannot describe the asymmetric hysteresis due to cyclic phenomena since, during them, the sign of the generalised displacement x changes.

For this reason, Song and Der Kiureghian have developed Equation (4.8); basically, the function Ψ defined by this equation can assume different values in six phases depending on the signs of x , \dot{x} , and z and on the values of six fixed parameters, namely β_1, \dots, β_6 . Consequently, this model has six degrees of freedom that affect the complexity of the parameter identification.

Subsequently, Sireteanu et al. have modified the Song and Der Kiureghian model by imposing the following conditions:

$$\beta_3 = -\beta_2 \quad \text{and} \quad \beta_6 = 0, \quad (4.10)$$

that represent a continuity condition of the hysteresis loop at the points of intersections with the axis of ordinates. Equation (4.9) describes four different behaviours depending on the signs of x , \dot{x} , and z and on the values of only four fixed parameters, namely β_1 , β_2 , β_4 , and β_5 .

Figure 4.4 shows the four different curves of the Ψ function defined by Sireteanu et al. The continuity condition in Equation (4.10) involves that the hysteretic loop is characterised by the conditions:

$$\Psi_3 = \Psi_4 \quad \text{and} \quad \Psi_6 = \Psi_1.$$

Table 4.1 lists the sign combinations of x , \dot{x} , and z for the different curves showed in Figure 4.4.

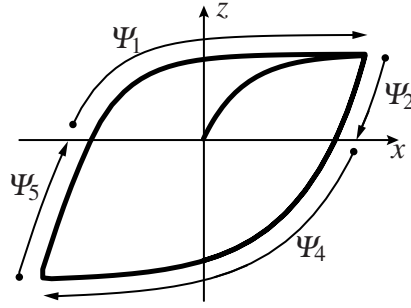


Figure 4.4: Values of the Ψ function in the model by Sireteanu et al.

4.1.2.2 Sensitivity analysis

A parameter sensitivity analysis was carried out to evaluate the effect of each parameter of the Ψ function on the hysteretic variable $z(x)$ evaluated by adopting Equation (4.1), Equation (4.6), and Equation (4.9).

Figure 4.5 shows the relationship between the hysteretic variable z and the generalised displacement x . All hysteretic loops have been obtained by applying a generalised displacement described by the sine wave in Equation (4.5).

The Figure 4.5a shows the influence of the first value of the Ψ function, namely Ψ_1 , on the hysteretic loop. Such a value modifies the shape of the hysteretic loop in the first and second quadrant when $\dot{x} > 0$ and $z > 0$: the hysteretic variable z is prone to decrease with an increasing value of Ψ_1 ; the hysteretic loop exhibits work hardening (softening) when the Ψ_1 value is negative (positive).

The influence of the Ψ_2 value on the hysteretic loop is shown in Figure 4.5b. The value Ψ_2 modifies the trend of the hysteretic loop in the second quadrant when $x > 0$, $\dot{x} < 0$, and $z > 0$: the hysteretic variable z is prone to decrease with an increasing value of Ψ_2 ; the hysteretic loop is concave (convex) when the Ψ_2 value is negative (positive).

The Ψ_4 value modifies the shape of the hysteretic loop in the third and fourth quadrant when $\dot{x} < 0$ and $z < 0$; the influence of such

Phase	x	\dot{x}	z	$\psi(x, \dot{x}, z)$
1	[-]	+	+	$\psi_1 = \beta_1 + \beta_4 + \beta_5$
2	+	-	+	$\psi_2 = -\beta_1 - 2\beta_2 - \beta_4 + \beta_5$
3	[-]	-	-	$\psi_4 = \beta_1 - \beta_4 - \beta_5$
4	-	+	-	$\psi_5 = -\beta_1 - 2\beta_2 + \beta_4 - \beta_5$

Table 4.1: Sign combinations of the Ψ function in the model by Sireteanu et al.

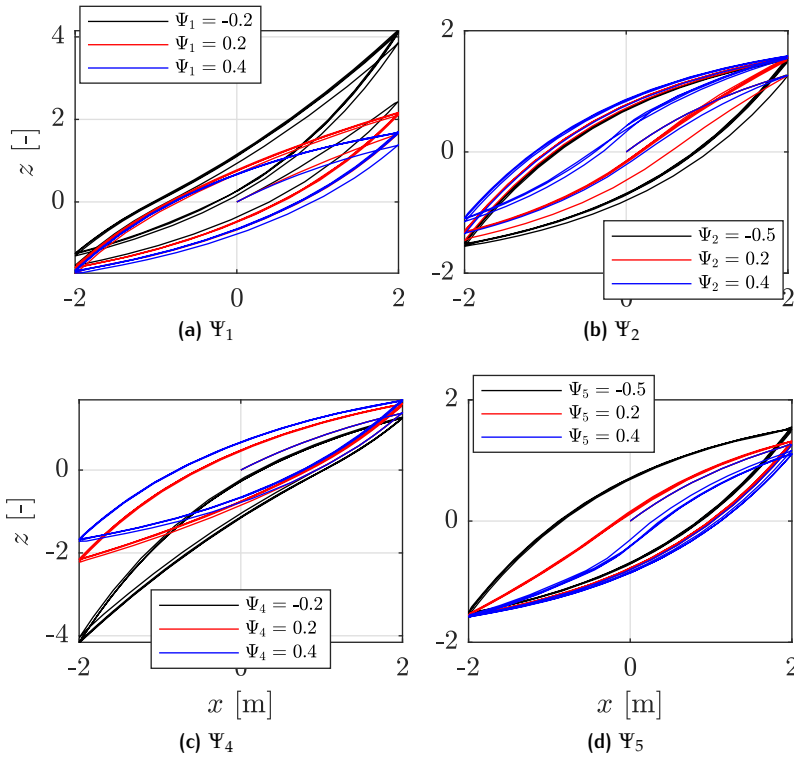


Figure 4.5: Sensitivity analysis of the Bouc-Wen model with respect to the material parameters.

a value is shown in Figure 4.5c: the hysteretic variable z is prone to increase with an increasing value of Ψ_4 ; the hysteretic loop shows work hardening (softening) when the Ψ_4 value is negative (positive).

Finally, Figure 4.5d shows the influence of the Ψ_5 value on the hysteretic loop. This value modifies the shape of the hysteretic loop in the third quadrant when $x < 0$, $\dot{x} > 0$, and $z < 0$: the hysteretic function z is prone to increase with an increasing value of Ψ_5 ; namely, the hysteretic loop is concave (convex) when the Ψ_5 value is positive (negative).

4.1.3 Modelling of pinched hysteresis loops

The pinching effect is a physical phenomenon, observed in many experimental results, in which a very low incremental stiffness near the origin followed by a stiffening under greater generalised displacements. In particular we can observe the pinching effect in reinforced concrete structures due to the high shear loads, the slippage of longitudinal reinforcement [13], the opening and closing of cracks in the compress-

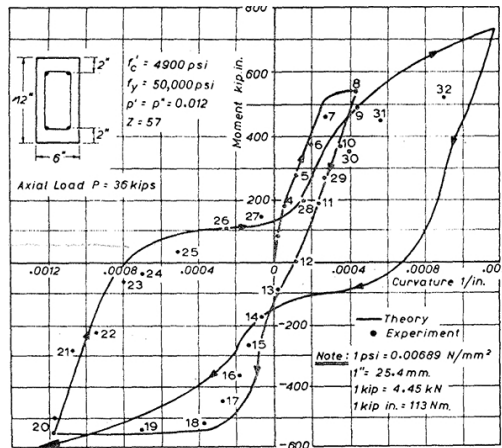


Figure 4.6: The hysteresis behaviour of a concrete column section - R. Park et al. [93].

sion zones [93], Y-braced steel frames and confined walls of masonry structures. A hysteresis loop with the pinching effect, obtained in experimental tests, is shown in Figure 4.6.

4.1.3.1 Pinching Bouc-Wen models

To account for the above-described pinching effects, some researchers [8, 9, 46, 120] have modified the expression of the function employed by the symmetric differential models, described in Section 4.1.1, to evaluate the hysteretic variable z . In particular, some modified expressions of such a function are

$$\text{Baber and Noori (1985)} = \begin{cases} B = \frac{B_h B_p}{B_h + B_p} \\ B_h = A - |z^n| (\gamma + \beta \operatorname{sgn}(\dot{x}z)) \\ B_p = \left(\frac{1}{\sqrt{2\pi} Z_\sigma} \Delta x \exp\left(-\frac{z^2}{2Z_\sigma^2}\right) \right) \end{cases} \quad (4.11)$$

$$\text{Baber and Noori (1986)} = \begin{cases} B = h \left(A - |z^n| (\gamma + \beta \operatorname{sgn}(\dot{x}z)) \right) \\ h = 1 - \zeta_1 \exp\left(-\frac{z^2}{2\zeta_2^2}\right) \end{cases} \quad (4.12)$$

$$\text{Foliente (1995)} = \begin{cases} B = h \left(A - |z^n| \left(\gamma + \beta \operatorname{sgn}(\dot{x} z) \right) \right) \\ h = 1 - \zeta_1 \exp \left(- \frac{(z - \bar{z} \operatorname{sgn}(\dot{x}))^2}{\zeta_2^2} \right) \end{cases} \quad (4.13)$$

$$\text{Sivaselvan et al. (2000)} = \begin{cases} B = \frac{B_h B_p}{B_h + B_p} \\ B_h = A - \left| \frac{z}{z_y} \right|^n \left(\gamma + \beta \operatorname{sgn}(\dot{x} z) \right) \\ B_p = \left(\frac{1}{\sqrt{2} \pi Z_\sigma} \Delta x \exp \left(- \frac{(z - \bar{z} \operatorname{sgn}(\dot{x}))^2}{2 Z_\sigma^2} \right) \right)^{-1} \\ \Delta x = R_s (x_{\max}^+ - x_{\max}^-) \\ Z_\sigma = \sigma z_y \\ \bar{z} = \lambda z_y \end{cases} \quad (4.14)$$

where B_h , B_p , γ , β , etc. are material parameters.

Baber and Noori (1985) take into account the pinching effect in their model through a pinching spring with stiffness B_p in series with the hysteretic element associated with z , see Equation (4.11). The parameter Δx represents the length at which the variable z of the pinching spring tends to $+\infty$ ($-\infty$), namely:

$$\lim_{x \rightarrow +\Delta x^-} z(x) = +\infty, \quad \lim_{x \rightarrow -\Delta x^+} z(x) = -\infty,$$

and is associated with the energy dissipation ε . Z_σ is related to the sharpness of pinching; in particular a higher Z_σ implies a more uniform pinching effect.

In 1986, Baber and Noori proposed a different strategy to account for the pinching effect (see Equation (4.12)); in particular it amount to multiplying the A parameter by a pinching function h that depends on the energy dissipation ε , the hysteretic function z , and two parameters, namely ζ_1 and ζ_2 : the first one controls the severity of pinching, whereas the second controls the spread of the pinching region.

Foliente followed the same strategy proposed by Baber and Noori (1986) but proposed a pinching function h that depends on ε , z , ζ_1 and ζ_2 , as well as the pinching function h in Equation (4.12); in addition, the function h also depends on the parameter \bar{z} that corresponds to a fraction of z at $dz/dx = 0$.

Finally, Sivaselvan and Reinhorn proposed a model similar to the one by Baber and Noori (1985), the main difference lying in the fact that in the former model the pinching parameter Δx depends on the maximum generalised displacement reached on the positive and negative sides during the response, weighed through the parameter of the model R_s ,

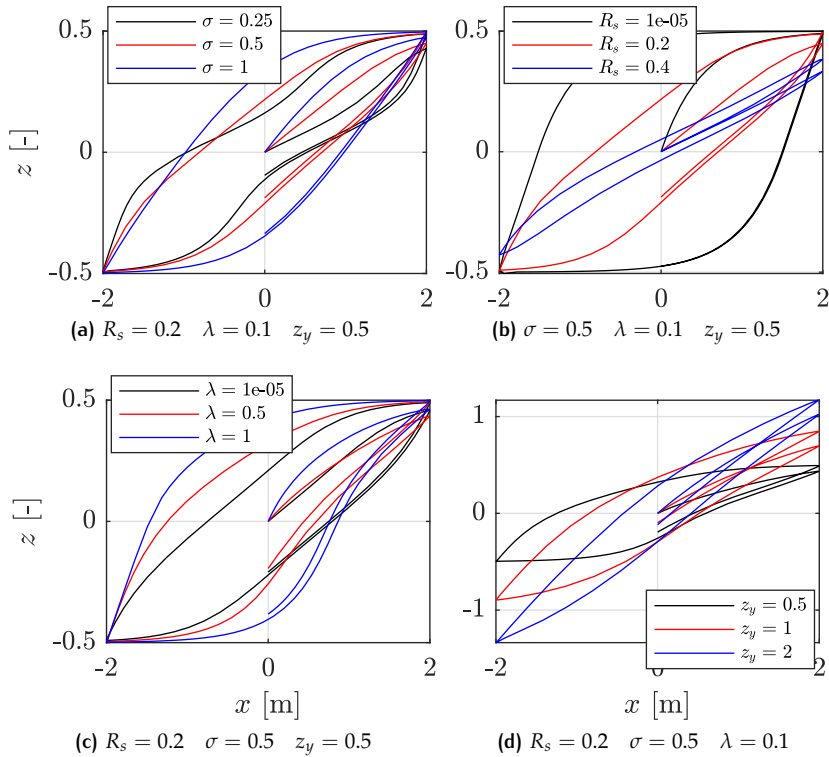


Figure 4.7: Sensitivity analysis of the Bouc-Wen model with respect to the material parameters.

and no longer on the energy dissipation ε . Z_σ and \bar{z} are two variables that depend on the yield value of the hysteretic variable, i.e. z_y through two parameters of the model, namely σ and λ (see Equation (4.14)).

4.1.3.2 Sensitivity analysis

A sensitivity analysis was carried out to evaluate the effect of each parameter on the hysteretic variable $z(t)$ evaluated by adopting Equation (4.1), and Equation (4.14). The effects of the parameters R_s , σ , λ , and z_y on the hysteretic function z are shown in Figure 4.7. All hysteretic loops have been obtained by applying a generalised displacement described by the sine wave in Equation (4.5).

Figure 4.7a shows the variation of the σ parameter: this parameter controls the pinching region and increasing σ causes the pinching region to spread. Figure 4.7b shows the variation of the R_s parameter: the intensity of the pinching effect is prone to decrease with a decreasing R_s ; specifically, when R_s approaches 0 the pinching effect is null. Figure 4.7c depicts the variations of the λ parameter: the hysteresis

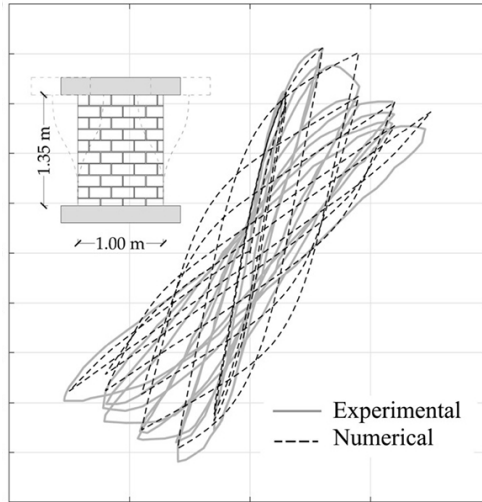


Figure 4.8: The hysteresis behaviour of a unreinforced masonry panels - D. Liberatore et al. [74].

loop tends to become more asymmetric when λ increases. Finally, Figure 4.7d shows the variation of the z_y parameter: the tangent stiffness at the origin of the hysteresis loop increases with an increasing value of z_y .

4.1.4 Modelling of degrading hysteresis loops

It is well known from the scientific literature that many mechanical systems can exhibit strength and stiffness degradation. In general we can see a hysteretic degrading behaviour when the systems are subjected to cyclic loads like earthquake, winds and so on. For instance, in concrete and masonry [74] structures it is possible to observe a progressive loss of stiffness due to the opening and closing of cracks when the applied loads change direction. Wooden structures also exhibit hysteretic degrading behaviour. In Figure 4.8 hysteresis loop exhibiting strength and stiffness degradation is shown.

4.1.4.1 Degrading Bouc-Wen models

Similarly to the asymmetric and pinched hysteresis phenomena, several researchers [8, 10, 46] have modified the differential models described in Section 4.1.1 to allow for the simulation of the stiffness and strength degradation effects. Specifically, they have modified the expression

employed for evaluating the hysteresis function, required to compute the model output, as follows:

$$\text{Baber and Wen (1981)} = \begin{cases} B = \frac{A}{\eta} - \nu |z^n| (\gamma + \beta \operatorname{sgn}(\dot{x}z)) \\ A = A[\varepsilon(t)] = A_0 - \delta_A \varepsilon(t) \\ \eta = \eta[\varepsilon(t)] = \eta_0 + \delta_\eta \varepsilon(t) \\ \nu = \nu[\varepsilon(t)] = \nu_0 + \delta_\nu \varepsilon(t) \end{cases} \quad (4.15)$$

$$\text{Baber and Noori (1985)} = \begin{cases} B = \frac{A}{\eta} - \nu |z^n| (\gamma + \beta \operatorname{sgn}(\dot{x}z)) \\ A = A[\varepsilon(t)] = A_0 - \delta_A \varepsilon(t) \\ \eta = \eta[\varepsilon(t)] = 1 + \delta_\eta \varepsilon(t) \\ \nu = \nu[\varepsilon(t)] = 1 + \delta_\nu \varepsilon(t) \end{cases} \quad (4.16)$$

$$\text{Foliente (1995)} = \begin{cases} B = \frac{A}{\eta} - \nu |z^n| (\gamma + \beta \operatorname{sgn}(\dot{x}z)) \\ \eta = \eta[\varepsilon(t)] = 1 + \delta_\eta \varepsilon(t) \\ \nu = \nu[\varepsilon(t)] = 1 + \delta_\nu \varepsilon(t) \end{cases} \quad (4.17)$$

where A , η , ν , etc. are material parameters.

All models consider strength, stiffness, or combined degradation, from the initial time $t = 0$ to the present one, as a function of the dissipated energy associated with the hysteretic displacement z ; its expression is given by

$$\varepsilon(t) = \int_0^t z \dot{x} dt \quad (4.18)$$

In particular, a convenient measure of degradation is the cumulative hysteretic dissipated energy $\varepsilon(t)$ since degradation depends on the intensity and duration of the phenomenon under investigation

Baber and Wen defined two new parameters: η and ν controlling in turn the stiffness and the strength degradation. Moreover, the amplitude of the hysteresis loop, controlled by the A parameter, can change. In the Baber and Noori (1985) model the η_0 and ν_0 parameters, which represent the initial values of the degradation functions, are set to 1. Finally, in the Foliente model the degradation law related to the A parameter is null. All models assume that both parameters η and ν depend linearly on the hysteretic energy $\varepsilon(t)$.

It is worth being emphasised that the energy dissipated by the material coincides with $\varepsilon(t)$ in Equation (4.18) only for peculiar values of the parameters. In general, $\varepsilon(t)$ does not necessarily fulfil the thermodynamic compatibility. For this reason, the use of degrading Bouc-Wen formulations should carefully account for such an issue.

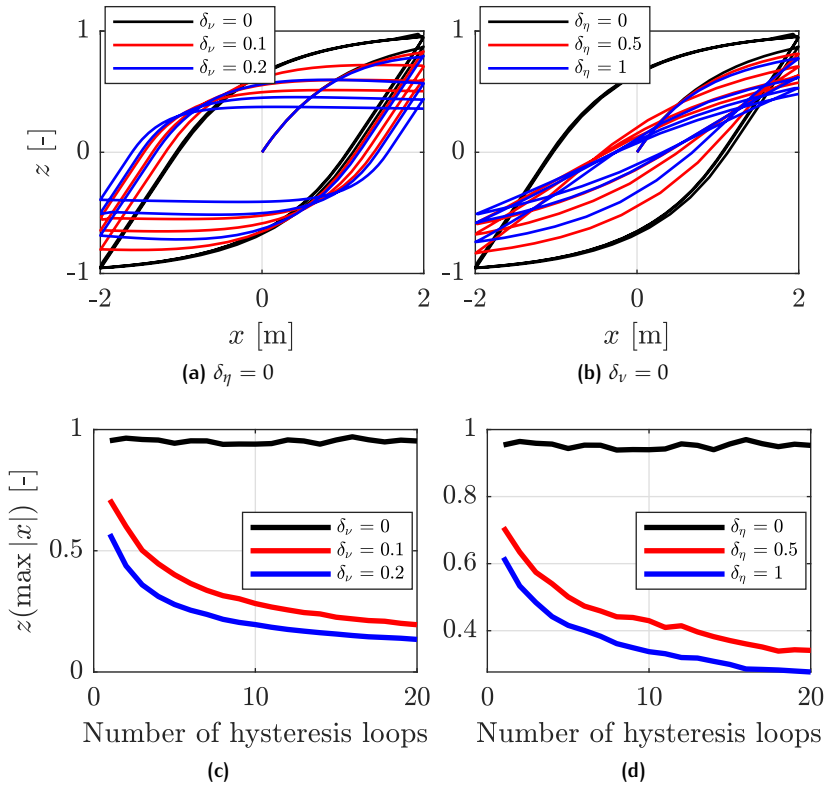


Figure 4.9: Sensitivity analysis of the Bouc-Wen model with respect to the material parameters.

4.1.4.2 Sensitivity analysis

Sensitivity analysis has been carried out on the Foliente model [46] and the results are shown in Figure 4.9. The top left and the top right plots show the hysteresis loops that exhibit a strength and stiffness degradation, respectively. For both top plots, there are two black coloured hysteresis loops without any kind of degradation, obtained by setting to zero the values of δ_η and δ_v . Conversely, when the latter parameters are greater than zero, a degrading hysteretic behaviour is obtained; in particular the rate of the strength and stiffness degradation gets stronger when the δ_η and δ_v parameters, respectively, increase. All hysteretic loops have been obtained by applying a generalised displacement described by the sine wave in Equation (4.5).

The two bottom plots show the relationship between the number of hysteresis loops and the value of the hysteretic function z associated with the maximum positive displacement x . In these plots the effect of δ_η and δ_v parameters on the hysteresis behaviour are more evident.

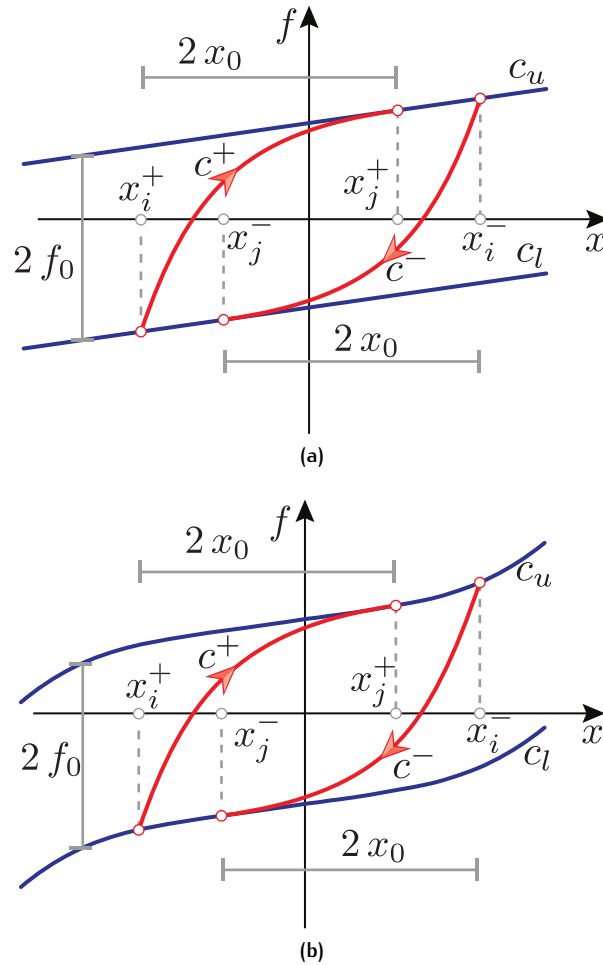


Figure 4.10: Hysteresis loop bounded by two straight parallel lines (a) or curves (b).

4.2 PROPOSED CLASS OF UNIAXIAL PHENOMENOLOGICAL MODELS

The Bouc-Wen model [19, 145] is the most popular hysteretic model and is used to simulate several types of hysteretic phenomena [62, 64]. This model is of differential nature, that is the equation that allows one to evaluate the output state variable is a nonlinear ordinary differential equation. Unfortunately, this differential equation could need some iterative techniques for each time step of the nonlinear time history analysis by increasing the computational costs. To overcome the limits of the differential models, we use a computationally efficient model

belonging to a class developed by Vaiana *et al.* [133]. This model is of algebraic nature so that it is possible to evaluate the output variable in closed form. Consequently, the computation time for geometrically and mechanically-nonlinear dynamics analyses can be reduced. Moreover, this model can be used in a design procedure using an energy-based approach (described in Section 4.3), since it is possible to evaluate the dissipated energy analytically.

4.2.1 Assumptions of the class of hysteretic models

First of all, the class of hysteretic models is able to reproduce a symmetric loop bounded between two parallel straight lines (Figure 4.10a) or curves (Figure 4.10b). Additionally, it assumes that the general loop is defined by four separate curves:

- the upper and the lower limiting curves, denoted as c_u and c_l , respectively, and represented by the blue colour in the Figure 4.10;
- the loading and unloading limiting curves, denoted as c^+ and c^- , respectively, and represented in red in the Figure 4.10.

As shown in Figure 4.10, the model assumes that the distance between the upper and the lower limiting curves is constant and equal to $2f_0$, in which f_0 [$-f_0$] represents the point of intersection between the upper [lower] limiting curve with the axis of ordinate. This assumption implies that the distance between the starting and the ending point on the upper [lower] limiting curves c_u [c_l], denoted as x_i and x_j , respectively, is assumed to be constant and equal to $2x_0$ (see Figure 4.10). Accordingly, utilising the superscript $+$ [$-$] to denote the generic loading [unloading] curve, one obtains $x_i^+ = x_j^+ - 2x_0$ [$x_i^- = x_j^- + 2x_0$]. Please, notice that, if the restoring force is equal for positive and negative excitations, the displacements x_j^+ [x_i^+] and x_j^- [x_i^-] can be the same in absolute value.

Consequently, in the generic loading case, that is to say when the horizontal velocity is positive ($\dot{x} > 0$), the generalised force f is computed as

$$f(x, x_j^+) = \begin{cases} c^+(x, x_j^+) & \text{if } x \in [x_j^+ - 2x_0, x_j^+], \\ c_u(x) & \text{if } x \in [x_j^+, \infty). \end{cases}$$

Conversely, for a generic unloading case ($\dot{x} < 0$), the generalised force f can be computed in the following way

$$f(x, x_j^-) = \begin{cases} c^-(x, x_j^-) & \text{if } x \in [x_j^-, x_j^- + 2x_0], \\ c_l(x) & \text{if } x \in (-\infty, x_j^-]. \end{cases}$$

4.2.2 General expressions of the four curves

A uniaxial hysteretic spring parallel to a nonlinear elastic one is used to model the hysteretic behaviour. Such modelling is generally used in scientific literature. Consequently, the general form of the tangent stiffness k_t is computed in the following way

$$k_t(x, x_j^+) = k_e(x) + k_h(x, x_j^+) \quad \text{if } \dot{x} > 0 \quad (4.19)\text{a}$$

$$k_t(x, x_j^-) = k_e(x) + k_h(x, x_j^-) \quad \text{if } \dot{x} < 0 \quad (4.19)\text{b}$$

where $k_h(x, x_j)$ and $k_e(x)$ are the tangent stiffnesses of the hysteretic spring and the nonlinear elastic one. Hysteresis loops bounded between two parallel straight lines can be reproduced by the former spring with tangent stiffness k_h . The latter, having tangent stiffness k_e , modifies the two parallel straight lines in two parallel curves. We suppose that the tangent stiffness $k_h(x, x_j)$ is a nonlinearly decreasing function, from k_a to k_b on $[x_j^+ - 2x_0, x_j^+]$ when $\dot{x} > 0$, or on $[x_j^-, x_j^- + 2x_0]$ when $\dot{x} < 0$, remains constant and equal to k_b on $[x_j^+, \infty)$ when $\dot{x} > 0$, or on $(-\infty, x_j^-]$ if $\dot{x} < 0$.

The generic expressions of the upper and lower limiting curves are obtained by integrating the Equation (4.19), that is

$$c_u(x) = f_e(x) + k_b x + C_u \quad \text{for } x > x_j^+ \quad (4.20)\text{a}$$

$$c_l(x) = f_e(x) + k_b x + C_l \quad \text{for } x < x_j^- \quad (4.20)\text{b}$$

where $f_e(x) = \int k_e(x) dx$. The integral $\int k_h(x, x_j^+) dx$ [$\int k_h(x, x_j^-) dx$] is constant for $x > x_j^+$ [$x < x_j^-$] and equal to $k_b x$. The two integration constants C_u and C_l can be computed by imposing that the curves c_u and c_l intersect the ordinate axis at $f = f_0$ and $f = -f_0$, respectively, and supposing that $f_e(0) = 0$. Consequently, Equation (4.20) can be rewritten in the following way

$$c_u(x) = f_e(x) + k_b x + f_0 \quad (4.21)\text{a}$$

$$c_l(x) = f_e(x) + k_b x - f_0 \quad (4.21)\text{b}$$

By integrating the Equation (4.19) for $x_j^+ - 2x_0 < x < x_j^+$ [$x_j^- < x < x_j^- + 2x_0$], one can obtain the general expression of the loading [unloading] curve

$$c^+(x, x_j^+) = f_e(x) + f_h(x, x_j^+) + C^+ \quad \text{for } x_j^+ - 2x_0 < x < x_j^+ \quad (4.22)\text{a}$$

$$c^-(x, x_j^-) = f_e(x) + f_h(x, x_j^-) + C^- \quad \text{for } x_j^- < x < x_j^- + 2x_0 \quad (4.22)\text{b}$$

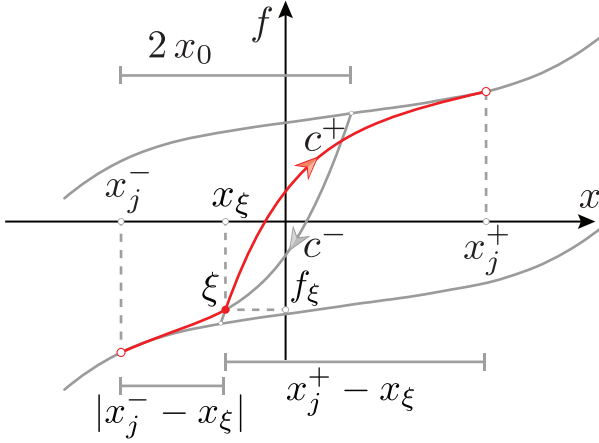


Figure 4.11: Evaluation of the history variable x_j^+ (x_j^-) for a generic loading (unloading) case.

where $f_h(x, x_j^+) = \int k_h(x, x_j^+) dx$ and $f_h(x, x_j^-) = \int k_h(x, x_j^-) dx$. The two integration constants C^+ and C^- can be computed by imposing that the curves c^+ and c^- intersect the upper and the lower limiting curve at $x = x_j^+$ and $x = x_j^-$, respectively. Consequently, Equation (4.22) can be expressed in the following form

$$c^+(x, x_j^+) = f_e(x) + f_h(x, x_j^+) + k_b x_j^+ + f_0 - f_h(x_j^+, x_j^+) \quad (4.23)a$$

$$c^-(x, x_j^-) = f_e(x) + f_h(x, x_j^-) + k_b x_j^- - f_0 - f_h(x_j^-, x_j^-) \quad (4.23)b$$

The internal model parameters x_0 and f_0 can be computed solving an expression in closed-form or numerically, depending on the complexity of the function k_h . Such an expression is

$$f_h(x_j^+ - 2x_0, x_j^+) + 2k_b x_0 + 2f_0 - f_h(x_j^+, x_j^+) = 0 \quad (4.24)$$

obtained by imposing that $c^+ = c_l$ at $x = x_i^+$. An analogous expression can be obtained imposing that $c^- = c_u$ at $x = x_i^-$.

To evaluate the generalised force, it is necessary to derive the expression of x_j^+ [x_j^-]. Such an expression can be derived from a generic starting point ξ of coordinate (x_ξ, f_ξ) , where $x_j^+ - 2x_0 < x_\xi < x_j^+$ [$x_j^- < x_\xi < x_j^- + 2x_0$]. Notably, the expression of the history variable x_j^+ is obtained by imposing that the generic loading curve c^+ passes through the point ξ , as shown in Figure 4.11

$$f_e(x_\xi) + f_h(x_\xi, x_j^+) + k_b x_j^+ + f_0 - f_h(x_j^+, x_j^+) = f_\xi \quad (4.25)$$

In a similar way, one can obtain the expression of the history variable x_j^- by imposing that the generic unloading curve c^- passes through the point ξ , see [Figure 4.11](#).

$$f_e(x_\xi) + f_h(x_\xi, x_j^-) + k_b x_j^- - f_0 - f_h(x_j^-, x_j^+) = f_\xi \quad (4.26)$$

In conclusion, the history variables can be obtained by solving [Equation \(4.25\)](#) and [Equation \(4.26\)](#) for the variables x_j^+ and x_j^- . This system of equations can be solved numerically or in closed-form, depending on the complexity of the tangent stiffness k_h .

4.2.3 Bilinear model formulation

The bilinear model, able to reproduce hysteresis loops bounded between two parallel straight lines, is one of the easiest hysteretic models that can be formulated from the proposed class.

We select the following tangent stiffness functions

$$k_e(x) = 0 \quad \text{on } (-\infty, \infty) \quad (4.27a)$$

$$k_h(x, x_j^+) = \begin{cases} k_a & \text{if } x \in [x_j^+ - 2x_0, x_j^+ [\\ k_b & \text{if } x \in]x_j^+, \infty) \end{cases} \quad (4.27b)$$

$$k_h(x, x_j^-) = \begin{cases} k_a & \text{if } x \in]x_j^-, x_j^- + 2x_0] \\ k_b & \text{if } x \in (-\infty, x_j^- [\end{cases} \quad (4.27c)$$

Consequently, the expressions of the upper and lower limiting curves, obtained by using [Equation \(4.21\)](#), are

$$c_u = k_b x + f_0 \quad (4.28a)$$

$$c_l = k_b x - f_0 \quad (4.28b)$$

Similarly, [Equation \(4.23\)](#) yields the expressions of the loading and unloading limiting curves, i.e.

$$c^+ = k_a (x - x_j^+) + k_b x_j^+ + f_0 \quad (4.29a)$$

$$c^- = k_a (x - x_j^-) + k_b x_j^- - f_0 \quad (4.29b)$$

By solving [Equation \(4.24\)](#) for the internal parameters f_0 , one can obtain

$$f_0 = (k_a - k_b) x_0 \quad (4.30)$$

The history variable x_j^+ can be obtained by involving Equation (4.25)

$$x_j^+ = \frac{k_a x_\xi + f_0 - f_\xi}{k_a - k_b} \quad (4.31)$$

Similarly, the history variable x_j^- follows from Equation (4.26), i.e.

$$x_j^- = \frac{k_a x_\xi - f_0 - f_\xi}{k_a - k_b} \quad (4.32)$$

The influence of the constitutive hysteretic parameters k_a , k_b and x_0 on the hysteresis loop shape is shown in [133].

4.2.4 Algebraic model formulation

In this Section, we describe the algebraic hysteretic model able to simulate the behaviour of the LRBs and HDRBs [134]. Such a hysteretic model is also able to reproduce the behaviour of WRIs along the Shear and Roll directions [132].

The tangent stiffness functions of the algebraic model are

$$k_e(x) = 3\beta_1 x^2 + 5\beta_2 x^4 \quad \text{on } (-\infty, \infty) \quad (4.33)\text{a}$$

$$k_h(x, x_j^+) = \begin{cases} k_b + \frac{k_a - k_b}{(1 + x - x_j^+ + 2x_0)^\lambda} & \text{if } x \in [x_j^+ - 2x_0, x_j^+ [\\ k_b & \text{if } x \in]x_j^+, \infty) \end{cases} \quad (4.33)\text{b}$$

$$k_h(x, x_j^-) = \begin{cases} k_b + \frac{k_a - k_b}{(1 - x - x_j^- + 2x_0)^\lambda} & \text{if } x \in]x_j^-, x_j^- + 2x_0] \\ k_b & \text{if } x \in (-\infty, x_j^- [\end{cases} \quad (4.33)\text{c}$$

where x represents the longitudinal displacement and k_a , k_b , λ , β_1 , and β_2 are the model parameters. Notably, k_a is the tangent stiffness of curve c^+ [c^-] at $x = x_i^+$ [$x = x_i^-$], k_b is the tangent stiffness of curve c^+ [c^-] at $x = x_j^+$ [$x = x_j^-$], and the dimensionless parameter λ defines the rate of change of the tangent stiffness from k_a to k_b for both curves c^+ and c^- . Finally, the parameters β_1 and β_2 define the curvatures of the upper and lower limiting curves.

Consequently, the expressions of the upper (lower) and the loading (unloading) limiting curves can be computed by integrating Equation (4.33) to get

$$c_u = \beta_1 x^3 + \beta_2 x^5 + k_b x + f_0, \quad (4.34)\text{a}$$

$$c_l = \beta_1 x^3 + \beta_2 x^5 + k_b x - f_0, \quad (4.34)\text{b}$$

and

$$\begin{aligned} c^+ &= \beta_1 x^3 + \beta_2 x^5 + k_b x + f_0 \\ &+ (k_a - k_b) \left(\frac{(1 + x - x_j^+ + 2x_0)^{(1-\lambda)}}{1 - \lambda} - \frac{(1 + 2x_0)^{(1-\lambda)}}{1 - \lambda} \right), \end{aligned} \quad (4.35)\text{a}$$

$$\begin{aligned} c^- &= \beta_1 x^3 + \beta_2 x^5 + k_b x - f_0 \\ &+ (k_a - k_b) \left(\frac{(1 - x + x_j^- + 2x_0)^{(1-\lambda)}}{\lambda - 1} - \frac{(1 + 2x_0)^{(1-\lambda)}}{\lambda - 1} \right), \end{aligned} \quad (4.35)\text{b}$$

From a mathematical point of view, $k_a > k_b$, $k_a > 0$, $\lambda > 0$, $\lambda \neq 1$, $x_0 > 0$, and $\beta_1, \beta_2 \in \mathbb{R}$. The influence of these parameters on the hysteresis loop shape is shown in [134].

The internal model parameters x_0 and f_0 can be evaluated as follows

$$x_0 = \frac{1}{2} \left[\left(\frac{k_a - k_b}{\delta_k} \right)^{\frac{1}{\lambda}} - 1 \right], \quad (4.36)$$

$$f_0 = \frac{k_a - k_b}{2} \left(\frac{(1 + 2x_0)^{(1-\lambda)} - 1}{1 - \lambda} \right), \quad (4.37)$$

in which δ_k is the difference between the two values assumed by the tangent stiffness at x_j^+ [x_j^-] and it may be set equal to 10^{-20} , as explained in [134].

Similarly, as shown in the previous Section, the history variable x_j^+ can be computed using Equation (4.25), i.e.

$$\begin{aligned} x_j^+ &= 1 + x_\xi + 2x_0 - \left\{ \frac{1 - \lambda}{k_a - k_b} \left[f_\xi - \beta_1 x_\xi^3 - \beta_2 x_\xi^5 - k_b x_\xi \right. \right. \\ &\quad \left. \left. - f_0 + (k_a - k_b) \frac{(1 + 2x_0)^{(1-\lambda)}}{1 - \lambda} \right] \right\}^{\left(\frac{1}{1-\lambda} \right)} \end{aligned} \quad (4.38)$$

On the other hand, the history variable x_j^- can be obtained in the following way

$$\begin{aligned} x_j^- &= -1 + x_\xi - 2x_0 + \left\{ \frac{\lambda - 1}{k_a - k_b} \left[f_\xi - \beta_1 x_\xi^3 - \beta_2 x_\xi^5 - k_b x_\xi \right. \right. \\ &\quad \left. \left. + f_0 + (k_a - k_b) \frac{(1 + 2x_0)^{(1-\lambda)}}{\lambda - 1} \right] \right\}^{\left(\frac{1}{1-\lambda} \right)} \end{aligned} \quad (4.39)$$

that trivially follows from Equation (4.26).

4.3 THE ENERGY-BASED DESIGN PROCESS FOR THE DEFINITION OF THE HYSTERETIC MODEL PARAMETERS

The constitutive models' parameters, namely k_a, k_b, x_0 for the bilinear model, and $k_a, k_b, \lambda, \beta_1, \beta_2$ for the algebraic one, can be calibrated from experimental testing by an inverse identification strategy as shown in [113]. However, this approach could be a hard task for the designer since the experimental data of elastomeric isolators and WRIs are not available on the manufacturers' catalogues. Hence, the choice of the mechanical characteristics of the above-mentioned isolators, and consequently the isolator's type and size, could require some iterations in the design process.

This Section provides a design procedure able to predict the parameters of bilinear and algebraic hysteretic models described in Section 4.2, that are strictly related to mechanical characteristics of isolators. This procedure is based on equating the area of the hysteresis loop with the shape of an ellipse, which represents the energy dissipated through the equivalent linear rate-dependent hysteretic model, and the area of the hysteresis loop displayed by the generic isolator. In this way, the hysteretic model parameters can be evaluated from data easily available to the designer, namely the isolated system's mass and period, the admissible displacement of the elastomeric device and the viscous damping factor.

4.3.1 Evaluation of the energy dissipated per cycle

The force-displacement relationship is an ellipse when the damping is strictly viscous. The area of the ellipse represents the energy dissipated and it is computed as follows

$$E_v = 2 \pi k_{\text{eff}} x_{\text{max}}^2 \zeta, \quad (4.40)$$

where k_{eff} is the effective secant stiffness of the peak-to-peak values in the hysteresis loop, x_{max} is the maximum displacement, and ζ is the viscous damping factor.

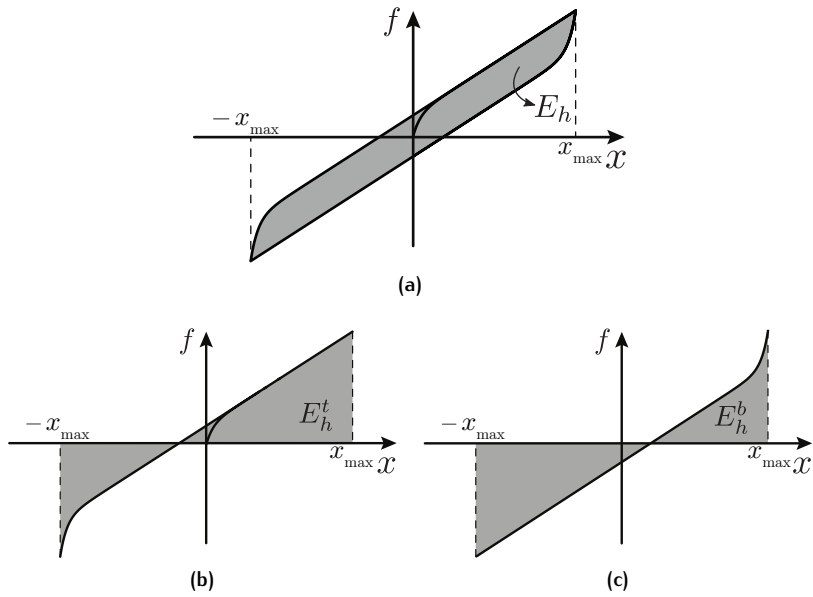


Figure 4.12: The full area (a), the area below the top (b) and the bottom (c) curve of the algebraic hysteretic model.

4.3.1.1 Energy dissipated by the bilinear model

The energy dissipated by the hysteresis loop in one cycle, simulated through the bilinear model, can be trivially computed in closed form by the following formula

$$E_a = 4 f_0 (x_{\max} - x_0). \quad (4.41)$$

4.3.1.2 Energy dissipated by the algebraic model

The energy dissipated by the hysteresis loop in one cycle, simulated through the algebraic model, can be evaluated in closed form, owing to the fact that each curve of the hysteresis loop is defined by analytical expressions. Indeed, the energy dissipated on the interval $[-x_{\max}, x_{\max}]$ is the difference between the area below the top and the bottom curve of the loop, see e.g. [Figure 4.12](#), by giving:

$$E_h = E_h^t - E_h^b = \left(\int_{-x_{\max}}^{-x_{\max}+2x_0} c^+ dx + \int_{-x_{\max}+2x_0}^{x_{\max}} c_u dx \right) - \left(\int_{-x_{\max}}^{x_{\max}-2x_0} c_l dx + \int_{x_{\max}-2x_0}^{x_{\max}} c^- dx \right), \quad (4.42)$$

so that replacing Equation (4.34) and Equation (4.35) in the previous equation, one obtains

$$E_h = \frac{(1 + 2x_0)^{-\lambda}}{(\lambda - 2)(\lambda - 1)} \left[2(k_a - k_b)(1 + 2x_0)(1 + 2x_0(\lambda - 1)) - 2(1 + 2x_0)^\lambda (k_a - k_b - 2f_0 x_{\max}(\lambda - 2)(\lambda - 1)) \right]. \quad (4.43)$$

We infer from Equation (4.43), that the dissipated energy E_h does not depend on the model parameters β_1 and β_2 . In fact, the hysteresis loop is symmetric, i.e. it is characterised by an odd function with respect to the origin of the reference frame; consequently, the variation of curvature of the limiting curves c_u and c_l does not affect the area of the hysteresis loop.

The initial tangent stiffness k_a can be expressed as a multiple of the post yield tangent stiffness k_b

$$k_a = \eta k_b, \quad (4.44)$$

where η is the initial-to-post yield tangent stiffness ratio [90, 121]. For instance, [90] recommended $\eta \approx 3 \div 6$ for the HDBRs and $\eta \approx 10 \div 21$ for the LRBs.

Replacing Equation (4.36), Equation (4.37) and Equation (4.44) in Equation (4.43), we get

$$E_h = \frac{2}{(\lambda - 2)(\lambda - 1)} \left\{ k_b(\eta - 1)(x_{\max}(\lambda - 2) - 1) + \lambda \left(\frac{k_b(\eta - 1)}{\lambda} \right)^{\frac{1}{\lambda}} \left[(\lambda - 1) \left(\frac{k_b(\eta - 1)}{\lambda} \right)^{\frac{1}{\lambda}} - (\lambda - 2)(x_{\max} + 1) \right] \right\}. \quad (4.45)$$

4.3.2 Evaluation of the bilinear model parameters

Exploiting Equation (4.44), the bilinear model's constitutive parameters to evaluate are only k_a and x_0 . These parameters can be computed by equating the energy dissipated by the bilinear hysteresis loop E_a and the equivalent viscous one E_v , obtaining the following system of equations

$$f_0 = \frac{E_v}{4(x_{\max} - x_0)} \quad (4.46a)$$

$$k_b = k_{\text{eff}} - \frac{f_0}{x_{\max}} \quad (4.46b)$$

$$k_a = \eta k_b \quad (4.46)c$$

$$x_0 = \frac{f_0}{k_a - k_b} \quad (4.46)d$$

i.e. a nonlinear system of equations given the dependence of f_0 on the unknowns k_a and x_0 .

The effective secant stiffness k_{eff} in Equation (4.40) can be evaluated from the properties of the seismically base-isolated rigid body, i.e.

$$k_{\text{eff}} = \left(\frac{2\pi}{T_{bi}} \right)^2 (m + m_b), \quad (4.47)$$

in which T_{bi} and $m + m_b$ are the isolation period and the total mass, respectively.

Such a system (4.46) can be solved in a closed form to get

$$f_0 = \frac{x_{\text{max}} k_{\text{eff}}}{4\eta} (\eta - 1) \left(2 + \pi \zeta \mp \frac{\Delta}{\sqrt{\eta - 1}} \right) \quad (4.48)a$$

$$k_b = \pm \frac{k_{\text{eff}}}{4\eta} \left(2 + 2\eta + \zeta (\pi - \pi\eta) + \Delta \sqrt{\eta - 1} \right) \quad (4.48)b$$

$$k_a = \eta k_b \quad (4.48)c$$

$$x_0 = \frac{x_{\text{max}}}{4} \left(2 - \pi \zeta \mp \frac{\Delta}{\sqrt{\eta - 1}} \right) \quad (4.48)d$$

where

$$\Delta = \sqrt{4(\eta - 1) + \pi \zeta (\pi \zeta (\eta - 1) - 4(\eta + 1))}. \quad (4.49)$$

4.3.3 Evaluation of the algebraic model parameters

The algebraic hysteretic model's area depends on just two parameters, namely k_b and λ , once the initial-to-post yield tangent stiffness ratio η and the admissible displacement of the elastomeric isolator x_{max} have been established. These mechanical characteristics can be estimated by means of a constrained optimisation problem obtained by equating the energy dissipated by the hysteresis loop simulated through the algebraic hysteretic model E_h and the equivalent viscous one E_v .

Let us define the objective function to be optimised ϵ as the relative error between the energy dissipated by the equivalent viscous model and the algebraic hysteretic model

$$\epsilon = \frac{|E_v - E_h|}{|E_v|}. \quad (4.50)$$

The constrained optimisation problem consists of minimising the function ϵ with respect to the variables k_b and λ and in the presence of constraints on those variables. Accordingly, the problem can be expressed in the following form

$$\begin{aligned} \min_{\substack{k_b \in \mathbb{R}^+ \setminus \{0\} \\ \lambda \in \mathbb{R}^+ \setminus \{0,1\}}} \epsilon(k_b, \lambda) \quad \text{subject to: } k_b = k_{\text{eff}} - \frac{f_0}{x_{\text{max}}}, \end{aligned} \quad (4.51)$$

wherein the constraint $k_b = k_{\text{eff}} - f_0/x_{\text{max}}$ is nonlinear given the dependence of f_0 on the unknowns k_b and λ , see [Equation \(4.37\)](#).

The problem in [Equation \(4.51\)](#) has to be solved numerically. In this study, we used the Interior Point technique, see e.g. [143] for a more extensive description.

In order to provide the best estimate of the optimal solution, it is necessary to define the initial points k_b^0 and λ^0 . A general criterion for a correct choice of k_b^0 and λ^0 does not exist. However, the extensive numerical tests that have been carried out by the authors, starting with randomly generated initial points, have proved that the values

$$k_b^0 = k_{\text{eff}} \quad \text{and} \quad \lambda^0 = \frac{\log\left(\frac{k_{\text{eff}}(\eta - 1)}{\delta_k}\right)}{\log(1 + 2x_{\text{max}})} \quad (4.52)$$

provide a good lower local minimum objective function value. The order of magnitude of the relevant value at solution is equal to 10^{-10} .

The expression of λ^0 has been obtained by inverting [Equation \(4.36\)](#) and setting $k_b^0 = k_{\text{eff}}$ and $x_0 = x_{\text{max}}$.

5

COMPUTATIONAL ANALYSIS

This section shows the results of some numerical analyses performed on seismically isolated rigid bodies by means of the two kinds of elastomeric isolators, i.e. LRBs and HDRBs, and WRIs. The strongly nonlinear force-displacement relationship displayed by elastomeric isolators and WRIs is simulated by the algebraic hysteretic model described in [Section 4.2](#). The constitutive model parameters of the hysteretic model able to reproduce the behaviour of the elastomeric isolators is computed by the energy-based design procedure described in [Section 4.3](#). On the other hand, the constitutive model parameters of WRIs are identified in Shear and Roll directions from experimental hysteresis loops using a user-friendly program named *Parameter Identifier* (ParIde) based on the algorithm described by Sessa *et al.* [[113](#)]. This software identifies the parameters of the uniaxial constitutive model by minimising the mean-square error with respect to an experimental target response, see [[112](#)].

The following analyses consider two collapse conditions that could occur, namely overturning of the rigid body when tilt angle reaches ninety degrees $|\theta| = \pi/2$ [[36](#), [63](#)], and the failure of isolation devices when the horizontal displacement reaches the admissible displacement of the isolator $|x| = x_{\max}$.

5.1 OVERTURNING SPECTRA GENERATED BY IMPULSIVE EXCITATION

In this Section, we establish the performance of the two kinds of elastomeric isolators and WRIs in the protection of a rigid body subjected to an impulsive excitation by overturning spectra [[35](#), [138](#), [149](#)]. These spectra are obtained for rigid bodies having the geometrical and dynamical properties presented in [Table 5.1](#), where α , m , and m_b are

Table 5.1: Properties of the rigid body used for generating the overturning spectra.

α [deg]	m [kg]	m_b [kg]	ω_r [rad s ⁻¹]
15	5 000	286.20	var.

detailed in Section 2.3, whereas $\omega_r = \sqrt{m g R / J_O}$ is the fundamental angular rocking frequency of the rigid body.

The system is subjected to an impulsive signal with a shape of a full sine cycle $\ddot{x}_g = A_{\ddot{x}_g} \sin(\omega_{\ddot{x}_g} t)$, where $A_{\ddot{x}_g}$ is the magnitude, supposed to be variable, and $\omega_{\ddot{x}_g}$ is the angular frequency, supposed to be equal to $2\pi/0.5 \text{ rad s}^{-1}$.

5.1.1 Elastomeric isolators

The evaluation of the algebraic model parameters for simulating the elastomeric isolators' hysteresis loops by means of the design procedure defined in Section 4.3, requires the definition of the following properties: the number of the elastomeric isolators, the isolation period, the elastomeric device's admissible displacement, the equivalent viscous damping factor, and the initial-to-post yield stiffness ratio. The selected values of properties for generating the overturning spectra are given in Table 5.2.

The algebraic model parameters for three types of elastomeric isolators, one LRB and two HDRBs, have been obtained by the design procedure and are reported in Table 5.3. Since the parameters β_1 and β_2 cannot be obtained from the design process, we assigned a value that provides stiffening behaviour at a relatively large value of shear strain.

The overturning spectra in Figure 5.1 are shown by reporting on the abscissa the impulse-to-rigid body angular frequency ratio $\omega_{\ddot{x}_g} / \omega_r$, whereas there is the impulse magnitude normalised with the static value of the minimum overturning acceleration $A_{\ddot{x}_g} / (g \tan(\alpha))$ on the ordinate axis. Consequently, the filled contour maps are obtained by varying the impulse magnitude $A_{\ddot{x}_g}$ and the fundamental angular rocking frequency ω_r of the rigid body supported on: (a) no isolation system, (b) LRB, (c) HDRB₁, and (d) HDRB₂ isolation systems.

Colour maps depict the maximum absolute value of the tilt angle $|\theta_{\max}|$, showing:

- the safe area - represented by the dark blue colour - i.e. the area in which the rigid body does not rock;

Table 5.2: Properties of the elastomeric isolators.

n_d [-]	T_{bi} [s]	x_{\max} [m]	ζ [%]		η [-]	
			LRB	HDRB	LRB	HDRB
4	2	0.30	15	15	10	5

- the overturning area - represented by the red colour - namely the area where the rigid body overturns;
- the rocking area - represented by the colours between the dark blue and red colour - i.e. the area in which the rigid body rocks without overturning.

In addition, the spectra also consider the failure condition of the elastomeric isolators, represented by the 45 degree parallel lines hatch pattern, i.e. the area in which the elastomeric isolators fail due to the fact that the maximum horizontal displacement of the system exceeds the device's admissible displacement.

The comparison of the above-mentioned spectra highlights the performance of the elastomeric isolators. In fact, we can see that both kinds of base isolation increase the safe area, increasing as well the static value of the minimum overturning acceleration, in comparison to the spectrum of the non-isolated rigid bodies. However, we can also see that if the value of the impulse-to-rigid body angular frequency ratio $\omega_{\ddot{x}_g}/\omega_r$ is conveniently high, what typically happens for big-size bodies or high frequencies pulses, the collapse condition of the device will reduce the base-isolated rigid body's safe area in comparison to the non-isolated rigid body one.

The comparison between the spectra of the LRB and the HDRBs isolation systems shows significant differences. The safe area of the LRB isolation system's spectrum is wider than the ones related to the two HDRBs isolation system. The increases of the minimum overturning acceleration of the two HDRBs isolation systems' spectra are less than those characterising the LRB isolation system. Furthermore, the rocking area is prone to increase as the ratio $\omega_{\ddot{x}_g}/\omega_r$ increases when the rigid body is isolated by the HDRB₁ as well as HDRB₂ isolation systems.

From Figure 5.1c and Figure 5.1d we can compare the two HDRBs isolation systems. Figure 5.1c refers to an algebraic model in which the parameters β_1 and β_2 are equal to $\beta_1 = 50 \times 10^3 \text{ N m}^{-3}$ and $\beta_2 = 50 \times 10^3 \text{ N m}^{-5}$, whereas in Figure 5.1d the parameters β_1 and β_2 have been doubled, i.e. $\beta_1 = 100 \times 10^3 \text{ N m}^{-3}$ and $\beta_2 = 100 \times 10^3 \text{ N m}^{-5}$. This means that in the latter case, the stiffening behaviour

Table 5.3: The algebraic model parameters obtained by the energy-based design procedure.

	$k_b \text{ [N m}^{-1}\text{]}$	$\lambda \text{ [-]}$	$\beta_1 \text{ [N m}^{-3}\text{]}$	$\beta_2 \text{ [N m}^{-5}\text{]}$
LRB	1.15×10^4	109.37	0	0
HDRB ₁	1.14×10^4	46.70	50×10^3	50×10^3
HDRB ₂	1.14×10^4	46.70	100×10^3	100×10^3

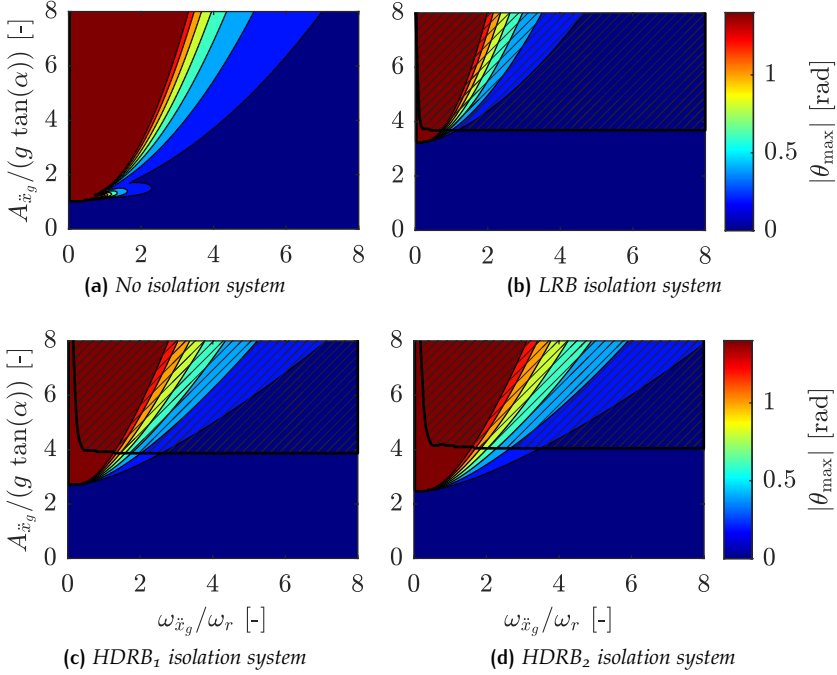


Figure 5.1: Overturning spectra for rigid bodies: without base isolation (a), isolated by the LRB (b), HDRB₁ (c), HDRB₂ (d) isolation systems defined in Table 5.3 and subjected to the full sine cycle. Dark blue colour = safe area; red colour = overturning area; further colours indicate rocking area; 45 degree parallel lines hatch pattern indicates collapse area for elastomeric bearing.

provides a restoring force of the device greater (in absolute value) than the former case, under the same displacement. Figure 5.1d shows that raising of the parameters β_1 and β_2 has the effect to reduce the safe area, given that the minimum overturning acceleration decreases and in addition, the rocking area for high values of the ratio $\omega_{\ddot{x}_g}/\omega_r$ increases.

As regards the failure of the devices, it can be seen that for small values of the ratio $\omega_{\ddot{x}_g}/\omega_r$ the HDRBs devices reach displacements smaller than the LRB one. In addition, such displacements are prone to decrease with increasing values of β_1 and β_2 . In order to establish a numerical quantification of the device failure condition, we denote with A_{LRB} , A_{HDRB_1} , and A_{HDRB_2} the areas in which the LRB, HDRB₁, and HDRB₂ devices fail, respectively. Therefore, the ratios between the above-mentioned quantities are: $A_{LRB}/A_{HDRB_1} \approx 1.05$, $A_{LRB}/A_{HDRB_2} \approx 1.12$, and $A_{HDRB_1}/A_{HDRB_2} \approx 1.06$. Consequently, the HDRB's collapse area tends decrease as the stiffening behaviour increases, what happens if the β parameters are increased. Notably,

the HDRB₁'s collapse area decreases by approximately the six per cent when doubling the β parameters.

The extensive numerical applications carried out show that the elastomeric bearings-base isolation increase the safe area in the overturning spectrum, i.e. the area where the rigid body never rocks. The comparison between the LRB's overturning spectrum and the HDRB one shows that the former provides a safe area greater than the latter. Moreover, if the value of the impulse-to-rigid body angular frequency ratio is conveniently high, what typically happens for big-size bodies or high frequencies pulses, the collapse condition of the device reduces the base-isolated rigid body's safe area in comparison to the non-isolated rigid body one. Consequently, if we decide to isolate a rocking object, it could collapse for the failure of the isolation device.

5.1.2 Wire Rope Isolators

Overturning spectra regarding the rigid bodies having the same geometrical and dynamical properties listed in Table 5.1 and isolated by four WRIs are discussed in this Section. The helical WRI chosen is the PWHS16040 manufactured by Powerflex S.r.l (Limatola, Italy).

The dynamic behaviour of the tested WRI along the two principal horizontal directions, namely Roll and Shear directions (see Figure 3.8), is obtained during an experimental campaign performed at the Department of Structures for Engineering and Architecture of the University of Naples Federico II (Italy) by Vaiana *et al.* [136].

Hysteretic parameters able to reproduce the behaviour of the helical PWHS16040, namely k_a , k_b , λ , β_1 , and β_2 , are calibrated from the experimental hysteresis loops by the in-house software *ParIde* [111] that identifies the parameters of a uniaxial constitutive model by minimising the mean-square error with respect to an experimental target response [112]. This user-friendly software is based on the algorithm described by Sessa *et al.* [113].

The algebraic model's hysteretic parameters used to reproduce the behaviour in both directions, namely Shear and Roll, of the helical WRI PWHS16040, are listed in Table 5.4.

Figure 5.2 shows overturning spectra for rigid bodies isolated by four WRIs loaded in (a) Shear and (b) Roll directions and subjected to the

Table 5.4: Identified model parameters relevant to the experimental hysteresis loops of WRI PWHS16040 tested in Shear and Roll directions.

Direction	k_a [N/m]	k_b [N/m]	λ [-]	β_1 [N m ⁻³]	β_2 [N m ⁻⁵]
Shear	518 970.68	29 107.70	434.19	-1 167 052.18	34 053 603 138.58
Roll	427 786.00	29 995.10	313.45	923 367.84	16 872 030 903.28

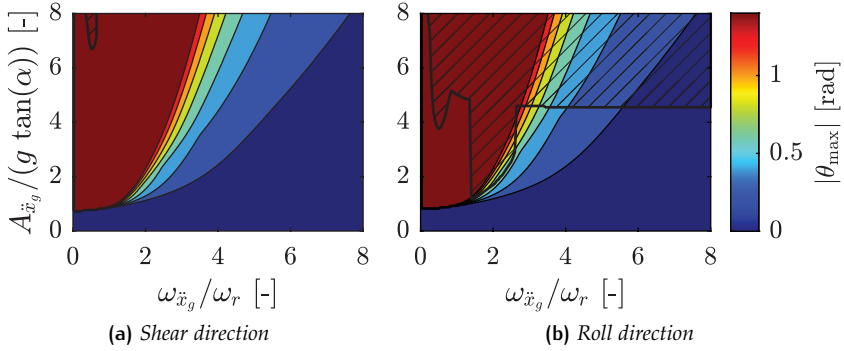


Figure 5.2: The overturning spectra for rigid bodies isolated by four WRIs loaded in (a) Shear and (b) Roll directions and subjected to the full sine cycle. Dark blue colour = safe area; red colour = overturning area; further colours indicate rocking area; 45 degree parallel lines hatch pattern indicates collapse area for WRIs.

full sine cycle. The 45 degree parallel lines hatch pattern represents the area in which the failure condition of the WRI PWHS16040 due to exceeding the device's admissible displacement equal to $x_{max} = 0.07$ m.

The comparison between [Figure 5.2a](#) and [Figure 5.2b](#) highlights that the seismically base-isolated rigid body by means of WRI PWHS16040 in both directions, namely Shear and Roll directions, displays a quite similar rocking behaviour. In both directions, one can see that the minimum overturning acceleration is less than the static one regarding the gravity acceleration if the ratio $\omega_{\ddot{x}_g}/\omega_r$ is very small.

The failure area of the WRI loaded in the Shear direction is practically negligible in comparison to the one regarding the Roll direction, as shown in [Figure 5.2](#). From a mathematical point of view, denoting with A_{Shear} and A_{Roll} the areas in which WRIs loaded in Shear and Roll directions fail, respectively, A_{Roll} is approximately 100 times greater than A_{Shear} .

5.2 APPLICATION OF SCULPTURES SUBJECTED TO SEISMIC EXCITATION

In this Section, the results obtained from some numerical analysis applied to a Caryatid from the Erechtheion, the six of Michelangelo's sculptures, and finally, the Emperor Caracalla's bust of the Farnese collection are discussed. Each of them is subjected to a different earthquake. The effective performances of the proposed isolation systems

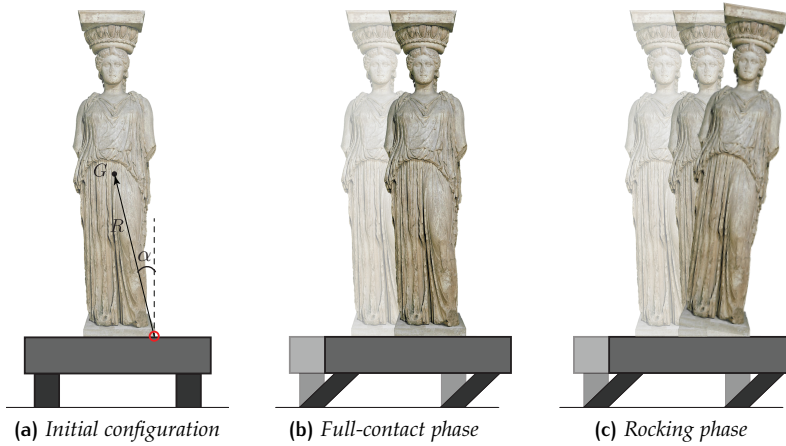


Figure 5.3: The Caryatid from the Erechtheion.

are investigated by comparing the isolated and non-isolated behaviour of each above-mentioned sculpture providing the effectiveness of the isolation systems.

5.2.1 Application of a Caryatid from the Erechtheion

In this Section, the results obtained from some nonlinear time history analyses on the Caryatid from the Erechtheion (see Figure 5.3) modelled as a symmetric rigid body supported on four LRBs are shown. The friction between the statue and the isolated base is supposed to be high enough to avoid the sliding.

The geometrical parameters of the model are the distance R between the centre of gravity and the centre of rotation, and the slenderness α measured as the tilt angle relative to the vertical axis when the body is at rest. Their values are taken from the paper by Constantinides *et al.* [26] who studied the seismic response of six statues belonging to a collection shown at the University of California, Berkeley.

The Caryatid's mass m , equal to 3 172.05 kg, is obtained supposing that the density of Caryatid's material is equal to $2\,650\text{ kg m}^{-3}$. Hence, the Caryatid's fundamental angular rocking frequency is given by

$$\omega_r = \sqrt{\frac{m g R}{J_O}} \approx 2.60\text{ rad s}^{-1},$$

Finally, the mass of the isolated base m_b is supposed to equal to 212 kg.

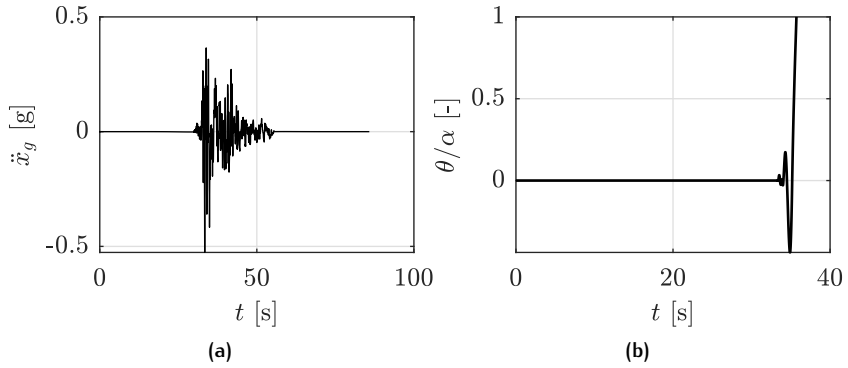


Figure 5.4: The East-West component of the Düzce earthquake acceleration recorded on the 12th of November 1999 (a); Non-isolated Caryatid's rocking response (b).

The East-West component of ground acceleration recorded at the AI_011_DZC station during the Düzce earthquake (Turkey), that occurred on the 12th of November 1999, is used as seismic input. Such an acceleration, displayed in Figure 5.4a, is taken from the Engineering Strong Motion (ESM) database [81]. The rocking response of the non-isolated Caryatid subjected to the above-mentioned acceleration is shown in Figure 5.4b. As a result, the Caryatid needs to be protected since, due to the assumed excitation, it overturns after approximately thirty-five seconds.

Firstly, the Caryatid's rocking spectrum regarding the Düzce earthquake acceleration, see Figure 5.5a, is built. T_r refers to the rocking period. We observe that the Caryatid is vulnerable to such an excitation when its rocking period is less than four seconds. Hence, the base isolation will be efficient if it increases the Caryatid rocking period above four seconds.

Figure 5.5b shows the horizontal displacement spectrum referred to the isolated Caryatid with LRBs devices by increasing the viscous damping factor, where T_{bi} is the isolation period. This spectrum allows one to infer the isolation period and the equivalent viscous damping factor providing a displacement less than the device's maximum allowed displacement, x_{\max} .

The time histories of the rocking angle normalised with respect to the Caryatid's angle α and displacement of the base-isolated Caryatid characterised by the properties shown in Table 5.5 are illustrated in Figure 5.6a and Figure 5.6b, respectively. The adopted constitutive parameters of the model shown in Table 5.5 are obtained from the design procedure described in Section 4.3.

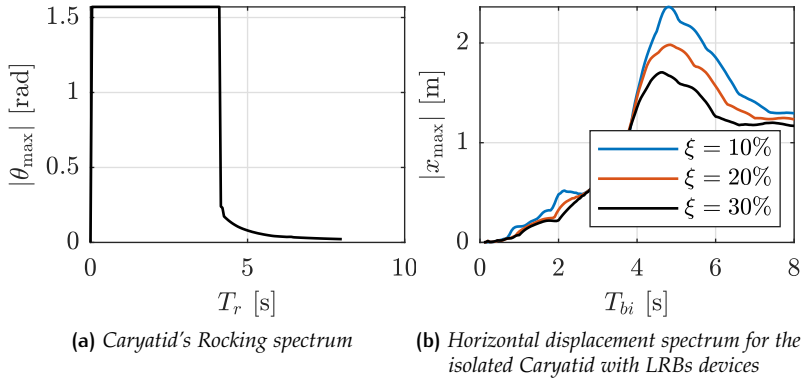


Figure 5.5: Response spectra obtained from the Düzce earthquake acceleration.

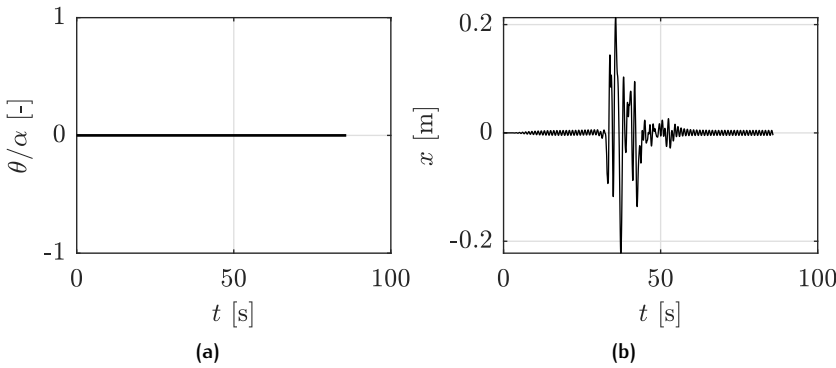


Figure 5.6: The rocking (a) and horizontal displacement (b) responses of the seismically base-isolated Caryatid.

The results are very satisfactory, given that the base-isolated Caryatid does not rock, removing the possibility of damage due to collisions. Moreover, the attained displacements are much smaller than the device's maximum assumed displacement whose value is shown in Table 5.5.

5.2.2 Application of the six of Michelangelo's sculptures

The results obtained from the analyses applied to the six of Michelangelo's sculptures located in the *Galleria dei Prigioni* at the Accademia Gallery of Florence subjected to six different earthquakes are shown and discussed in this Section.

The geometrical properties of such statues, listed in Table 5.6, have been taken from [16] who performed the study of seismic assessment of art objects in museums supposing that the statues were equivalent to a

prismatic block, named *equivalent block*. Although the symmetric model was quite reasonable for most of the statues, the above-mentioned authors concluded that the equivalent block model overestimates the stability capacity of the artefacts compared to a more realistic model accounting for the eccentricities of the centre of mass with respect to the centres of rotations (asymmetric model).

The masses listed in Table 5.6 are obtained supposing that the density of each statue was 2650 kg m^{-3} .

Nonlinear time history analyses have been conducted supposing that the mass of the isolated base m_b is the one showed in Table 5.1 and assuming the following seismic inputs:

- the Strike Parallel direction of the horizontal ground acceleration recorded at the Jensen Filter Plant station during the Northridge earthquake of January 17, 1994;
- the 000 component of the horizontal ground acceleration recorded at the Gilroy Array #1 station during the Loma Prieta earthquake of October 18, 1989;
- the 180 component of the horizontal ground acceleration recorded at the Geotech. Investig. Center station during the San Salvador earthquake of October 10, 1986;
- the East-West component of the horizontal ground acceleration recorded at the Gemona station during the Friuli earthquake of September 15, 1976;
- the North-South component of the horizontal ground acceleration recorded at the Mire station during the Emilia earthquake of May 5, 2012;
- the North-South component of the horizontal ground acceleration recorded at the Domo station during the Central Italy earthquake of October 6, 2016.

First of all, we investigated the rocking behaviour of the statues without the base isolation. Figure 5.7 displays the rocking angle θ normalised with respect to the angle α versus the time of each statue subjected to the Northridge earthquake. All statues rock and two of these, namely *San Matteo* and *Prigione che si Sveglia*, overturn. The same conclusions are derived from the Central Italy earthquake. All statues

Table 5.5: LRBS' properties and the model constitutive parameters of the model

n_d [-]	T_{bi} [s]	x_{\max} [m]	ζ [%]	k_a [N m^{-1}]	k_b [N m^{-1}]	λ [-]
4	2	0.30	30	6.22×10^4	6.22×10^3	44.69

rock without overturning when they are subjected to the Loma Prieta as well as the San Salvador earthquakes. Only *San Matteo* overturns due to Friuli earthquake, while the remaining sculptures rock. The Emilia earthquake does not cause overturning of the sculptures, even though the *San Matteo* and *Prigione che si Sveglia* statues rock. For completeness we show in Figure 5.8 the results obtained for the *San Matteo* statue subjected to the above-mentioned seismic inputs. In any case, in addition to overturning, rocking is an unsatisfactory behaviour because of the possible damages that the collisions cause with the pedestal [39, 47, 70]. Consequently, all the statues need to be protected from seismic excitations.

Figure 5.9 shows the Full-Contact spectra regarding the seismically base-isolated rigid body with four LRBs, whose properties are listed in Table 5.7, and subjected to the six seismic excitations. The spectra are referred to one value of the viscous damping factor ζ , namely 15% and depicts the evolution of $|x_{\max}|$ with respect to the isolation period T_{bi} . The other properties of the LRBs, i.e. the admissible displacement, and the initial-to-post yield stiffness ratio are reported in Table 5.2.

We can see that lower values of the horizontal displacement are reached by choosing a value of the isolation period ranging from approximately 2.5 to 5.3 seconds. We chose $T_{bi} = 3.7$ seconds for further analyses (see Table 5.7).

The hysteretic model parameters have been obtained for each statue according to the above detailed design procedure and are reported in Table 5.8 where the parameters β_1 and β_2 have been omitted since they are null for the LRBs isolation system. The numerical results show that both collapse conditions, namely overturning of the statues and failure of the devices, are never attained. Moreover, all statues never rock and this avoids the possibility of damage due to impacts. For brevity, in Figure 5.10 we reported just the time-displacement relationships

Table 5.6: The geometrical properties (see Figure 2.6) of the equivalent blocks of the six of Michelangelo's sculptures located in the *Galleria dei Prigioni* at the Accademia Gallery of Florence [16].

	b [m]	h [m]	m [kg]
<i>San Matteo</i>	0.30	1.36	3 287
<i>Pietà da Palestrina</i>	0.39	1.26	7 084
<i>Prigione che si Sveglia</i>	0.32	1.41	5 644
<i>Prigione il Giovane</i>	0.36	1.28	4 005
<i>Prigione Barbuto</i>	0.37	1.29	4 655
<i>Prigione Atlante</i>	0.45	1.39	7 691

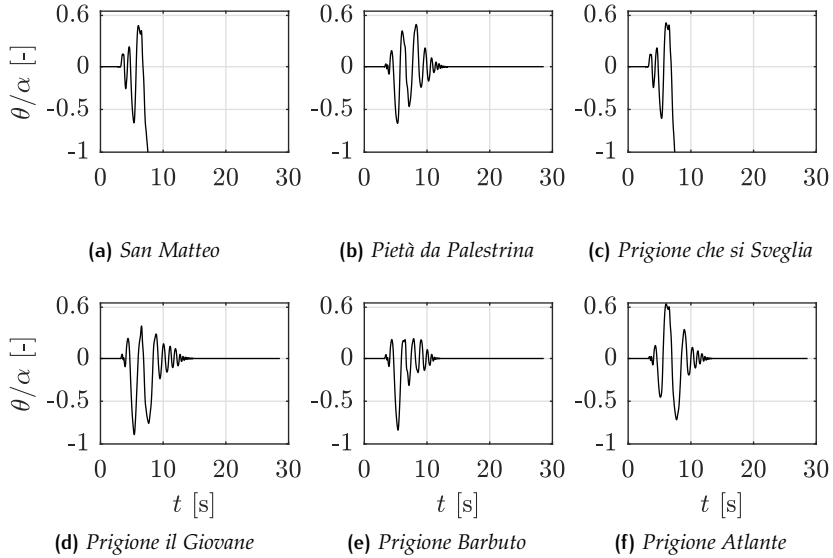


Figure 5.7: Rocking response of the Michelangelo’s sculptures located in the *Galleria dei Prigioni* at the Accademia Gallery of Florence subjected to the horizontal ground acceleration recorded during the Northridge earthquake (1994).

concerning the six seismic excitations considered since the time-rocking angle relationships are always null for every statue.

The same analyses have been carried out considering the HDRBs devices as an isolation system. Table 5.9 presents the devices’ properties providing the same results, in terms of time-rocking angle relationship, of the LRB isolation. The related hysteretic model parameters obtained by the design procedure are listed in Table 5.10. For the sake of simplicity, we chose the same β_1 and β_2 parameters for all statues, although an *ad hoc* calibration for each statue would be needed in order to have stiffening behaviour at a relative large values of shear strain.

Both the LRB and the HDRB satisfied the assumed ultimate limit states, i.e. no overturning, no breaking of the devices, and no rocking. Especially, the HDRB device adopted to isolate the statues turned out to be less damped and more deformable than the LRB.

Table 5.7: The properties considered to evaluate the algebraic model parameters for the isolation of the Michelangelo’s sculptures with the LRBs.

n_d [-]	T_{bi} [s]	x_{\max} [m]	ζ [%]	η [-]
4	3.7	0.30	15	10

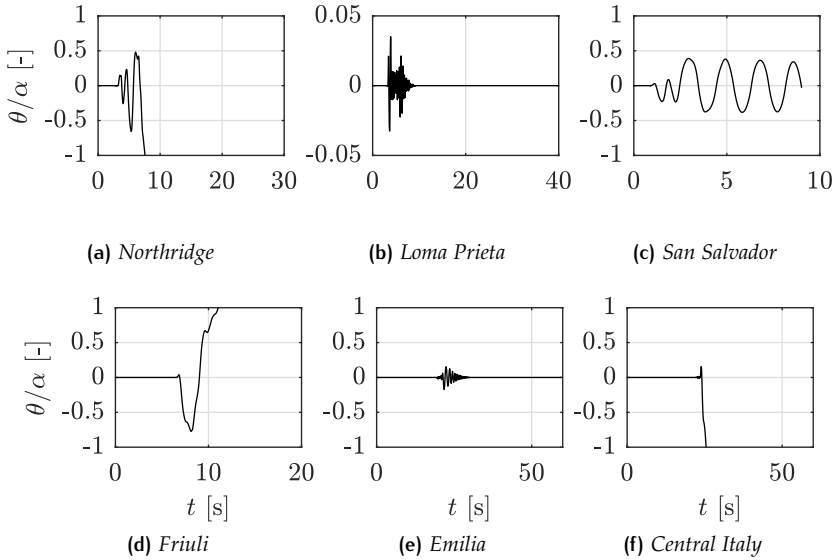


Figure 5.8: Rocking response of the *San Matteo* statue located in the *Galleria dei Prigioni* at the Accademia Gallery of Florence subjected to the: (a) Northridge, (b) Loma Prieta, (c) San Salvador, (d) Friuli, (e) Emilia, and (f) Central Italy seismic excitations.

5.2.3 Application of the Emperor Caracalla's bust

This Section illustrates the advantages of seismic isolation by means of helical Wire Rope Isolators (WRIs) when adopted to protect the Emperor Caracalla's bust of the Farnese collection (Naples, Italy).

The fundamental rigid body properties are the mass $m = 241.15$ kg, the distance $R \approx 0.69$ m, and the angle $\alpha \approx 0.22$ rad, see [Figure 5.11](#). These properties has been computed by a three-dimensional computer graphic model taken from the platform *Scan The World*. Subsequently, the fundamental angular rocking frequency of Emperor Caracalla's bust is

$$\omega_r = \sqrt{\frac{m g R}{J_O}} \approx 3.26 \text{ rad s}^{-1}$$

We assumed the following hypotheses: the sliding motion between the bust and the isolated base is negligible, while the rotation as well as vertical movement of the pedestal is avoided. The former hypothesis can be verified supposing either that the friction between the statue and the isolated base is very high or the existence of a clip constraining block translation movements. Instead, combining the helical WRIs with

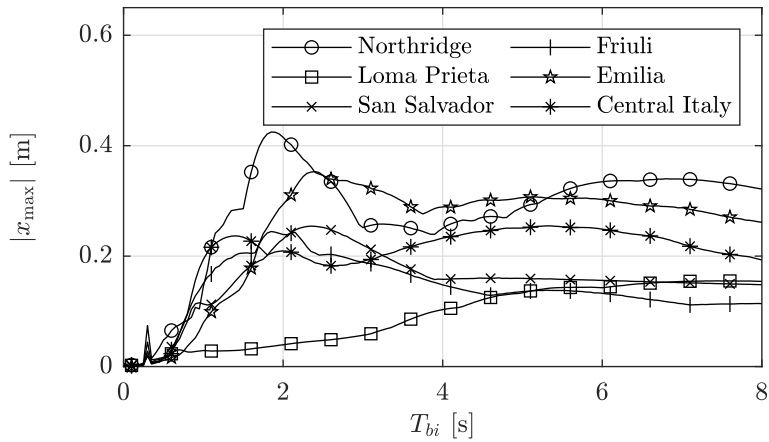


Figure 5.9: Full-Contact spectra referring to the seismically base-isolated rigid body with four LRBs whose admissible displacement, viscous damping factor and initial-to-post yield stiffness ratio are listed in [Table 5.7](#).

slider constraints, the rotation and vertical movements of the pedestal are avoided, see [Figure 5.11](#).

The typology of WRI chosen to protect Emperor Caracalla's bust is the PWHS16040, the same shown in [Section 5.1.2](#). We selected the PWHS16040 because of its high energy dissipation properties, as shown during the experimental campaign, allowing one to use the minimum number of isolators to protect the art object.

The algebraic model's hysteretic parameters used to reproduce the behaviour in both directions, namely Shear and Roll, of the helical WRI PWHS16040, are listed in [Table 5.4](#).

The East-West and the vertical components of ground accelerations recorded at the Sturno station during the Irpinia earthquake (Italy), that occurred on the 23rd of November 1980, are used as seismic inputs.

Table 5.8: The algebraic model parameters obtained from the LRBs' properties listed in [Table 5.7](#) by means of the energy-based design procedure.

	k_b [N m ⁻¹]	λ [-]
<i>San Matteo</i>	2.26×10^3	109.37
<i>Pietà da Palestrina</i>	4.67×10^3	109.37
<i>Prigione che si Sveglia</i>	3.76×10^3	109.37
<i>Prigione il Giovane</i>	2.72×10^3	109.37
<i>Prigione Barbuto</i>	3.13×10^3	109.37
<i>Prigione Atlante</i>	5.05×10^3	109.37

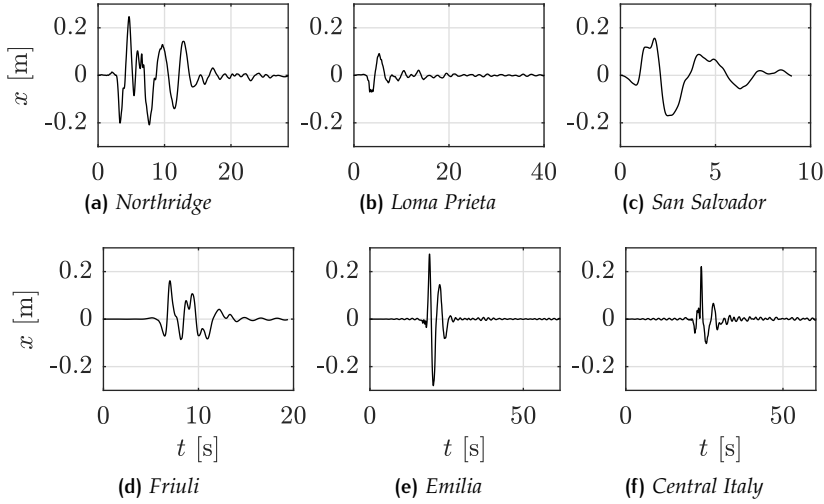


Figure 5.10: The displacement time histories of the seismically base-isolated rigid body with the LRBs isolation system, whose properties are listed in Table 5.7, subjected to the: (a) Northridge, (b) Loma Prieta, (c) San Salvador, (d) Friuli, (e) Emilia, and (f) Central Italy seismic excitations.

These accelerations, displayed in Figure 5.12a and Figure 5.12b, have been taken from the Engineering Strong Motion (ESM) database.

Figure 5.12c depicts the rocking response of the non-isolated Emperor Caracalla's bust subjected to the above-mentioned accelerations. As a consequence, the Emperor Caracalla's bust needs to be protected, since due to the assumed excitations, it overturns after approximately twenty-two seconds.

Figure 5.13 and Figure 5.14 illustrate the time histories of the rocking angle (a) and displacement (b) of Emperor Caracalla's bust isolated by three helical WRIs disposed along the Shear and Roll directions, respectively. The results in both directions are satisfactory, since the rocking angle and the attained displacement are very small. However, the WRIs located in the Shear direction provide the best behaviour because of

Table 5.9: The properties considered to evaluate the algebraic model parameters for the isolation of the Michelangelo's sculptures with the HDRBs.

n_d [-]	T_{bi} [s]	x_{\max} [m]	ζ [%]	η [-]
4	3.7	0.35	15	5

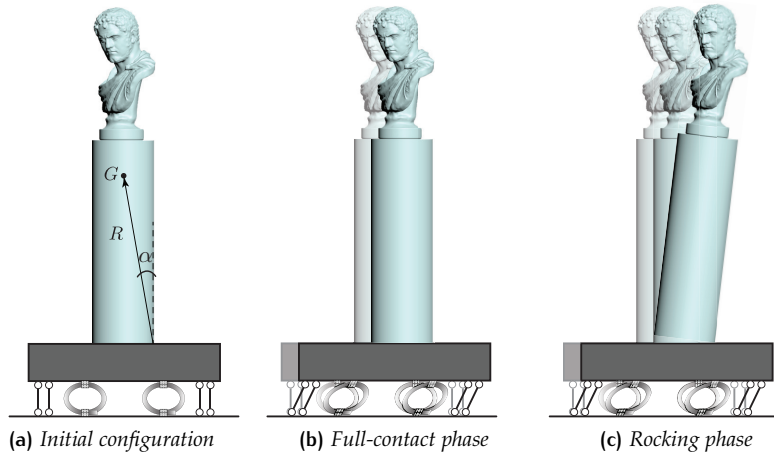


Figure 5.11: Emperor Caracalla's bust of the Farnese collection (Naples, Italy).

significant energy dissipation due to the device's deformability in that direction.

We performed further analyses selecting seven ground accelerations compatible with the design spectra defined by the Italian Building Code. The seven records, listed in Tab. 5.11, have been obtained by using the *REXEL* software (Iervolino *et al.* [61]) regarding the site's National Archaeological Museum of Naples, in which there is the Farnese collection, and the limit state of the Italian code-based spectrum. The records have been found in specific ranges of moment magnitude M_w , i.e. [5, 7], and epicentral distance R , that is [0 km, 30 km]. In particular, we have chosen the period range [0.15 s, 4.0 s] in which the seven records are made compatible, to the average, with the design spectrum.

Table 5.10: The algebraic model parameters obtained from the HDRBs' properties listed in Table 5.9 by means of the energy-based design procedure.

	k_b [N m ⁻¹]	λ [-]	β_1 [N m ⁻³]	β_2 [N m ⁻⁵]
<i>San Matteo</i>	2250	40.16	1×10^4	1×10^4
<i>Pietà da Palestrina</i>	4640	40.16	1×10^4	1×10^4
<i>Prigione che si Sveglia</i>	3730	40.16	1×10^4	1×10^4
<i>Prigione il Giovane</i>	2700	40.16	1×10^4	1×10^4
<i>Prigione Barbuto</i>	3110	40.16	1×10^4	1×10^4
<i>Prigione Atlante</i>	5020	40.16	1×10^4	1×10^4

Table 5.11: REXEL outputs.

ID	Earthquake Name	Date	Mw	R [km]	PGA-X [m s^{-2}]	PGA-Y [m s^{-2}]
1	Campano Lucano	23 rd Nov 1980	6.9	25	0.5878	0.5876
2	Bingol	1 st May 2003	6.3	14	5.0514	2.9178
3	Mt. Hengill Area	4 th Jun 1998	5.4	23	0.1695	0.1581
4	Mt. Hengill Area	4 th Jun 1998	5.4	18	0.1325	0.2386
5	Friuli	6 th May 1976	6.5	23	3.4985	3.0968
6	South Iceland-X	17 th Jun 2000	6.5	5	3.1176	3.3109
7	South Iceland-Y	17 th Jun 2000	6.5	5	3.1176	3.3109

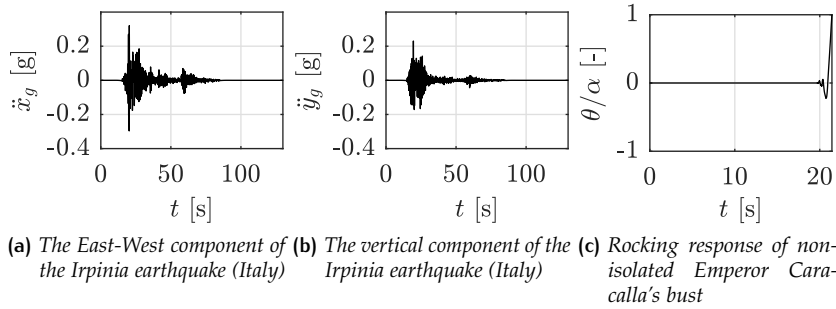


Figure 5.12: Numerical results of non-isolated Emperor Caracalla's bust by using the horizontal and vertical components of the Irpinia earthquake (Italy).

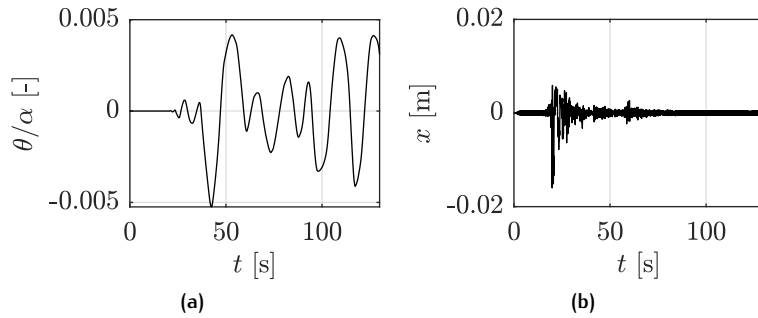


Figure 5.13: The rocking (a) and horizontal displacement (b) responses of the seismically base-isolated Emperor Caracalla's bust endowed with WRIs loaded in the in Shear direction.

For completeness, we have also carried out a one-dimensional analysis of the local seismic response. In this way, we can take into account the change of magnitude and frequency content due to the propagation of waves from bedrock to surface. Firstly, we used the *SeismoSignal* software (see References) to filter and baseline-correct the seven records provided by *REXEL*. The Butterworth filter with a bandpass between 0.10 and 25 Hz was chosen accordingly.

Soil properties such as unit weight, thickness and velocity of the secondary waves of each ground layer, have been taken from a geological survey regarding the requalification of the ex Civil Registry located in Dante Square (Naples). Soil type, soil profile and acceleration records regarding bedrock have been used as input to *STRATA* (see References), the software adopted to evaluate the local seismic response.

Fig. 5.15 shows the horizontal displacement response of the isolated Emperor Caracalla's bust by three helical WRIs disposed along the Shear (see Fig. 5.15(a)) and Roll (see Fig. 5.15(b)) directions, respectively.

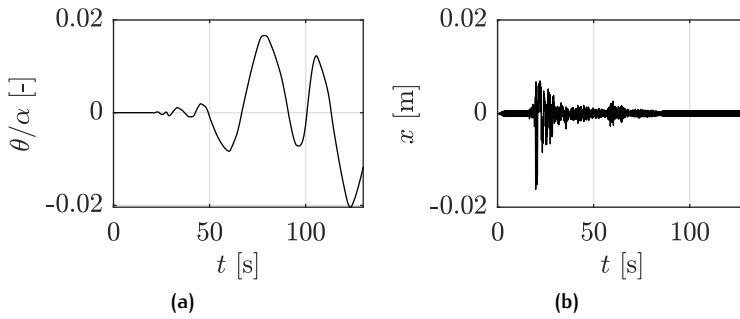
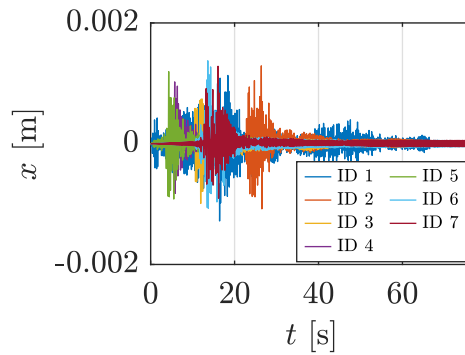


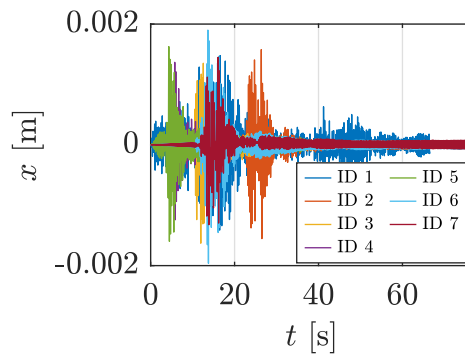
Figure 5.14: The rocking (a) and horizontal displacement (b) responses of the seismically base-isolated Emperor Caracalla's bust by WRIs loaded in the Roll direction.

The rocking responses have been omitted because they are negligible. The results show that the lowest displacements are attained when the WRIs are loaded along the Shear direction, as shown in the previous result.

In conclusion, the efficiency of the proposed isolation system can be assessed independently of the frequency contents of the earthquake due to the rate-independent nature of the WRIs in the small displacements range, a property thoroughly proved by the experimental studies conducted by Demetriades *et al.* [34] and Alessandri *et al.* [4]. In addition, the proposed isolation system works satisfactorily even if the magnitude and the frequency content of the ground acceleration change due to seismic site effects.



(a) Shear direction



(b) Roll direction

Figure 5.15: The horizontal displacements responses of the seismically base-isolated Emperor Caracalla's bust by WRIs loaded in the Shear (a) and Roll (b) directions.

6

CONCLUSIONS AND PERSPECTIVES

The present dissertation has addressed the rocking behaviour of rigid bodies, the seismic protection of statues standing on base isolation made by elastomeric isolators such as Lead Rubber Bearings and High Damping Rubber Bearings, and special devices named Wire Rope Isolators.

The complex hysteretic behaviour displayed by such devices has been modelled by a uniaxial phenomenological model that offers many advantages.

First, the model is based on a small set of parameters, directly associated with the mechanical properties of the device's hysteretic behaviour to be simulated.

Second, the model's algebraic nature and the straight forward mechanical interpretation of the model parameters make it possible to define a new design procedure that allows one to obtain the hysteretic model parameters starting from easily available properties, i.e. the mass and the period of the system to isolate, the number, admissible displacement, viscous damping factor, and the initial-to-post yield tangent stiffness ratio of the isolator. This design process exploits an energetic approach based on an equivalent viscous system.

Last, but not least, the model's validation and its accuracy have been successfully experienced in several papers [133–135].

The extensive numerical applications carried out show that the elastomeric bearings-base isolation increase the safe area in the overturning spectrum, i.e. the area where the rigid body never rocks. The comparison between the LRB's overturning spectrum and the HDRB one shows that the former provides a safe area greater than the one associated with the latter. Moreover, if the value of the impulse-to-rigid body angular frequency ratio is conveniently high, what typically happens for big-size bodies or high frequencies pulses, the collapse condition of the device reduces the base-isolated rigid body's safe area in comparison to the non-isolated rigid body one. Consequently, if one decides to isolate a rocking object, it could collapse for the failure of the isolation device. In addition, the collapse area for both the LRB and the two HDRBs isolators have been compared.

Numerical assessments have been carried out on a Caryatid from the Erechtheion subjected to the 1999 Düzce earthquake (Turkey), with and without isolation. After approximately thirty-five seconds the statue without isolation overturns. Consequently, a base isolation supported

on four Lead Rubber Bearings as seismic protection system has been considered. Firstly, the rocking and horizontal displacement response spectra of the statue subjected to seismic excitation has been computed in order to establish the isolation period and the device's maximum displacement to exploit. The results have shown that the Lead Rubber Bearings isolation system not only avoids overturning of the Caryatid, but it completely removes the rocking motion; hence, any kind of damage due to collision is avoided. Moreover, the horizontal displacements attained by the base-isolated Caryatid are less than the maximum displacement allowed for the adopted device.

The dissertation also includes the results referred to six of Michelangelo's sculptures located in the *Galleria dei Prigioni* at the Accademia Gallery of Florence subjected to six earthquakes with pulse-like behaviour. The Full-Contact spectrum of the isolated system under seismic excitations was computed to choose the isolation period, admissible displacement and equivalent viscous damping of the devices. In this way, it has been possible to apply the design procedure in order to obtain the mechanical properties of the devices for each statue. Both the LRB and the HDRB satisfied the assumed ultimate limit states, i.e. absence of overturning, breaking of the devices, and of rocking. Especially, the HDRB device adopted to isolate the statues turned out to be less damped and more deformable than the LRB.

Finally, the rocking behaviour of the Emperor Caracalla's bust of the Farnese collection (Naples, Italy) subjected to the 1980 Irpinia earthquake (Italy) has been investigated. Base isolation allowed by three helical wire rope isolators acting as seismic protection system has been considered since the stability of the bust is unable to resist the oscillations induced by the considered earthquake. The constitutive model parameters of the adopted device, namely the PWHS 16040, have been identified in both directions (Shear and Roll) from experimental hysteresis loops by means of the in-house software Parameter Identification (ParIde). Numerical results have shown that the base isolation with three helical wire ropes in Shear and Roll directions avoids overturning and provides small rocking angle and displacement.

Future developments of the research will address the adoption of a statistical approach to design these sensitive objects correctly. Actually, several studies have highlighted the significant record-to-record variability associated with rocking response (see e.g. Klaboe *et al.* [69] and Bachmann *et al.* [11]).

In addition, considering earthquakes with pulse-like behaviour, that represent the most dangerous actions for freestanding objects, a perspective of this study will be the use of overturning spectra to understand the effective equilibrium state of the rocking art object. Specially, each set of records compatible, in the average, with the design spectra

according to design codes can be transformed in a wavelet that is a rapidly decaying, wave-like oscillation that has zero mean.

Unlike sinusoids, which extend to infinity, a wavelet exists for a finite duration. Consequently, the wavelets transform decomposes the seismic signal as the sum of wavelets that are well localised in time and frequency. In this way, an overturning spectrum can be computed for each wavelet in order to establish the equilibrium state of the rocking art object.

This can alleviate the shortcomings of the classical Fourier transform that using sine waves to represent functions is not able to suitably represent those functions that are not localised in time or space.

BIBLIOGRAPHY

- [1] M. Agbabian, W. Ginell, S. Masri, and R. Nigbor, "Evaluation of earthquake damage mitigation methods for museum contents," *Studies in Conservation*, vol. 36, pp. 111–120, 1991. DOI: <https://doi.org/10.2307/1506335>.
- [2] M. Agbabian, S. Masri, R. Nigbor, and G. C. Institute, *Evaluation of Seismic Mitigation Measures for Art Objects Getty Seismic Adobe Project*, ser. GCI scientific program reports. J. Paul Getty Trust, 1990, ISBN: 9780892365876.
- [3] S. Alessandri, R. Giannini, F. Paolacci, M. Amoretti, and A. Freddo, "Seismic retrofitting of an hv circuit breaker using base isolation with wire ropes. part 2: Shaking-table test validation," *Engineering Structures*, vol. 98, pp. 263–274, 2015. DOI: <https://doi.org/10.1016/j.engstruct.2015.03.031>.
- [4] S. Alessandri, R. Giannini, F. Paolacci, and M. Malena, "Seismic retrofitting of an hv circuit breaker using base isolation with wire ropes. part 1: Preliminary tests and analyses," *Engineering Structures*, vol. 98, pp. 251–262, 2015. DOI: <https://doi.org/10.1016/j.engstruct.2015.03.032>.
- [5] M. Antonelli, B. Carboni, W. Lacarbonara, D. Bernardini, and T. Kalmár-Nagy, "Quantifying rate-dependence of a nonlinear hysteretic device," in *Nonlinear Dynamics of Structures, Systems and Devices*. 2020, pp. 347–355. DOI: https://doi.org/10.1007/978-3-030-34713-0_35.
- [6] M. Aslam, W. G. Godden, and D. T. Scalise, "Earthquake rocking response of rigid bodies," Prepared for the Department of Energy under Contract W-7405-ENG-48, EERC 2003-07, 1978.
- [7] G. Augusti, M. Ciampoli, and L. Airoidi, "Mitigation of seismic risk for museum contents an introductory investigation," in *Proceedings of 10th World Conference on Earthquake Engineering (10WCEE)*, Madrid, Spain, Jul. 1992, pp. 5995–6000.
- [8] T. T. Baber and M. N. Noori, "Random vibration of degrading, pinching systems," *Journal of Engineering Mechanics*, vol. 111, no. 8, pp. 1010–1026, 1985. DOI: [https://doi.org/10.1061/\(ASCE\)0733-9399\(1985\)111:8\(1010\)](https://doi.org/10.1061/(ASCE)0733-9399(1985)111:8(1010)).

- [9] T. T. Baber and M. N. Noori, "Modeling general hysteresis behavior and random vibration application," *Journal of Vibration, Acoustics, Stress, and Reliability in Design*, vol. 108, no. 4, pp. 411–420, 1986. DOI: <https://doi.org/10.1115/1.3269364>.
- [10] T. T. Baber and Y.-K. Wen, "Random vibration of hysteretic, degrading systems," *Journal of the Engineering Mechanics Division*, vol. 107, no. 6, pp. 1069–1087, 1981. DOI: <https://doi.org/10.1061/JMCEA3.0002768>.
- [11] J. A. Bachmann, M. Strand, M. F. Vassiliou, M. Broccardo, and B. Stojadinović, "Is rocking motion predictable?" *Earthquake Engineering & Structural Dynamics*, vol. 47, no. 2, pp. 535–552, 2018. DOI: <https://doi.org/10.1002/eqe.2978>.
- [12] S. Baggio, L. Berto, I. Rocca, and A. Sietta, "Vulnerability assessment and seismic mitigation intervention for artistic assets: From theory to practice," *Engineering Structures*, vol. 167, pp. 272–286, 2018. DOI: <https://doi.org/10.1016/j.engstruct.2018.03.093>.
- [13] H. Banon and D. Veneziano, "Seismic safety of reinforced concrete members and structures," *Earthquake Engineering & Structural Dynamics*, vol. 10, no. 2, pp. 179–193, 1982. DOI: <https://doi.org/10.1002/eqe.4290100202>.
- [14] N. Barbieri, R. Barbieri, R. A. da Silva, M. J. Mannala, and L. Barbieri, "Nonlinear dynamic analysis of wire-rope isolator and stockbridge damper," *Nonlinear Dynamics*, vol. 86, no. 1, pp. 501–512, 2016. DOI: <https://doi.org/10.1007/s11071-016-2903-1>.
- [15] L. Berto, T. Favaretto, and A. Sietta, "Seismic risk mitigation technique for art objects: Experimental evaluation and numerical modelling of double concave curved surface sliders," *Bulletin of Earthquake Engineering*, vol. 11, no. 5, pp. 1817–1840, 2013. DOI: <https://doi.org/10.1007/s10518-013-9441-8>.
- [16] L. Berto, T. Favaretto, A. Sietta, F. Antonelli, and L. Lazzarini, "Assessment of seismic vulnerability of art objects: The "Galleria dei Prigioni" sculptures at the Accademia Gallery in Florence," *Journal of Cultural Heritage*, vol. 13, no. 1, pp. 7–21, 2012. DOI: <https://doi.org/10.1016/j.culher.2011.06.005>.
- [17] L. Berto, E. Meroi, I. Rocca, and A. Sietta, "Rocking activation of free standing elements in real conditions: A safe experimentally-based acceleration limit," *Engineering Structures*, vol. 226, p. 111 331, 2021. DOI: <https://doi.org/10.1016/j.engstruct.2020.111331>.
- [18] R. Bouc, "Forced vibrations of a mechanical system with hysteresis," in *Proceedings of 4th Conference on Non-linear Oscillations*, Prague, Czech Republic, 1967.

- [19] R. Bouc, "Modèle mathématique d'hystérésis," *Acustica*, vol. 24, no. 1, pp. 16–25, 1971.
- [20] I. Calìo and M. Marletta, "Passive control of the seismic rocking response of art objects," *Engineering Structures*, vol. 25, no. 8, pp. 1009–1018, 2003. DOI: [https://doi.org/10.1016/S0141-0296\(03\)00045-2](https://doi.org/10.1016/S0141-0296(03)00045-2).
- [21] I. Calìo and M. Marletta, "On the mitigation of the seismic risk of art objects: Case-studies," in *Proceedings of 13th World Conference on Earthquake Engineering*, 2004.
- [22] G. D. Canio, "Marble devices for the base isolation of the two bronzes of riace: A proposal for the david of michelangelo," in *Proceedings of 15th World Conference on Earthquake Engineering (15WCEE)*, Lisbon, Portugal, Sep. 2012.
- [23] B. Carboni, W. Lacarbonara, P. T. Brewick, and S. F. Masri, "Dynamical response identification of a class of nonlinear hysteretic systems," *Journal of Intelligent Material Systems and Structures*, vol. 29, no. 13, pp. 2795–2810, 2018. DOI: <https://doi.org/10.1177/1045389X18778792>.
- [24] R. Ceravolo, M. L. Pecorelli, and L. Zanotti Fragonara, "Semi-active control of the rocking motion of monolithic art objects," *Journal of Sound and Vibration*, vol. 374, pp. 1–16, 2016. DOI: <https://doi.org/10.1016/j.jsv.2016.03.038>.
- [25] A. Chopra, *Dynamics of Structures: Theory and Applications to Earthquake Engineering*. Prentice Hall, 2000.
- [26] M. Constantinides, N. Makris, and S. Miller, "Seismic response analysis of plaster cast sculptures on the university of california, berkeley campus," Earthquake Engineering Research Center, University of California, Berkeley, EERC 2003-07, 2003.
- [27] M. C. Constantinou, A. S. Whittaker, Y. Kalpakidis, D. M. Fenz, and G. P. Warn, "Performance of seismic isolation hardware under service and seismic loading," Multidisciplinary Center for Earthquake Engineering Research: Buffalo, NY, USA, Tech. Rep., 2007.
- [28] M. Constantinou, T. Soong, and G. Dargush, "Passive energy dissipation systems for structural design and retrofit, monograph no. 1," Multidisciplinary Center for Earthquake Engineering Research: Buffalo, NY, USA, Tech. Rep., 1998.
- [29] A. Contento and A. Di Egidio, "Investigations into the benefits of base isolation for non-symmetric rigid blocks," *Earthquake Engineering & Structural Dynamics*, vol. 38, no. 7, pp. 849–866, 2009. DOI: <https://doi.org/10.1002/eqe.870>.

- [30] A. Contento and A. Di Egidio, "On the use of base isolation for the protection of rigid bodies placed on a multi-storey frame under seismic excitation," *Engineering Structures*, vol. 62-63, pp. 1–10, 2014. DOI: <https://doi.org/10.1016/j.engstruct.2014.01.019>.
- [31] D. D'Angela, G. Magliulo, and E. Cosenza, "Seismic damage assessment of unanchored nonstructural components taking into account the building response," *Structural Safety*, vol. 93, p. 102 126, 2021. DOI: <https://doi.org/10.1016/j.strusafe.2021.102126>.
- [32] D. D'Angela, G. Magliulo, and E. Cosenza, "Towards a reliable seismic assessment of rocking components," *Engineering Structures*, vol. 230, p. 111 673, 2021. DOI: <https://doi.org/10.1016/j.engstruct.2020.111673>.
- [33] M. J. DeJong, "Amplification of rocking due to horizontal ground motion," *Earthquake Spectra*, vol. 28, no. 4, pp. 1405–1421, 2012. DOI: <https://doi.org/10.1193/1.4000085>.
- [34] G. Demetriades, M. Constantinou, and A. Reinhorn, "Study of wire rope systems for seismic protection of equipment in buildings," *Engineering Structures*, vol. 15, no. 5, pp. 321–334, 1993. DOI: [https://doi.org/10.1016/0141-0296\(93\)90036-4](https://doi.org/10.1016/0141-0296(93)90036-4).
- [35] A. Di Egidio, R. Alaggio, A. Aloisio, A. M. de Leo, A. Contento, and M. Tursini, "Analytical and experimental investigation into the effectiveness of a pendulum dynamic absorber to protect rigid blocks from overturning," *International Journal of Non-Linear Mechanics*, vol. 115, pp. 1–10, 2019. DOI: <https://doi.org/10.1016/j.ijnonlinmec.2019.04.011>.
- [36] A. Di Egidio and A. Contento, "Base isolation of slide-rocking non-symmetric rigid blocks under impulsive and seismic excitations," *Engineering Structures*, vol. 31, no. 11, pp. 2723–2734, 2009. DOI: <https://doi.org/10.1016/j.engstruct.2009.06.021>.
- [37] A. Di Egidio, A. Contento, C. Olivieri, and A. M. de Leo, "Protection from overturning of rigid block-like objects with linear quadratic regulator active control," *Structural Control and Health Monitoring*, vol. 27, no. 10, e2598, 2020. DOI: <https://doi.org/10.1002/stc.2598>.
- [38] A. Di Egidio, G. Simoneschi, and A. Leo, "Active control methods to improve the seismic response of rigid block-like structures," in *Proceedings of 16th European Conference on Earthquake Engineering*, 2018.

- [39] L. Di Sarno, G. Magliulo, D. D'Angela, and E. Cosenza, "Experimental assessment of the seismic performance of hospital cabinets using shake table testing," *Earthquake Engineering & Structural Dynamics*, vol. 48, no. 1, pp. 103–123, 2019. DOI: <https://doi.org/10.1002/eqe.3127>.
- [40] M. Dimian and P. Andrei, *Noise-Driven Phenomena in Hysteretic Systems*, ser. Signals and Communication Technology. Springer, New York, NY, 2014. DOI: <https://doi.org/10.1007/978-1-4614-1374-5>.
- [41] E. G. Dimitrakopoulos and M. J. DeJong, "Revisiting the rocking block: Closed-form solutions and similarity laws," *Proceedings of the Royal Society A: Mathematical, Physical and Engineering Sciences*, vol. 468, no. 2144, pp. 2294–2318, 2012. DOI: <https://doi.org/10.1098/rspa.2012.0026>.
- [42] E. G. Dimitrakopoulos and E. D. W. Fung, "Closed-form rocking overturning conditions for a family of pulse ground motions," *Proceedings of the Royal Society A: Mathematical, Physical and Engineering Sciences*, vol. 472, no. 2196, p. 20160662, 2016. DOI: <https://doi.org/10.1098/rspa.2016.0662>.
- [43] E. G. Dimitrakopoulos and T. S. Paraskeva, "Dimensionless fragility curves for rocking response to near-fault excitations," *Earthquake Engineering & Structural Dynamics*, vol. 44, no. 12, pp. 2015–2033, 2015. DOI: <https://doi.org/10.1002/eqe.2571>.
- [44] S. Dobson, M. Noori, Z. Hou, M. Dimentberg, and T. Baber, "Modeling and random vibration analysis of sdof systems with asymmetric hysteresis," *International Journal of Non-Linear Mechanics*, vol. 32, no. 4, pp. 669–680, 1997. DOI: [https://doi.org/10.1016/S0020-7462\(96\)00090-X](https://doi.org/10.1016/S0020-7462(96)00090-X).
- [45] P. Duhem, "Die dauernden aenderungen und die thermodynamik. i," *Zeitschrift für Physikalische Chemie*, vol. 22U, no. 1, pp. 545–589, 1897. DOI: <https://doi.org/10.1515/zpch-1897-2250>.
- [46] G. C. Foliente, "Hysteresis modeling of wood joints and structural systems," *Journal of Structural Engineering*, vol. 121, no. 6, pp. 1013–1022, 1995. DOI: [https://doi.org/10.1061/\(ASCE\)0733-9445\(1995\)121:6\(1013\)](https://doi.org/10.1061/(ASCE)0733-9445(1995)121:6(1013)).
- [47] M. Fragiadakis and S. Diamantopoulos, "Fragility and risk assessment of freestanding building contents," *Earthquake Engineering & Structural Dynamics*, vol. 49, no. 10, pp. 1028–1048, 2020. DOI: <https://doi.org/10.1002/eqe.3276>.

- [48] T. Fujita, S. Suzuki, and S. Fujita, "High damping rubber bearings for seismic isolation of buildings (1st report, Hysteretic restoring force characteristics and analytical models)," *Transactions of the Japan Society of Mechanical Engineers Series C*, vol. 56, pp. 658–666, 1990. DOI: <https://doi.org/10.1299/kikaic.56.658>.
- [49] A. Gesualdo, A. Iannuzzo, M. Guadagnuolo, A. Guerriero, M. Monaco, M. Savino, and M. Guadagnuolo, "Numerical analysis of rigid body behaviour," *Applied Mechanics and Materials*, vol. 847, pp. 240–247, 2016. DOI: <https://doi.org/10.4028/www.scientific.net/AMM.847.240>.
- [50] A. Gesualdo, A. Iannuzzo, V. Minutolo, and M. Monaco, "Rocking of freestanding objects: Theoretical and experimental comparisons," *Journal of Theoretical and Applied Mechanics (Poland)*, vol. 56, pp. 977–991, 2018. DOI: <https://doi.org/10.15632/jtam-pl.56.4.977>.
- [51] A. Gesualdo, A. Iannuzzo, and M. Monaco, "Rocking behaviour of freestanding objects," *Journal of Physics: Conference Series*, vol. 1141, p. 012 091, 2018. DOI: <https://doi.org/10.1088/1742-6596/1141/1/012091>.
- [52] A. Gesualdo, A. Iannuzzo, M. Monaco, and F. Penta, "Rocking of a rigid block freestanding on a flat pedestal," *Journal of Zhejiang University-SCIENCE A*, vol. 19, no. 5, pp. 331–345, 2018. DOI: <https://doi.org/10.1631/jzus.A1700061>.
- [53] E. J. Graesser and F. A. Cozzarelli, "Shape-memory alloys as new materials for aseismic isolation," *Journal of Engineering Mechanics*, vol. 117, no. 11, pp. 2590–2608, 1991. DOI: [https://doi.org/10.1061/\(ASCE\)0733-9399\(1991\)117:11\(2590\)](https://doi.org/10.1061/(ASCE)0733-9399(1991)117:11(2590)).
- [54] F. Greco, R. Luciano, G. Serino, and N. Vaiana, "A mixed explicit-implicit time integration approach for nonlinear analysis of base-isolated structures," *Annals of Solid and Structural Mechanics*, vol. 10, no. 1, pp. 17–29, 2018. DOI: <https://doi.org/10.1007/s12356-017-0051-z>.
- [55] H. A. Hadad, A. Calabrese, S. Strano, and G. Serino, "A base isolation system for developing countries using discarded tyres filled with elastomeric recycled materials," *Journal of Earthquake Engineering*, vol. 21, no. 2, pp. 246–266, 2017. DOI: <https://doi.org/10.1080/13632469.2016.1172371>.
- [56] T. Heitz, C. Giry, B. Richard, and F. Ragueneau, "Identification of an equivalent viscous damping function depending on engineering demand parameters," *Engineering Structures*, vol. 188, pp. 637–649, 2019. DOI: <https://doi.org/10.1016/j.engstruct.2019.03.058>.

- [57] M. Hodgdon, "Mathematical theory and calculations of magnetic hysteresis curves," *IEEE Transactions on Magnetics*, vol. 24, no. 6, pp. 3120–3122, 1988. DOI: <https://doi.org/10.1109/20.92354>.
- [58] S. J. Hogan, "On the dynamics of rigid-block motion under harmonic forcing," *Proceedings of the Royal Society of London. A. Mathematical and Physical Sciences*, vol. 425, no. 1869, pp. 441–476, 1989. DOI: <https://doi.org/10.1098/rspa.1989.0114>.
- [59] M. M. Hossain, R. Browning, R. Minkwitz, and H.-J. Sue, "Effect of asymmetric constitutive behavior on scratch-induced deformation of polymers," *Tribology Letters*, vol. 47, no. 1, pp. 113–122, 2012. DOI: <https://doi.org/10.1007/s11249-012-9967-y>.
- [60] G. W. Housner, "The behavior of inverted pendulum structures during earthquakes," *Bulletin of the Seismological Society of America*, vol. 53, no. 2, pp. 403–417, 1963.
- [61] I. Iervolino, C. Galasso, and E. Cosenza, "Rexel: Computer aided record selection for code-based seismic structural analysis," *Bulletin of Earthquake Engineering*, vol. 8, no. 2, pp. 339–362, 2010. DOI: <https://doi.org/10.1007/s10518-009-9146-1>.
- [62] F. Ikhoulane, V. Mañosa, and J. Rodellar, "Dynamic properties of the hysteretic Bouc-Wen model," *Systems & Control Letters*, vol. 56, no. 3, pp. 197–205, 2007. DOI: <https://doi.org/10.1016/j.sysconle.2006.09.001>.
- [63] Y. Ishiyama, "Motions of rigid bodies and criteria for overturning by earthquake excitations," *Earthquake Engineering & Structural Dynamics*, vol. 10, no. 5, pp. 635–650, 1982. DOI: <https://doi.org/10.1002/eqe.4290100502>.
- [64] M. Ismail, F. Ikhoulane, and J. Rodellar, "The hysteresis Bouc-Wen model, a survey," *Archives of Computational Methods in Engineering*, vol. 16, no. 2, pp. 161–188, 2009. DOI: <https://doi.org/10.1007/s11831-009-9031-8>.
- [65] D. Jiles and D. Atherton, "Theory of ferromagnetic hysteresis," *Journal of Magnetism and Magnetic Materials*, vol. 61, no. 1, pp. 48–60, 1986. DOI: [https://doi.org/10.1016/0304-8853\(86\)90066-1](https://doi.org/10.1016/0304-8853(86)90066-1).
- [66] I. Kavvadias, H. Bibo, and L. Vasiliadis, "Numerical study on the dynamic response of classical column standing free on an isolated base," in *Proceedings of 6th ECCOMAS Thematic Conference on Computational Methods in Structural Dynamics and Earthquake Engineering*, Jun. 2017. DOI: <https://doi.org/10.7712/120117.5614.17410>.

- [67] I. Kavvadias, L. Vasiliadis, A. Elenas, and K. Koutsoupakis, "Fragility assessment of base isolated free standing museum artifacts," in *Proceedings of 6th Conference on Computational Methods in Structural Dynamics and Earthquake Engineering*, Jun. 2019. DOI: <https://doi.org/10.7712/120119.7120.19829>.
- [68] M. Kikuchi and I. D. Aiken, "An analytical hysteresis model for elastomeric seismic isolation bearings," *Earthquake Engineering & Structural Dynamics*, vol. 26, no. 2, pp. 215–231, 1997. DOI: [https://doi.org/10.1002/\(SICI\)1096-9845\(199702\)26:2<215::AID-EQE640>3.0.CO;2-9](https://doi.org/10.1002/(SICI)1096-9845(199702)26:2<215::AID-EQE640>3.0.CO;2-9).
- [69] K. Klaboe, S. Pujol, and L. Laughery, "Seismic response of rocking blocks," *Earthquake Spectra*, vol. 34, no. 3, pp. 1051–1063, 2018. DOI: <https://doi.org/10.1193/060517EQS107DP>.
- [70] D. Konstantinidis and N. Makris, "Experimental and analytical studies on the response of freestanding laboratory equipment to earthquake shaking," *Earthquake Engineering & Structural Dynamics*, vol. 38, no. 6, pp. 827–848, 2009. DOI: <https://doi.org/10.1002/eqe.871>.
- [71] D. Konstantinidis and N. Makris, "Experimental and analytical studies on the response of 1/4-scale models of freestanding laboratory equipment subjected to strong earthquake shaking," *Bulletin of Earthquake Engineering*, vol. 8, no. 6, pp. 1457–1477, 2010. DOI: <https://doi.org/10.1007/s10518-010-9192-8>.
- [72] A. N. Kounadis, "On the rocking–sliding instability of rigid blocks under ground excitation: Some new findings," *Soil Dynamics and Earthquake Engineering*, vol. 75, pp. 246–258, 2015. DOI: <https://doi.org/10.1016/j.soildyn.2015.03.026>.
- [73] S. S. Kumar, A. M. Krishna, and A. Dey, "Evaluation of dynamic properties of sandy soil at high cyclic strains," *Soil Dynamics and Earthquake Engineering*, vol. 99, pp. 157–167, 2017. DOI: <https://doi.org/10.1016/j.soildyn.2017.05.016>.
- [74] D. Liberatore, D. Addessi, and M. Sangirardi, "An enriched Bouc-Wen model with damage," *European Journal of Mechanics - A/Solids*, 2019.
- [75] S. A. Linde, D. Konstantinidis, and M. J. Tait, "Rocking response of unanchored building contents considering horizontal and vertical excitation," *Journal of Structural Engineering*, vol. 146, no. 9, p. 04020175, 2020. DOI: [https://doi.org/10.1061/\(ASCE\)ST.1943-541X.0002735](https://doi.org/10.1061/(ASCE)ST.1943-541X.0002735).
- [76] D. Losanno, H. Hadad, and G. Serino, "Design charts for eurocode-based design of elastomeric seismic isolation systems," *Soil Dynamics and Earthquake Engineering*, vol. 119, pp. 48–498, 2019. DOI: <https://doi.org/10.1016/j.soildyn.2017.12.017>.

- [77] D. Losanno, I. E. Madera Sierra, M. Spizzuoco, J. Marulanda, and P. Thomson, "Experimental assessment and analytical modeling of novel fiber-reinforced isolators in unbounded configuration," *Composite Structures*, vol. 212, pp. 66–82, 2019. DOI: <https://doi.org/10.1016/j.compstruct.2019.01.026>.
- [78] D. Losanno, I. E. Madera Sierra, M. Spizzuoco, J. Marulanda, and P. Thomson, "Experimental performance of unbonded polyester and carbon fiber reinforced elastomeric isolators under bidirectional seismic excitation," *Engineering Structures*, vol. 209, p. 110 003, 2020. DOI: <https://doi.org/10.1016/j.engstruct.2019.110003>.
- [79] D. Losanno, M. Spizzuoco, and A. Calabrese, "Bidirectional shaking-table tests of unbonded recycled-rubber fiber-reinforced bearings (rr-frbs)," *Structural Control and Health Monitoring*, vol. 26, no. 9, e2386, 2019. DOI: <https://doi.org/10.1002/stc.2386>.
- [80] M. Lowry, D. Armendariz, B. Farrar, and J. Podany, "Seismic mount making: A review of the protection of objects in the J. Paul Getty Museum from earthquake damage," in *Advances in the Protection of Museum Collections from Earthquake Damage*, J. Paul Getty Museum at the Getty Villa, Los Angeles, 2008.
- [81] L. Luzi, G. Lanzano, C. Felicetta, M. C. D'Amico, E. Russo, S. Sgobba, F. Pacor, and. ORFEUS Working Group 5. "Engineering strong motion database (ESM) (version 2.0). istituto nazionale di geofisica e vulcanologia (INGV)." (2020).
- [82] N. Makris and M. Aghagholizadeh, "Effect of supplemental hysteretic and viscous damping on rocking response of free-standing columns," *Journal of Engineering Mechanics*, vol. 145, no. 5, p. 04 019 028, 2019. DOI: [https://doi.org/10.1061/\(ASCE\)EM.1943-7889.0001596](https://doi.org/10.1061/(ASCE)EM.1943-7889.0001596).
- [83] N. Makris and Y. S. Roussos, "Rocking response of rigid blocks under near-source ground motions," *Géotechnique*, vol. 50, no. 3, pp. 243–262, 2000. DOI: <https://doi.org/10.1680/geot.2000.50.3.243>.
- [84] N. Makris and M. F. Vassiliou, "Planar rocking response and stability analysis of an array of free-standing columns capped with a freely supported rigid beam," *Earthquake Engineering & Structural Dynamics*, vol. 42, no. 3, pp. 431–449, 2013. DOI: <https://doi.org/10.1002/eqe.2222>.
- [85] P. K. Malhotra, *Seismic Analysis of Structures and Equipment*. Springer International Publishing AG., 2009.

- [86] F. Marmo and L. Rosati, "Analytical integration of elasto-plastic uniaxial constitutive laws over arbitrary sections," *International Journal for Numerical Methods in Engineering*, vol. 91, no. 9, pp. 990–1022, 2012. DOI: <https://doi.org/10.1002/nme.4316>.
- [87] I. Mayergoyz, *Mathematical Models of Hysteresis*. Springer, New York, NY, 1991. DOI: <https://doi.org/10.1007/978-1-4612-3028-1>.
- [88] M. Menegotto and P. E. Pinto, "Method of analysis for cyclic loaded R. C. plane frame including changes in geometry and non-elastic behaviour of elements under combined normal force and bending," in *Proceedings of IABSE Symposium on Resistance and Ultimate Deform ability of Structures Acted On by Well Defined Repeated Loads*, 1973, pp. 15–22. DOI: <http://doi.org/10.5169/seals-13741>.
- [89] M. Monaco, M. Guadagnuolo, and A. Gesualdo, "The role of friction in the seismic risk mitigation of freestanding art objects," *Natural Hazards*, vol. 73, no. 2, pp. 389–402, 2014. DOI: <https://doi.org/10.1007/s11069-014-1076-9>.
- [90] F. Naeim and J. M. Kelly, *Design of Seismic Isolated Structures: From Theory to Practice*. Wiley, 1999, ISBN: 978-0-471-14921-7.
- [91] I. Nuzzo, D. Losanno, and N. Caterino, "Seismic design and retrofit of frame structures with hysteretic dampers: A simplified displacement-based procedure," *Bulletin of Earthquake Engineering*, vol. 17, no. 5, pp. 2787–2819, 2019. DOI: <https://doi.org/10.1007/s10518-019-00558-8>.
- [92] F. Parisi and N. Augenti, "Earthquake damages to cultural heritage constructions and simplified assessment of artworks," *Engineering Failure Analysis*, vol. 34, pp. 735–760, 2013. DOI: <https://doi.org/10.1016/j.engfailanal.2013.01.005>.
- [93] R. Park and T. Paulay, "Strength of members with flexure and axial load," in *Reinforced Concrete Structures*. John Wiley & Sons, Ltd, 1975, ch. 5, pp. 118–194. DOI: <https://doi.org/10.1002/9780470172834.ch5>.
- [94] D. Pellecchia and P. Cesarano, "A generalized formulation of time integration methods for nonlinear dynamic analysis of hysteretic mechanical systems," in *Mathematical Applications in Continuum and Structural Mechanics*. Springer International Publishing, 2021, pp. 149–172. DOI: https://doi.org/10.1007/978-3-030-42707-8_8.

- [95] D. Pellecchia, S. Lo Feudo, N. Vaiana, J.-L. Dion, and L. Rosati, "A procedure to model and design elastomeric-based isolation systems for the seismic protection of rocking art objects," *Computer-Aided Civil and Infrastructure Engineering*, vol. n/a, no. n/a, pp. 1–18, 2021. DOI: <https://doi.org/10.1111/mice.12775>.
- [96] D. Pellecchia, S. Lo Feudo, N. Vaiana, J.-L. Dion, and L. Rosati, "Seismic protection of cultural heritage artefacts by means of elastomeric isolators: A case study," in *Proceedings of 8th International Conference on Computational Methods in Structural Dynamics and Earthquake Engineering (8COMPdyn)*, Streamed from Athens, Greece, Jun. 2021, pp. 2446–2455. DOI: <https://doi.org/10.7712/120121.8649.18631>.
- [97] D. Pellecchia and M. Paradiso, "A review of the class of bouc-wen differential models for simulating mechanical hysteresis phenomena," in *Mathematical Applications in Continuum and Structural Mechanics*. Springer International Publishing, 2021, pp. 127–148. DOI: https://doi.org/10.1007/978-3-030-42707-8_7.
- [98] D. Pellecchia, S. Sessa, N. Vaiana, and L. Rosati, "Comparative assessment on the rocking response of seismically base-isolated rigid blocks," *Procedia Structural Integrity*, vol. 29, pp. 95–102, 2020, Art Collections 2020, Safety Issue (ARCO 2020, SAFETY). DOI: <https://doi.org/10.1016/j.prostr.2020.11.144>.
- [99] C. Petrone, L. Di Sarno, G. Magliulo, and E. Cosenza, "Numerical modelling and fragility assessment of typical freestanding building contents," *Bulletin of Earthquake Engineering*, vol. 15, no. 4, pp. 1609–1633, 2017. DOI: <https://doi.org/10.1007/s10518-016-0034-1>.
- [100] F. Peña, F. Prieto, P. B. Lourenço, A. Campos Costa, and J. V. Lemos, "On the dynamics of rocking motion of single rigid-block structures," *Earthquake Engineering & Structural Dynamics*, vol. 36, no. 15, pp. 2383–2399, 2007. DOI: <https://doi.org/10.1002/eqe.739>.
- [101] J. Podany, "Safeguarding a collection and building from natural hazards, in perspectives on natural disaster mitigation," in *Papers presented at American Institute for Conservation of Historic & Artistic Works Workshop*, Washington DC, 1991, pp. 51–67.
- [102] J. Podany, *Advances in the Protection of Museum Collections from Earthquake Damage: Papers from a Symposium Held at the J. Paul Getty Museum at the Villa on May 3- 4, 2006*. Getty Publications, 2008, ISBN: 9780892369089.

- [103] J. Podany, *When Galleries Shake: Earthquake Damage Mitigation for Museum Collections*. Getty Publications, 2017, ISBN: 978-1-60606-522-8.
- [104] I. N. Psycharis and P. C. Jennings, "Rocking of slender rigid bodies allowed to uplift," *Earthquake Engineering & Structural Dynamics*, vol. 11, no. 1, pp. 57–76, 1983. DOI: <https://doi.org/10.1002/eqe.4290110106>.
- [105] M. D. Purvance, A. Anooshehpour, and J. N. Brune, "Free-standing block overturning fragilities: Numerical simulation and experimental validation," *Earthquake Engineering & Structural Dynamics*, vol. 37, no. 5, pp. 791–808, 2008. DOI: <https://doi.org/10.1002/eqe.789>.
- [106] W. Ramberg and W. Osgood, "Description of stress-strain curves by three parameters," NTRS - NASA Technical Reports Server, Tech. Rep., 1943.
- [107] P. Roussis and S. Odysseos, "Slide-rocking response of seismically-isolated rigid structures subjected to horizontal ground excitation," in *Proceedings of 2nd European Conference on Earthquake Engineering and Seismology*, 2014.
- [108] P. Roussis and S. Odysseos, "Rocking response of seismically-isolated rigid blocks under simple acceleration pulses and earthquake excitations," *The Open Construction and Building Technology Journal*, vol. 11, pp. 217–236, 2017. DOI: <https://doi.org/10.2174/1874836801711010217>.
- [109] P. Roussis, E. Pavlou, and E. Pisiara, "Base-isolation technology for earthquake protection of art objects," in *Proceedings of 14th World Conference on Earthquake Engineering*, 2008.
- [110] A. Salvatore, B. Carboni, L.-Q. Chen, and W. Lacarbonara, "Non-linear dynamic response of a wire rope isolator: Experiment, identification and validation," *Engineering Structures*, vol. 238, p. 112 121, 2021. DOI: <https://doi.org/10.1016/j.engstruct.2021.112121>.
- [111] S. Sessa. "Paride - parameter identification freeware." (2021), [Online]. Available: <https://bit.ly/35F5x7Q>.
- [112] S. Sessa, "Thermodynamic compatibility conditions of a new class of hysteretic materials," *Continuum Mechanics and Thermodynamics*, 2021. DOI: <https://doi.org/10.1007/s00161-021-01044-w>.
- [113] S. Sessa, N. Vaiana, M. Paradiso, and L. Rosati, "An inverse identification strategy for the mechanical parameters of a phenomenological hysteretic constitutive model," *Mechanical Systems and Signal Processing*, vol. 139, p. 106 622, 2020. DOI: <https://doi.org/10.1016/j.ymsp.2020.106622>.

- [114] H. W. Shenton, "Criteria for initiation of slide, rock, and slide-rock rigid-body modes," *Journal of Engineering Mechanics*, vol. 122, no. 7, pp. 690–693, 1996. DOI: [https://doi.org/10.1061/\(ASCE\)0733-9399\(1996\)122:7\(690\)](https://doi.org/10.1061/(ASCE)0733-9399(1996)122:7(690)).
- [115] H. W. Shenton and N. P. Jones, "Base excitation of rigid bodies. i: Formulation," *Journal of Engineering Mechanics*, vol. 117, no. 10, pp. 2286–2306, 1991. DOI: [https://doi.org/10.1061/\(ASCE\)0733-9399\(1991\)117:10\(2286\)](https://doi.org/10.1061/(ASCE)0733-9399(1991)117:10(2286)).
- [116] H. W. Shenton and N. P. Jones, "Base excitation of rigid bodies. ii: Periodic slide-rock response," *Journal of Engineering Mechanics*, vol. 117, no. 10, pp. 2307–2328, 1991. DOI: [https://doi.org/10.1061/\(ASCE\)0733-9399\(1991\)117:10\(2307\)](https://doi.org/10.1061/(ASCE)0733-9399(1991)117:10(2307)).
- [117] G. Simoneschi, C. Olivieri, A. M. de Leo, and A. Di Egidio, "Pole placement method to control the rocking motion of rigid blocks," *Engineering Structures*, vol. 167, pp. 39–47, 2018. DOI: <https://doi.org/10.1016/j.engstruct.2018.04.016>.
- [118] A. Sinopoli, "Unilaterality and dry friction: A geometric formulation for two-dimensional rigid body dynamics," *Nonlinear Dynamics*, vol. 12, no. 4, pp. 343–366, 1997. DOI: <https://doi.org/10.1023/A:1008289716620>.
- [119] T. Sireteanu, M. Giuclea, A.-M. Mitu, and G. Ghita, "A Genetic Algorithms Method for Fitting the Generalized Bouc-Wen Model to Experimental Asymmetric Hysteretic Loops," *Journal of Vibration and Acoustics*, vol. 134, no. 4, 2012. DOI: <https://doi.org/10.1115/1.4005845>.
- [120] M. V. Sivaselvan and A. M. Reinhorn, "Hysteretic models for deteriorating inelastic structures," *Journal of Engineering Mechanics*, vol. 126, no. 6, pp. 633–640, 2000. DOI: [https://doi.org/10.1061/\(ASCE\)0733-9399\(2000\)126:6\(633\)](https://doi.org/10.1061/(ASCE)0733-9399(2000)126:6(633)).
- [121] R. I. Skinner, W. H. Robinson, and G. McVerry, *An introduction to seismic isolation*, Wiley, Ed. 1993, ISBN: 978-0471934332.
- [122] J. Song and A. Der Kiureghian, "Generalized Bouc-Wen model for highly asymmetric hysteresis," *Journal of Engineering Mechanics*, vol. 132, no. 6, pp. 610–618, 2006. DOI: [https://doi.org/10.1061/\(ASCE\)0733-9399\(2006\)132:6\(610\)](https://doi.org/10.1061/(ASCE)0733-9399(2006)132:6(610)).
- [123] P. D. Spanos and A. Koh, "Rocking of rigid blocks due to harmonic shaking," *Journal of Engineering Mechanics*, vol. 110, no. 11, pp. 1627–1642, 1984. DOI: [https://doi.org/10.1061/\(ASCE\)0733-9399\(1984\)110:11\(1627\)](https://doi.org/10.1061/(ASCE)0733-9399(1984)110:11(1627)).

- [124] M. Spizzuoco, V. Quaglini, A. Calabrese, G. Serino, and C. Zambrano, "Study of wire rope devices for improving the re-centering capability of base isolated buildings," *Structural Control and Health Monitoring*, vol. 24, no. 6, e1928, 2017. DOI: <https://doi.org/10.1002/stc.1928>.
- [125] C. Spyrakos, C. Maniatakis, and I. Taflampas, "Assessment of seismic risk for museum artifacts," in *Proceedings of 14th World Conference on Earthquake Engineering (14WCEE)*, Beijing, China, Oct. 2008.
- [126] T. Taniguchi, "Non-linear response analyses of rectangular rigid bodies subjected to horizontal and vertical ground motion," *Earthquake Engineering & Structural Dynamics*, vol. 31, no. 8, pp. 1481–1500, 2002. DOI: <https://doi.org/10.1002/eqe.170>.
- [127] T. Ther and L. P. Kollár, "Overturning of rigid blocks for earthquake excitation," *Bulletin of Earthquake Engineering*, vol. 16, no. 3, pp. 1607–1631, 2018. DOI: <https://doi.org/10.1007/s10518-017-0238-z>.
- [128] R. Thiers-Moggia and C. Málaga-Chuquitaype, "Seismic protection of rocking structures with inerters," *Earthquake Engineering & Structural Dynamics*, vol. 48, no. 5, pp. 528–547, 2019. DOI: <https://doi.org/10.1002/eqe.3147>.
- [129] M. Tinker and M. Cutchins, "Damping phenomena in a wire rope vibration isolation system," *Journal of Sound and Vibration*, vol. 157, no. 1, pp. 7–18, 1992. DOI: [https://doi.org/10.1016/0022-460X\(92\)90564-E](https://doi.org/10.1016/0022-460X(92)90564-E).
- [130] R. G. Tyler and W. H. Robinson, "High-strain tests on lead-rubber bearings for earthquake loadings," *Bulletin of the New Zealand Society for Earthquake Engineering*, vol. 17, no. 2, pp. 90–105, 1984. DOI: <https://doi.org/10.5459/bnzsee.17.2.90-105>.
- [131] N. Vaiana, R. Capuano, S. Sessa, F. Marmo, and L. Rosati, "Non-linear dynamic analysis of seismically base-isolated structures by a novel openesses hysteretic material model," *Applied Sciences*, vol. 11, no. 3, 2021. DOI: <https://doi.org/10.3390/app11030900>.
- [132] N. Vaiana, F. Marmo, S. Sessa, and L. Rosati, "Modeling of the hysteretic behavior of wire rope isolators using a novel rate-independent model," in *Nonlinear Dynamics of Structures, Systems and Devices*, Springer International Publishing, 2020, pp. 309–317.

- [133] N. Vaiana, S. Sessa, F. Marmo, and L. Rosati, "A class of uniaxial phenomenological models for simulating hysteretic phenomena in rate-independent mechanical systems and materials," *Nonlinear Dynamics*, vol. 93, no. 3, pp. 1647–1669, 2018. DOI: <https://doi.org/10.1007/s11071-018-4282-2>.
- [134] N. Vaiana, S. Sessa, F. Marmo, and L. Rosati, "An accurate and computationally efficient uniaxial phenomenological model for steel and fiber reinforced elastomeric bearings," *Composite Structures*, vol. 211, pp. 196–212, 2019. DOI: <https://doi.org/10.1016/j.compstruct.2018.12.017>.
- [135] N. Vaiana, S. Sessa, F. Marmo, and L. Rosati, "Nonlinear dynamic analysis of hysteretic mechanical systems by combining a novel rate-independent model and an explicit time integration method," *Nonlinear Dynamics*, vol. 98, no. 4, pp. 2879–2901, 2019. DOI: <https://doi.org/10.1007/s11071-019-05022-5>.
- [136] N. Vaiana, M. Spizzuoco, and G. Serino, "Wire rope isolators for seismically base-isolated lightweight structures: Experimental characterization and mathematical modeling," *Engineering Structures*, vol. 140, pp. 498–514, 2017. DOI: <https://doi.org/10.1016/j.engstruct.2017.02.057>.
- [137] N. Valoroso and R. Fedele, "Characterization of a cohesive-zone model describing damage and de-cohesion at bonded interfaces. sensitivity analysis and mode-i parameter identification," *International Journal of Solids and Structures*, vol. 47, no. 13, pp. 1666–1677, 2010. DOI: <https://doi.org/10.1016/j.ijsolstr.2010.03.001>.
- [138] M. F. Vassiliou and N. Makris, "Analysis of the rocking response of rigid blocks standing free on a seismically isolated base," *Earthquake Engineering & Structural Dynamics*, vol. 41, no. 2, pp. 177–196, 2012. DOI: <https://doi.org/10.1002/eqe.1124>.
- [139] I. Venanzi, L. Ierimonti, and A. L. Materazzi, "Active base isolation of museum artifacts under seismic excitation," *Journal of Earthquake Engineering*, vol. 24, no. 3, pp. 506–527, 2018. DOI: <https://doi.org/10.1080/13632469.2018.1453410>.
- [140] F. Vestroni and S. Di Cinto, "Base isolation for seismic protection of statues," in *Proceedings of 12th World Conference of Earthquake Engineering*, 2000.
- [141] A. Visintin, *Differential Models of Hysteresis*, ser. Applied Mathematical Sciences. Springer, Berlin, Heidelberg, 1994. DOI: <https://doi.org/10.1007/978-3-662-11557-2>.

- [142] E. Voyagaki, I. N. Psycharis, and G. Mylonakis, "Rocking response and overturning criteria for free standing rigid blocks to single-lobe pulses," *Soil Dynamics and Earthquake Engineering*, vol. 46, pp. 85–95, 2013. DOI: <https://doi.org/10.1016/j.soildyn.2012.11.010>.
- [143] R. A. Waltz, J. L. Morales, J. Nocedal, and D. Orban, "An interior algorithm for nonlinear optimization that combines line search and trust region steps," *Mathematical Programming*, vol. 107, no. 3, pp. 391–408, 2006. DOI: <https://doi.org/10.1007/s10107-004-0560-5>.
- [144] C. Wang and Y. Wen, "Reliability and redundancy of pre-northridge low-rise steel buildings under seismic excitation," University Illinois at Urbana-Champaign, Tech. Rep., 1998.
- [145] Y.-K. Wen, "Method for random vibration of hysteretic systems," *Journal of the Engineering Mechanics Division*, vol. 102, no. 2, pp. 249–263, 1976. DOI: <https://doi.org/10.1061/JMCEA3.0002106>.
- [146] Y. K. Wen, "Equivalent Linearization for Hysteretic Systems Under Random Excitation," *Journal of Applied Mechanics*, vol. 47, no. 1, pp. 150–154, 1980. DOI: <https://doi.org/10.1115/1.3153594>.
- [147] C. E. Wittich, T. C. Hutchinson, R. L. Wood, M. Seracini, and F. Kuester, "Characterization of full-scale, human-form, culturally important statues: Case study," *Journal of Computing in Civil Engineering*, vol. 30, no. 3, p. 05015001, 2016. DOI: [https://doi.org/10.1061/\(ASCE\)CP.1943-5487.0000508](https://doi.org/10.1061/(ASCE)CP.1943-5487.0000508).
- [148] C.-S. Yim, A. K. Chopra, and J. Penzien, "Rocking response of rigid blocks to earthquakes," *Earthquake Engineering & Structural Dynamics*, vol. 8, no. 6, pp. 565–587, 1980. DOI: <https://doi.org/10.1002/eqe.4290080606>.
- [149] J. Zhang and N. Makris, "Rocking response of free-standing blocks under cycloidal pulses," *Journal of Engineering Mechanics*, vol. 127, no. 5, pp. 473–483, 2001. DOI: [https://doi.org/10.1061/\(ASCE\)0733-9399\(2001\)127:5\(473\)](https://doi.org/10.1061/(ASCE)0733-9399(2001)127:5(473)).
- [150] G. Zuccaro, F. Dato, F. Cacace, D. de Gregorio, and S. Sessa, "Seismic collapse mechanisms analyses and masonry structures typologies: A possible correlation," *Ingegneria Sismica*, vol. 34, no. 4, pp. 121–149, 2017.
- [151] H. Özdemir, "Nonlinear transient dynamic analysis of yielding structures," Ph.D. Thesis, University of California, Berkeley, 1976.

AUTHOR'S PUBLICATIONS

1. D. Pellecchia *et al.*, "Comparative assessment on the rocking response of seismically base-isolated rigid blocks," *Procedia Structural Integrity*, vol. 29, pp. 95–102, 2020, Art Collections 2020, Safety Issue (ARCO 2020, SAFETY). DOI: <https://doi.org/10.1016/j.prostr.2020.11.144>
2. D. Pellecchia *et al.*, "A procedure to model and design elastomeric-based isolation systems for the seismic protection of rocking art objects," *Computer-Aided Civil and Infrastructure Engineering*, vol. n/a, no. n/a, pp. 1–18, 2021. DOI: <https://doi.org/10.1111/mice.12775>
3. D. Pellecchia *et al.*, "Seismic protection of cultural heritage artefacts by means of elastomeric isolators: A case study," in *Proceedings of 8th International Conference on Computational Methods in Structural Dynamics and Earthquake Engineering (8COMPdyn)*, Streamed from Athens, Greece, Jun. 2021, pp. 2446–2455. DOI: <https://doi.org/10.7712/120121.8649.18631>
4. D. Pellecchia and M. Paradiso, "A review of the class of bouc-wen differential models for simulating mechanical hysteresis phenomena," in *Mathematical Applications in Continuum and Structural Mechanics*. Springer International Publishing, 2021, pp. 127–148. DOI: https://doi.org/10.1007/978-3-030-42707-8_7
5. D. Pellecchia and P. Cesarano, "A generalized formulation of time integration methods for nonlinear dynamic analysis of hysteretic mechanical systems," in *Mathematical Applications in Continuum and Structural Mechanics*. Springer International Publishing, 2021, pp. 149–172. DOI: https://doi.org/10.1007/978-3-030-42707-8_8

COLOPHON

This document was typeset using the typographical look-and-feel `classicthesis` developed by André Miede and Ivo Pletikosić. The style was inspired by Robert Bringhurst's seminal book on typography "*The Elements of Typographic Style*". `classicthesis` is available for both \LaTeX and LyX :

<https://bitbucket.org/amiede/classicthesis/>

Happy users of `classicthesis` usually send a real postcard to the author, a collection of postcards received so far is featured here:

<http://postcards.miede.de/>

Thank you very much for your feedback and contribution.